Thermoelectric Properties of Coinage Metal Chalcogenides

by

Cheryl Sturm

A thesis

presented to the University of Waterloo

in fulfilment of the

thesis requirement for the degree of

Doctor of Philosophy

in

Chemistry

Waterloo, Ontario, Canada, 2021

Examining Committee Membership

The following served on the Examining Committee for this thesis. The decision of the Examining Committee is by majority vote.

External Examiner	Kirill Kovnir Associate Professor (Iowa State University)
Supervisor(s)	Holger Kleinke Professor (University of Waterloo)
Internal Members	Sonny Lee Professor (University of Waterloo)
	Eric Prouzet Associate Professor (University of Waterloo)
Internal-external Member	William Wong Professor (University of Waterloo)
Other Member(s)	Kathryn Preuss Professor (University of Guelph)

Author's Declaration

I hereby declare that I am the sole author of this thesis. This is a true copy of the thesis including any required final revisions, as accepted by my examiners. I understand that my thesis may be made electronically available to the public.

Abstract

Research into the development of high performance thermoelectric materials has been gaining interest because of the potential for various applications. In the public eye, thermoelectric devices are readily recognized, such as the radioisotope thermoelectric generators utilized by space agencies to power exploratory rovers on Mars and deep space satellites. Thermoelectric materials are also investigated for their 'green applications', such as waste heat recovery in automobiles and industrial processes. The purpose of this thesis is to optimize and study the thermoelectric properties, and determine the viability as potential candidates for thermoelectric devices of three different coinage metal chalcogenides: $Cu_5Sn_2Se_7$ and $Cu_5Sn_2Te_7$, $Ba_3Cu_{14-\delta}Te_{12}$, and Ag_8SnS_6.

The first compounds discussed (Chapter 3) are $Cu_5Sn_2Se_7$ and $Cu_5Sn_2Te_7$, which were previously reported to have metal-like properties, which are not desirable characteristics for thermoelectric materials. The aim of this study was to reduce the carrier concentration of these materials by Zn-doping to enhance the thermopower, and then investigate the thermoelectric properties of the doped materials in comparison to the undoped ones. The compounds were synthesized using both the traditional solid-state tube method and ball-milling. The crystal structures were characterized using powder X-ray diffraction, which confirmed that all materials crystallize in the monoclinic system with the space group *C*2. With the partial substitution of zinc for copper atoms, the compounds exhibited an overall improvement in their thermoelectric properties. Figure of merit values were determined to be 0.20 for $Cu_4ZnSn_2Se_7$ at 615 K and 0.05 for $Cu_4ZnSn_2Te_7$ at 575 K.

The fourth chapter aims to investigate the thermoelectric properties of hot-pressed $Ba_3Cu_{14-\delta}Te_{12}$, with a focus on stability concerns due to potential Cu ion movement. Previously published data had suggested that the title compound may be a potential candidate as a mid-temperature

range thermoelectric material. All $Ba_3Cu_{14-\delta}Te_{12}$ materials displayed low thermal conductivity values (<1 W $m^{-1}K^{-1}$) and desirable electrical conductivities (300 $\Omega^{-1}cm^{-1}$ – 600 $\Omega^{-1}cm^{-1}$). However, the thermopowers presented were low (< +65 μV K^{-1}), which produced small zT values, with the highest being achieved zT = 0.12 at 570 K for $Ba_3Cu_{13.175}Te_{12}$. Good reproducibility was ascertained when limiting the property measurements to remain below 600 K.

In an attempt to increase the thermopower, and therefore the figure of merit, a brief alloying study with Ag was investigated ($Ba_3Cu_{14-\delta-x}Ag_xTe_{12}$). The addition of Ag, however, did not produce any significant improvements. With the recent studies of Cu^+ mobility in other barium copper chalcogenides such as $Ba_3Cu_{16-x}(S,Te)_{11}$, single crystal studies were performed at room temperature to investigate potential changes in the Cu sites after the property measurements. Two single crystals were picked from samples that were tested up to 573 and 673 K; no significant changes in the occupancies in any of the Cu sites were observed.

The fifth chapter investigates the stability, and the thermoelectric properties of Ag_8SnS_6 and $Ag_{8.1}SnS_6$. A bulk sample of Ag_8SnS_6 was previously reported to exhibit a peak zT of 0.5 at 750 K. It is apparent however, that mixed ion-electron conductors such as Ag_8SnS_6, due to mobile Ag^+, could have stability issues, which were not addressed in previous studies. Indeed, our initial measurements revealed precipitation of Ag and Ag_2S wires, depending on the measurement conditions. By limiting the highest operating temperature and the amount of current placed through the sample, stability was achieved. Competitive thermopower values were obtained (S: -500 μV K^{-1} to -375 μV K^{-1} between 423 K and 723 K), as well as ultra-low thermal conductivity values (κ: 0.39 W $m^{-1}K^{-1}$ to 0.29 W $m^{-1}K^{-1}$ between 423 K and 723 K). However, very low electrical conductivity values (< 0.020 $\Omega^{-1}cm^{-1}$) caused dismal figure of merit values. Additional silver atoms were introduced (nominal composition $Ag_{8.1}SnS_6$) in an effort to increase the amount of

charge carriers and thus the electrical conductivity. The electrical conductivity overall increased significantly (σ: 6.9 $\Omega^{-1}cm^{-1}$ at 770 K), but not sufficiently to produce a competitive figure of merit.

Acknowledgements

First and foremost, I would like to thank my supervisor, Dr. Holger Kleinke for this incredible opportunity to work in his lab. During your visit to Long Beach, CA, you helped me (or rather mostly me watching) try to solve the supercell structure of a material I was working on. Periodically you would ask *'Can we do this?'*, I do my usual awkward smile, and then you'd say *'Of course we can!'*. It's this 'can-do' attitude that really makes this space so unique. It permeates through the lab, and has allowed myself and my fellow lab mates to be as independent as we are. No problem goes unsolved and no task is too far out of reach. I have experienced a lot of growth as a scientist and as a person, and for that I am forever grateful.

I would also like to thank my committee members Dr. Sonny Lee, Dr. Kathryn Preuss, and Dr. Eric Prouzet. My success in this program wouldn't be possible without all of the advice and guidance I have been given throughout my time here. The suggestion of constant communication with your supervisor is one that I preach to anyone who will listen.

A special thank you to Dr. Jalil Assoud and Dr. Howard Siu for always checking in! We don't get many visitors to the basement of C2, so the afternoon chats and advice were always a treat.

I would also like to thank the past and present members of the Kleinke group for all of their support, in and out of the lab: Dr. Leilane Macario, Dr. Parisa Jafarzadeh, Dr. Yixuan Shi, Daniel Ramirez, Luke Menezes, Xiaoyu Cheng, Matthew VanZant, and Andrew Golabek. It has been so wonderful to work with everyone.

And of course I would like to thank my family for their unwavering support throughout my entire academic career. I have always felt a bit aloof, never knowing where I'll end up, but you all have always been there to remind me of my goals.

Table of Contents

List of Figures

List of Tables

List of Symbols and Abbreviations

Symbols

η (η_{max})	efficiency of a thermoelectric module (maximum)
P	power
Q	heat expelled or absorbed
T	absolute temperature
ZT (zT)	figure of merit of a device (material)
σ	electrical conductivity
S	Seebeck coefficient (or thermopower)
κ	thermal conductivity
n	carrier concentration
e	charge of current carrier
μ	carrier mobility
τ	time between collisions
m^*	effective mass of an electron
l	mean free math
v	velocity of electrons
V	voltage
G	Gibbs free energy of charge carriers
$\boldsymbol{S}$	entropy
$\boldsymbol{\mu}$	chemical potential
N	total number of charge carriers
$\boldsymbol{\theta}$	entropy per charge carrier
Φ	electrical potential
q	amount of charger per carrier
k_B	Boltzmann constant
h	Planck constant
C_p	specific heat capacity
R	universal gas constant
M	average molar mass
L_0	Lorenz number
M_f/M_a	mass of object in liquid/air
ρ_f/ρ_p	density of liquid/pellet
R/R_w	weighted/unweighted factors
F_o/F_c	observed/calculated structure factors
w	weighted factor
y_i/I_K	intensity value/Bragg intensity
i	increment of scattering angle

2θ	scattering angle
K	Miller indices (h,k,l)
L_K	Lorentz, polarization, and multiplicity factors
A	absorption factor

Abbreviations

PF	power factor
PGEC	phonon-glass electron-crystal
TE	thermoelectric
PLEC	phonon-liquid electron-crystal
MIEC	mixed ion-electron conductor
GSAS	General Structure Analysis System
SEM	scanning electron microscopy
EDAX	energy-dispersive analysis of X-ray spectroscopy
PXRD	powder X-ray diffraction
DFT	density functional theory
LDA	local-density approximation
PBE	Perdew-Burke-Ernzerhof
GGA	generalized gradient approximation
mBJ	modified Becke-Johnson
TG	thermogravimetry
DSC	differential scanning calorimetry

CHAPTER 1: Introduction

1.1 Application of Thermoelectric Materials

To put it briefly, thermoelectric materials have the ability to directly convert heat into electricity and vice versa. Since the discovery of this phenomena, thermoelectric devices have been implemented in a variety of applications in both scientific and commercial settings. Thermoelectric devices provide certain advantages, such as an absence of moving parts, no greenhouse gas emissions, and the utilization of cheap and environmentally friendly materials.[1,2]

The most basic use of the thermoelectric phenomena can be found in thermocouples. Thermocouples can either act as temperature sensors (e.g. in furnaces, refrigerators, air conditioning units) or can create a cold junction in many electronic systems. During the mid-twentieth century, radioisotope thermoelectric generators were developed for deep-space satellite use, since solar panel usage was not feasible being so far away from the sun.[3] In those cases, electricity was generated through the conversion of the heat released from radioactive isotope decay, which provided power to the satellite as well as any other equipment. More recent applications include devices powered by body heat,[4–6] refrigeration,[7–9] temperature-controlled cup holders in automobiles,[10] and sensors.[11,12] The future of thermoelectric materials may lie with the Internet of Things, a reference to not only electronics that are connected to the internet, but also for future objects that can have microprocessors embedded within said objects.[13] Utilizing thermoelectric materials with microprocessors allows for devices with longer life spans (e.g. no battery replacement) and could pave the way for wireless sensor networks for office buildings and homes.[14,15]

1.2 Thermoelectric Efficiency and Figure of Merit

Thermoelectric devices are typically composed of several thermoelectric modules, which contain both *n*- and *p*-type semiconductor legs. These legs are connected electrically in series and thermally in parallel. From a broad perspective, the efficiency (η) of a thermoelectric module is the ratio of the power supplied (P) to the flow of heat or heat absorbed (Q) from the hot side of module. This is expressed as

$$\eta = \frac{P}{Q} \tag{1-1}$$

With this information, the maximum efficiency of a thermoelectric device is determined by (η_{max}),

$$\eta_{max} = \frac{T_H - T_C}{T_H} \frac{\sqrt{1+ZT}-1}{\sqrt{1+ZT}+\frac{T_C}{T_H}} \tag{1-2}$$

where (T) is the absolute temperature, and (T_H) and (T_C) are the temperatures at the hot and cold ends respectively, and (ZT) is the figure of merit of a device. Since thermoelectrics are a heat engine, the first term of (Eq. 1-2) demonstrates that these modules' efficiencies are limited by the Carnot efficiency, and as such can never reach an efficiency of unity. The second term describes the figure of merit, which is governed by the materials' properties. More precisely, ZT (or zT for a material) is a dimensionless value that is used to determine the performance of thermoelectrics, which is given by:

$$ZT = \frac{\sigma S^2}{\kappa} T \tag{1-3}$$

where (σ) is the electrical conductivity, (S) is the Seebeck coefficient (or thermopower), and (κ) is the total thermal conductivity. A ZT value of one is desirable, but with recent advances in nanostructuring this has since then been exceeded.[16] The product of σ and S^2 is also known as the

power factor (PF), which is a measure of the electronic transport properties. A graphical depiction of a thermoelectric module is displayed in Fig. 1.1.

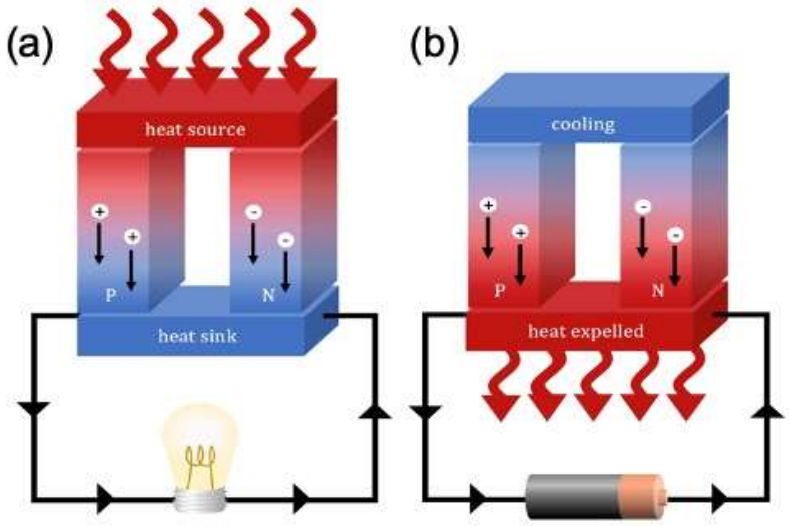

Figure 1.1. Depiction of thermoelectric modules in (a) power generation and (b) refrigeration. (Reproduced with permission from Lisa Grant)

In order to achieve a high figure of merit, certain criteria must be met. A high electrical conductivity and Seebeck coefficient must be maintained in conjunction with a low thermal conductivity. This poses problems, as tuning one parameter usually leads to a change in the others. This is because the σ, S, and κ are all coupled by the carrier concentration (n). For example, by increasing the carrier concentration, the electrical conductivity could also increase which is favorable. The thermal conductivity will also increase as κ is composed of two terms, κ_{el} (electrical component) and κ_{latt} (lattice component). The electrical component of the thermal conductivity will increase since the electrical conductivity has increased. This will be discussed further in detail in *Section 1.2.3*.

In general, degenerate semiconductors with large carrier concentrations ($n \sim 10^{19}$ - 10^{21} cm^{-3}) are sought after, rather than typical semiconductors (e.g. Si, n = 1.5 x 10^{10} cm^{-3} at room temperature).[17] Degenerate semiconductors are a type of an extrinsic semiconductor, and have

large carrier concentrations due to high doping levels, with the Fermi level is located in either the conduction or the valence band.

The materials that satisfy the aforementioned criteria are known to possess 'phonon-glass electron-crystal' (PGEC) qualities.[18,19] PGEC refers to crystalline semiconductors that effectively scatter phonons (glass-like), and have the capability to easily transport charge carriers throughout the system (crystal-like).

1.2.1 Electrical Conductivity

The electrical conductivity (σ) of a material is given by

$$\sigma = ne\mu \tag{1-4}$$

where (n) is the number of charge carriers, (e) is the charge of the current carrier, and (μ) is the carrier mobility.[20] Materials such as insulators, (degenerate) semiconductors, and metals can be characterized by their electrical conductivity as a function of temperature (positive or negative temperature dependence).[21] The target carrier concentrations are in the range of 10^{19} cm^{-3} to 10^{21} cm^{-3}. This broad range includes materials such as the typical semiconductor, as well as those that are heavily doped (degenerate).

The carrier concentration is an important parameter, as it is material dependent, and will dictate the behavior of not only the electrical conductivity, but also the thermopower and thermal conductivity. Those materials with smaller carrier concentrations (e.g. $n < 10^{19}$ cm^{-3}) tend to exhibit a positive temperature dependence of the electrical conductivity. However, when the carrier concentration is much larger (e.g. 10^{21} cm^{-3}), the charge carriers will be scattered by each other, and therefore a negative temperature dependence of the electrical conductivity will be

observed. Therefore, at higher carrier concentrations and temperatures, the electrical conductivity is governed by the mobility of the carrier and is given by:

$$\mu_e = e\tau/m = el/m^*v \tag{1-5}$$

where (τ) is the time between collisions, (m^*) is the effective mass of an electron, (l) is the mean free path, and (v) is the velocity of the itinerant electrons. As the temperature increases, electrons can also be scattered by phonons, which reduces their mean free path ($l \propto \frac{1}{T}$) and decreases the mobility ($\mu_e \propto T^{-3/2}$).

In order to obtain a competitive zT, it is desirable to have a large electrical conductivity σ (Eq. 1-3), but how large σ should be is material-dependent. For example, materials that exhibit a positive, exponential temperature dependence (intrinsic semiconductors), tend to have low carrier concentrations, as well as low electrical conductivity values (< 100 $\Omega^{-1}cm^{-1}$). It is not uncommon to use a strategy such as doping, to increase the number of carriers (extrinsic semiconductors). Those materials with higher carrier concentrations exhibit negative temperature dependences, and can be observed to have electrical conductivities > 100 $\Omega^{-1}cm^{-1}$ and even above 1000 $\Omega^{-1}cm^{-1}$.

1.2.2 Seebeck Coefficient

The Seebeck coefficient (also known as the thermopower) is best described by the Seebeck effect, which results from the build-up of charges across a temperature gradient. It was found that by joining two dissimilar metals and applying a temperature gradient, an electrical current would form between the two junctions as well as a magnetic field.[22] The thermopower (S) can be defined as

$$S = \frac{\Delta V}{\Delta T} \tag{1-6}$$

where (V) is the voltage. The Seebeck coefficient can also be described as the ratio of a charge carriers' entropy to its charge.

To understand this phenomenon in more depth, the Seebeck coefficient is characterized by two potentials, one being electrical, and the other thermal. These two potentials are related by the Gibbs free energy of a system

$$dG = -\boldsymbol{S}dT + \boldsymbol{\mu}dN \tag{1-7}$$

where (G) is the Gibbs free energy of a charge carriers, ($\boldsymbol{S}$) is entropy, ($\boldsymbol{\mu}$) is the chemical potential, and (N) is the total number of charge carriers. As the temperature changes, the chemical potential within the system also changes, and this behavior is described as

$$\frac{\partial \boldsymbol{\mu}}{\partial T} = -\frac{\partial \boldsymbol{S}}{\partial N} = -\boldsymbol{\theta} \tag{1-8}$$

where ($\boldsymbol{\theta}$) represents the entropy per charge carrier. Thermoelectric materials are studied by inducing a temperature gradient, in which one side is the "hot end" (T_1) and the other the "cold end" (T_2). The chemical potentials of the charge carriers in regions of T_1 and T_2 are therefore different. These differences in chemical potentials can be translated into a voltage potential, in which

$$\Delta\Phi = \frac{\Delta\boldsymbol{\mu}}{q} \quad \text{or} \quad d\Phi = d\boldsymbol{\mu}/q \tag{1-9}$$

where (Φ) is the electrical potential and (q) is the amount of charge per charge carrier (this value is either positive or negative depending on whether the charge carriers are holes or electrons). The Seebeck coefficient can then be determined with both the electrical potential (voltage) and the thermal potential (temperature) to yield

$$S = -\frac{1}{q}\frac{\partial \boldsymbol{\mu}}{\partial T} = \frac{\boldsymbol{\theta}}{q} = \frac{\partial \Phi}{\partial T} \tag{1-10}$$

Determining the Seebeck coefficient for degenerate semiconductors however, is a more complicated matter. The thermopower can be determined utilizing the Mott equation:[23]

$$S = \frac{8\pi^2 k_B^2}{3eh^2} m^* T \left(\frac{\pi}{3n}\right)^{2/3} \quad (1\text{-}11)$$

where (k_B) is the Boltzmann constant and (h) the Planck constant. Optimally accessible *p*- and *n*-type Seebeck coefficients that are desirable are found as the Fermi level approaches the transport edge. It is well known that the distribution of charges around the Fermi level will change with an applied temperature gradient, which will either enhance or diminish the scattering of phonons.

1.2.3 Thermal Conductivity

The thermal conductivity describes the conduction of heat throughout a given material. The total thermal κ conductivity is comprised of two parts, κ_{latt} and κ_{el} which are the lattice and the electrical components respectively:[24]

$$\kappa = \kappa_{latt} + \kappa_{el} \quad (1\text{-}12)$$

The lattice contribution of the thermal conductivity, is based on the vibration of atoms within a crystal lattice, and due to this, is the only parameter that can be modified and not affect the previously mentioned properties (e.g. electrical conductivity and thermopower). One can estimate the minimum κ_{latt} as a starting point with the following equation: $\kappa_{latt} = \frac{1}{3} C_p v l$

where (C_p) is the material's specific heat capacity and (l) is the phonon mean-free-path. A material's specific heat capacity can be estimated using the following Dulong-Petit law:[25]

$$C_p = \frac{3R}{M} \quad (1\text{-}13)$$

where (R) is the universal gas constant and (M) is the average molar mass. The specific heat capacity can also be determined experimentally either by differential scanning calorimetry (DSC)[26] or from a low temperature set-up of a physical properties measurement system (see *Section 2.3.3*)

The lattice portion of the thermal conductivity can be reduced by increasing the amount of phonon collisions that occur, therefore reducing the amount of heat transported, which contributes to an overall lower total thermal conductivity. Scattering mechanisms that are utilized include introducing grain boundaries, impurity atoms and/or vacancies, and heavy atoms (restrict vibrations).

The electrical component of the thermal conductivity (κ_{el}) describes how the propagation of charge carriers throughout a solid affects the total thermal conductivity. Materials that exhibit metallic electrical conductivity have (κ_{el}) as the dominating component of the total thermal conductivity. The relationship between (κ_{el}) and the electrical conductivity is described by the Wiedemann-Franz law:

$$\kappa_{el} = L_0 T \sigma \tag{1-14}$$

where (L_0) is the Lorenz number.[27,28] The Wiedemann-Franz law states that the electrical and thermal conductivities of metals are proportional to each other at any given temperature such that:

$$\frac{\kappa}{\sigma T} \approx \frac{\pi^3}{3}\frac{k_B^2}{e^2} \tag{1-15}$$

The term on the left is equal to the Lorenz number, while the term on the right is the constant that is observed experimentally in most metals at room temperature. The Lorenz number can be estimated to be 2.44 x 10^{-8} WΩ K^{-2} for metals and 1.48 x 10^{-8} WΩ K^{-2} for semiconductors.[29] The Lorenz number can be sufficiently estimated with the equation:[29]

$$L_0 = \{1.5 + exp\left[-\frac{|S|}{116\ \mu V/K}\right]\}10^{-8} V^2 K^{-2} \quad (1\text{-}16)$$

By determining the value of the Lorenz number, a more accurate κ_{el} can be estimated, and therefore a more precise κ_{latt} can be determined by

$$\kappa = \kappa_{el} + \kappa_{latt} \quad (1\text{-}17)$$

after κ is determined experimentally.

Different approaches can be taken to obtain a low total thermal conductivity. These methods can include utilizing materials with complex crystal structures (anisotropy), nanostructuring, and the introduction of heavy elements.

1.3 High Performance Thermoelectric Materials

The overall performance of the best thermoelectric (TE) materials has increased over the past couple of decades, as new strategies as well synthetic methods have paved the way for achieving zT values above unity. While (properly modified) Bi_2Te_3[30] still holds the benchmark for thermoelectric properties around room temperature, other materials such as SnSe[31] and $AgPb_{18+x}SbTe_{20}$[32] are very competitive TE materials at elevated temperatures. The bulk materials of the aforementioned compounds have been further studied and enhanced through nanostructuring.[32–36]

As previously mentioned, it is difficult to modify a single parameter that determines the figure of merit. For example, the parameters σ, S, and κ are all directly affected by the carrier concentration. Enhancements to TE materials are routinely performed with the addition of dopants in order to achieve the desired carrier concentration. However, if the carrier concentration is increased, σ will also increase (which is desirable), but this will negatively impact S, which will

decrease and κ which will increase. By nanostructuring, it is possible to decouple these three parameters by modifying the mean free path lengths of electrons and phonons to different extents.[37] Nanostructuring is a method used to either implement nanostructures (e.g. nanodots) within a matrix, or nanostructuring the material itself (such as the formation of nanocrystals or thin films). These nanostructures have dimensions between 1 nm to 100 nm. For thermoelectrics, if grain boundaries are introduced, phonons would be more effectively scattered, while the mean free paths of electrons would ideally remain unaffected. This strategy is described as energy filtering and is depicted in Fig. 1.2.

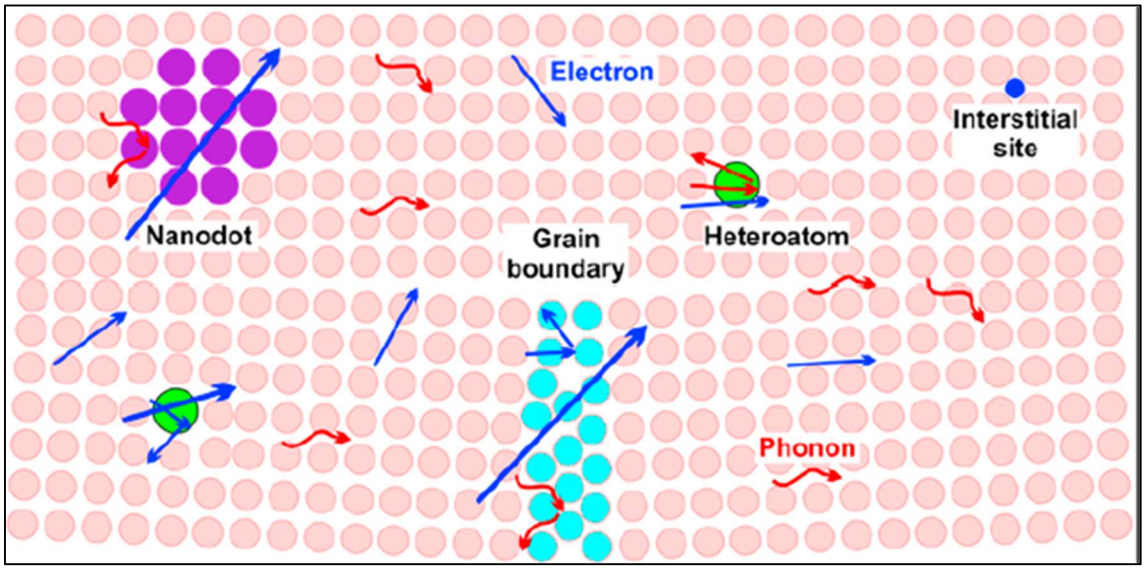

Figure 1.2. Schematic view of a heteroatom, a nanodot, and a grain boundary in a regular crystal differently impeding electrons and phonons with different mean free paths (energies). (Reproduced with permission from Academic Press)[37]

Atomic defects such as interstitial sites are effective at scattering short wavelength phonons. Grain boundaries and embedded nanoparticles are effective at filtering out low energy phonons, but allow high energy phonons to pass. This results in the decrease in total thermal conductivity, but the electrical conductivity and thermopower would experience no change.

1.3.1 Bi_2Te_3 and SnSe

Two examples of high-performance thermoelectric materials are Bi_2Te_3 and SnSe. Bi_2Te_3 is known for its exceptional thermoelectric properties ($zT > 1$) between 300 K and 400 K as well as the ease of being doped to become either an *n*- or *p*-type semiconductor.[30] One characteristic which lends itself to having a low thermal conductivity is the layered crystal structure. Bi_2Te_3 crystallizes in the rhombohedral space group $R\bar{3}m$ with alternating layers of - Te-Bi-Te-Bi-Te - along the *c* axis (Fig. 1.3). It is worthwhile to note that due to the anisotropy of Bi_2Te_3, the thermoelectric properties are directionally dependent. All Bi atoms are octahedrally coordinated to six Te atoms, while the Te atoms in the central layer are coordinated by six Bi atoms. The Te atoms that are contained in the first and fifth layers are coordinated to only three Bi atoms.

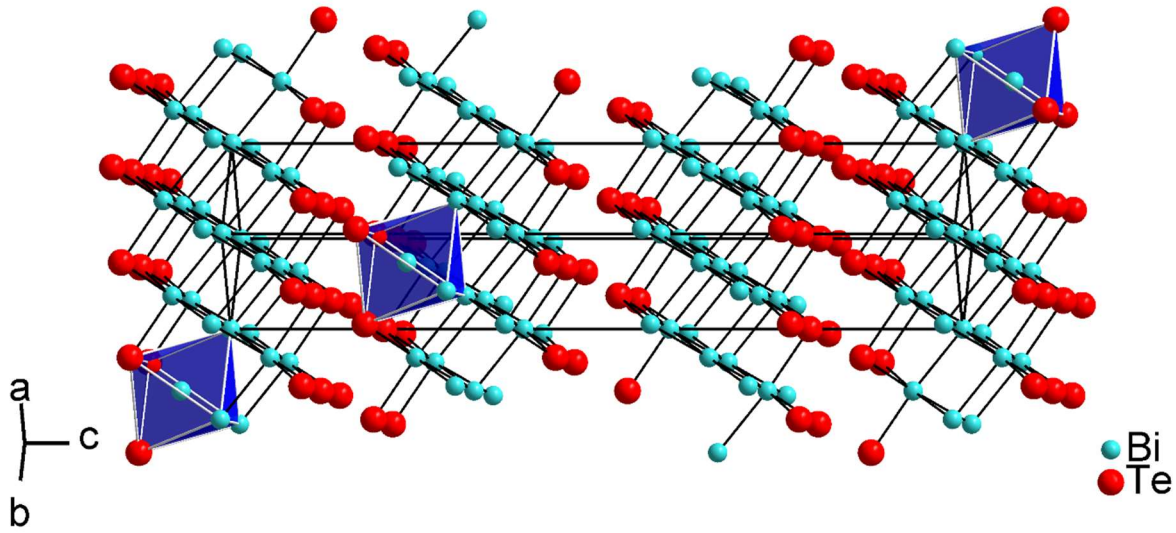

Figure 1.3. Crystal structure of Bi_2Te_3.

Semiconducting *p*-type Bi_2Te_3 can be achieved by alloying with Sb to give a bulk material with excellent thermoelectric properties between 300 K and 525 K.[38,39] A negative temperature dependence was also observed for the electrical conductivity with values of 1000 $\Omega^{-1}cm^{-1}$ – 400

$\Omega^{-1}cm^{-1}$ from 300 K to 525 K. These electrical conductivity values are desirable, where σ values > 1000 $\Omega^{-1}cm^{-1}$ are considered high, and values < 100 $\Omega^{-1}cm^{-1}$ are considered low. The Seebeck coefficient values observed are in the range of 150 μV K^{-1} – 230 μV K^{-1} with S_{max} being 230 μV K^{-1} at 375 K, which is desirable for thermoelectric materials that have *p*-type carriers.[10] Low thermal conductivity values of 1.3 W $m^{-1}K^{-1}$ (at 350 K) – 2.2 W $m^{-1}K^{-1}$ (at 525 K) were achieved. Overall, the figure of merit obtained was 1.0 at 325 K, making this material one of the higher performing TE materials at low temperatures.

When $Bi_{2-x}Sb_xTe_3$ was subjected to Sb nanoinclusions,[38] the electrical conductivity and Seebeck coefficient values were largely unaffected, while the thermal conductivity decreased even further down to 1.0 W $m^{-1}K^{-1}$ (at 375 K) – 1.2 W $m^{-1}K^{-1}$ (at 525 K). This resulted in a higher *zT* of 1.4 at 375 K. The thermal conductivity values of $Bi_xSb_{2-x}Te_3$ are regarded as being low, with κ values < 4 W $m^{-1}K^{-1}$ being desirable.

The high performance TE material, SnSe, has also been extensively studied due to the high *zT* values obtained by doping the material with transition metals as well as nanostructuring.[31] In 2014 Zhao et al. obtained an extraordinarily high *zT* of 2.6 with a single crystal of SnSe at 923 K, as well as an ultra-low thermal conductivity (< 1 W $m^{-1}K^{-1}$) value of 0.23 W $m^{-1}K^{-1}$ at 973 K along the *b*-axis.[40] The Seebeck coefficient values obtained were also high, ranging from 600 μV K^{-1} to 800 μV K^{-1} (between 300 K and 973 K), along with a very broad range of electrical conductivity values, ranging from 70 $\Omega^{-1}cm^{-1}$ to 800 $\Omega^{-1}cm^{-1}$ (from 300 K to 973 K).[40]

Like Bi_2Te_3, SnSe is also anisotropic, which yields high *zT* values along both the *b*- and *c*-axes. SnSe adopts a distorted rock salt structure type and crystallizes in the orthorhombic crystal

system. At room temperature, α-SnSe has a space group of *Pnma*, but upon heating to 750 K – 800 K, a phase transition occurs, resulting in the higher symmetry space group of *Cmcm* (β-SnSe).

The low temperature phase α-SnSe exhibits a double layered structure parallel to the *b,c*-plane (Fig. 1.4a). This double layered structure contains two-atom thick SnSe slabs which have strong Sn-Se bonds and weak Sn-Se bonding between the slabs along the *a*-axis (Fig. 1.4b). The structure also contains highly distorted $SnSe_7$ polyhedra, with three short Sn-Se bonds and four long Sn-Se contacts. In between the four long Sn-Se bonds, there is an Sn^{2+} lone pair. This $SnSe_7$ polyhedron allows for a disruption of phonon transport along the *a*-axis, which experiences weakly bonding Sn-Se interactions, and therefore is a factor in the ultra-low thermal conductivity.[40] Along the *b*-axis, the two-atom thick slabs creates a zig-zag pattern allowing for rigidity. The high temperature β-SnSe phase also contains two-atom thick slabs in which there are strong Sn-Se bonds; both Sn and Se are in a square pyramidal coordination with three short bonds (2.8 Å) and two long bonds (3.3 Å) between the atom pairs.

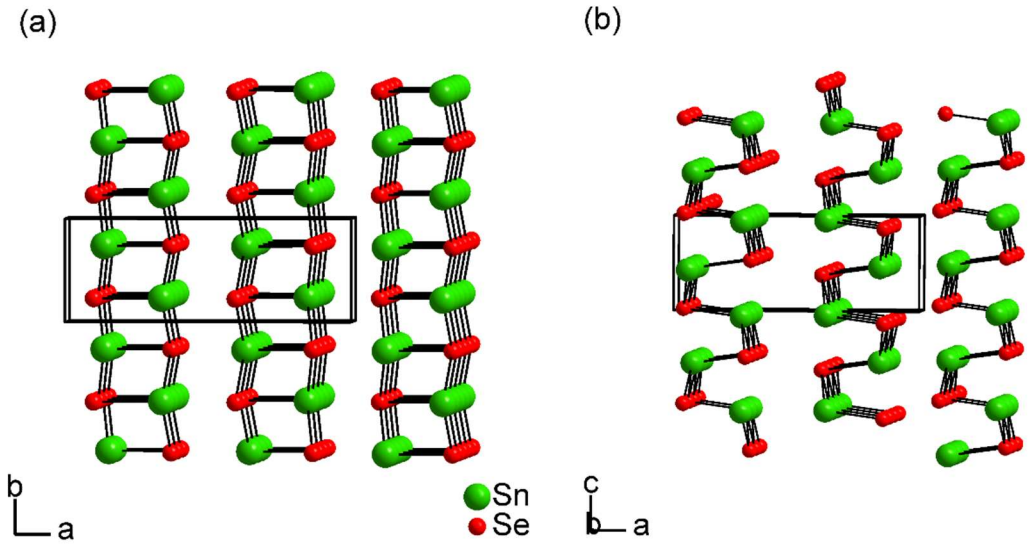

Figure 1.4. Crystal structure of α-SnSe viewed along the (a) *c*-axis and (b) *b*-axis.

1.4 Coinage Metal Chalcogenides as Thermoelectric Materials

In more recent years, thermoelectric materials synthesized from coinage metals (e.g. Cu, Zn, and Ag) have been a popular area of study. This is in part due to the constituent elements being relatively inexpensive and nontoxic. Many other high performance TE materials often contain toxic elements, such as PbTe[41,42] (zT = 1.4 at 750 K),[42] Sb_2Te_3[43,44] (zT = 1.4 at 400 K),[44] $Tl_2Ag_{12}Te_{7+\delta}$ (zT = 1.1 at 520 K),[45] and $Tl_{10-x}Pb_xTe_6$ (zT = 1.42 at 685 K).[46] These compounds benefit from the heavy, constituent atoms of Pb, Sb, Tl, and Te, which are contributors to the ultra-low (κ<1 W $m^{-1}K^{-1}$) thermal conductivity values (PbTe, κ = 0.8 W $m^{-1}K^{-1}$ at 750 K;[42] Sb_2Te_3, κ = 1.2 W $m^{-1}K^{-1}$ at 650 K;[44] $Tl_2Ag_{12}Te_{7+\delta}$ (κ = 0.22 W $m^{-1}K^{-1}$ at 520 K),[45] and $Tl_{10-x}Pb_xTe_6$ (κ = 0.45 W $m^{-1}K^{-1}$ at 685 K).[46]

Chalcogenides that contain Cu and Ag atoms, such as the chalcopyrites,[47–50] tetrahedrites,[51,52] and bornites,[53–55] have been studied due to their high zT values over a broad temperature range.[53,54] In particular, mixed ion-electron conductors (MIECs) such as $Cu_{2-x}Q$ (where Q = S, Se, and Te)[56,57] have been gaining more and more interest due to their utilization of the Phonon-Liquid-Electron Crystal (PLEC) concept.[58] These ionic conductors have excellent thermoelectric properties, but unfortunately are prone to degradation due to the movement of Cu^+ ions. The previously stated high performance Cu and Ag chalcogenides will be discussed in detail.

1.4.1 Copper Chalcogenides

Copper chalcogenides as thermoelectric materials encompasses a wide variety of materials, such as the chalcopyrites (ABQ_2, where A = Cu or Ag, B = 3+ cation, and Q = S, Se, Te),[47–50] colusites ($Cu_{26}E_2T_6S_{32}$, where E = Ge, Sn and T = V, Nb, Ta),[59] tetrahedrites ($Cu_{12-x}T_xSb_4S_{13}$ where T = Mn, Fe, Ni, Zn),[51,52] and bornites (Cu_5FeS_4).[53–55] In particular, the copper sulfides have been

studied extensively, due to their constituent elements being environmentally friendly and inexpensive. Although copper sulfides are inexpensive to synthesize and provide an advantage with respect to the economic component of manufacturing, the sulfides are problematic due to the degradation and instability of these compounds. The lack of stability affects the operating temperature, in which higher temperatures are inaccessible, as compared to other materials such as the perovskites[60] and half-Heusler materials.[61] As a consequence, copper sulfides tend to be utilized in the mid temperature range from 300 K to 700 K.

The previously mentioned $Cu_{2-x}Q$ adopt crystal structures with CuQ_4 tetrahedra. At higher temperatures a cubic phase is adopted, in which Cu atoms become highly disordered. When Cu deficient, the holes contribute as carriers, and as a result, the material exhibits *p*-type semiconductivity. Due to the large amount of disorder in the cubic phase, the thermal conductivity values tend to be very low.[58] Low thermal conductivity values coupled with desirable electrical conductivity values, lead to an overall high figure of merit.[62,63]

Kesterites are Cu-based quaternary chalcogenides (Cu_2ZnSnS_4) that are most known for their photovoltaic properties,[64] but have also been studied for their thermoelectric properties. This is due to the ease of doping to decrease the band gap (1 eV – 1.5 eV), and adding charge carriers (holes) in order to enhance the TE properties.[65,66] Kesterites crystallize in the ordered tetragonal space group $I\bar{4}$ and at higher temperatures will undergo a phase transition to the disordered $I\bar{4}m$ space group.[66] Kesterites can be described as having a diamond-like crystal structure with all atoms being tetrahedrally coordinated.[66,67]

Cu_2ZnSnQ_4 (where Q = S and Se)[68,69] was studied in 2009 by Liu et al. to determine the TE properties of the aforementioned compounds as well as $Cu_{2.1}Zn_{0.9}SnQ_4$.[69] Overall, the sulfide had very low electrical conductivity values (5 $\Omega^{-1}cm^{-1}$ – 26 $\Omega^{-1}cm^{-1}$ at 700 K) in comparison to the

high values of the selenide (750 $\Omega^{-1}cm^{-1}$ – 860 $\Omega^{-1}cm^{-1}$) for the undoped and doped samples, respectively. The overall increase in σ is caused by the hybridization of Cu 3*d* and Se 4*p* states at the top of the valence band, which creates new conduction pathways and increases carrier mobility. The Seebeck coefficient values for all compounds were low (50 μV K^{-1} to 200 μV $K^{-1}$from 300 K to 860 K) with the exception of Cu_2ZnSnS_4 (350 μV K^{-1} at 700 K). The thermal conductivity values were overall low (1 W $m^{-1}K^{-1}$ – 2.5 W $m^{-1}K^{-1}$ at 700 K), which is due to the alternating [CuQ_4] and [ZnQ_4] slabs within the crystal structure. The peak zT values obtained for both the doped sulfide and selenide were 0.36 and 0.45, respectively.

While the figure of merit values obtained were well below unity, there are aspects of the systems that are favorable. The electrical conductivity values of the selenides were high and desirable, however the Seebeck coefficients are too low. Another desirable trait is the low thermal conductivity, which has been attained before any nanostructuring was implemented. More recent efforts have included enhancing the TE properties through mechanochemical synthesis,[70] as well as hot-pressing nanocrystals.[71]

The colusites and the tetrahedrites have been found to have low thermal conductivity values, which can in part be attributed to the large amounts of atoms in the unit cells (66 and 58 atoms, respectively), as well as local distortions. Both materials crystallize in the cubic crystal system with the space groups of $P\bar{4}3m$ and $I\bar{4}3m$ for the colusite and tetrahedrite, respectively.

Like the kesterites, colusites ($Cu_{26}T_2E_6S_{32}$, where T = V, Nb, Ta and E = Ge, Sn) can also be described as having a diamond-like structure, which contains [CuS_4], [SnS_4], and [TS_4] tetrahedra. Finding alternatives for the toxic element vanadium in colusite materials while still retaining good TE properties has been a popular research topic.[59,72] Substituting tantalum for vanadium ($Cu_{26}Ta_2Sn_6S_{32}$) increased the electrical conductivity (200 $\Omega^{-1}cm^{-1}$ at 670 K), retained

the value of the Seebeck coefficient (200 μV K^{-1} at 670 K), but also decreased the thermal conductivity (0.6 W $m^{-1}K^{-1}$ at 670 K), yielding a high figure of merit of 0.8 at 670 K.[72] The reduction of the thermal conductivity was in part due to the existence of secondary phases (CuS and Cu_2S) as well as the heavy Ta atoms. The secondary phases affected the material in two ways. The first caused the colusite to be off stoichiometry, which increased the amount of charge carriers and therefore increased the electrical conductivity. The second is the physical presence of the binary sulfides, which effectively scatter phonons and decrease the thermal conductivity.

Tetrahedrites with the chemical formula of $A_{10}T_2X_4Q_{13}$ (A = Cu, Ag; T = a divalent, transition metal cation such as Cu, Co, Zn; X = As or Sb; and Q = S or Se) have also been studied.[51,52,73] Tetrahedrites with the composition of $Cu_{10}T_2Sb_4S_{13}$ have garnered a lot of attention due to the outstanding TE properties, as well as being less expensive (no Ag, Se) and toxic (no As, Se). In the crystal structure, Cu atoms occupy two distinct crystallographic sites: the first being tetrahedrally coordinated to S, and the second with Cu located in a planar triangle of S atoms. The S atoms also sit in two different crystallographic sites, in which they are tetrahedrally and octahedrally coordinated to Cu atoms. The Sb atom is coordinated to three S atoms in a trigonal pyramidal fashion and contains a lone pair. The low lattice thermal conductivity is in part a consequence of the lone pair effect on Sb^{3+}.[73] The lone pair generates anharmonic out of plane vibrations within the trigonal pyramidal Cu atoms. This leads to strong phonon scattering, and therefore low lattice thermal conductivity.

Published in 2018, Tippireddy et al. studied the TE properties of $Cu_{12-x}T_xSb_4S_{13}$ (where T = Mn, Fe, Co, Ni, Zn).[51] The variant with Co ($Cu_{11.5}Co_{0.5}Sb_4S_{13}$) obtained the highest zT of 0.98 at 673 K, in part due to the high band degeneracy that incurred around E_f due to the Co 3d states. An electrical conductivity of 670 $\Omega^{-1}cm^{-1}$ (comparable to the kesterites) was obtained at 673 K, as

well as a moderate Seebeck coefficient of 170 μV K^{-1}. A low thermal conductivity of 1.2 W $m^{-1}K^{-1}$ was observed at 673 K, due to the effect the lone pair effect of the Sb atoms. The affects that a lone pair may have on the anharmonicity of a crystal have been well studied in other materials, such as the rock-salt based crystal system of AXQ_2 (where A = Cu, Ag, and group I, X = As, Sb, Bi, and Q = S, Se, Te).[74] In tetrahedrites, the lone pair of the atom Sb participates with a weak bonding interaction with the trigonal planar Cu, which results in an out-of-plane anharmonicity, overall reducing the lattice component of the thermal conductivity.[75]

1.4.2 Barium Copper Chalcogenides

Due to the successes of Cu chalcogenides as TE materials, the use of Ba has been explored in order to reduce the thermal conductivity and to block the migration of Cu in MIECs. Compounds such as $Ba_{6.76}Cu_{2.42}Te_{14}$,[76] $Ba_2Cu_{4-x}Se_yTe_{5-y}$,[77] $BaCuSiTe_3$,[78] and most recently $Ba_3Cu_{16-x}Se_{11-y}Te_y$,[79] have been studied for their potential uses as thermoelectric materials. All of these materials exhibit recognizable Cu chalcogenide attributes, such as tetrahedral frameworks, and *p*-type semiconductivity within moderate temperature ranges (300 K – 600 K). To date, the best performing barium copper chalcogenides are $Ba_3Cu_{16-x}(S, Te)_{11}$ and $BaCu_{6-x}Se_{1-y}Te_{6+y}$, both of which have zT values close to unity.[80–82]

The material $Ba_3Cu_{16-x}(S,Te_{11})$ crystallizes in the rhombohedral $R\bar{3}m$ space group and has an extensive network of Cu-Cu contacts, forming Cu_{26} clusters. The structure also contains a 3-D network of corner-, edge-, and face-sharing CuQ_4 (where Q = S or Te) tetrahedra. All Cu positions in the structure are deficient, and therefore it was speculated that there could be a possibility of mobile Cu^+ ions. Finally, the Ba atoms sit in the center of the bicapped trigonal prismatic voids formed by the chalcogen atoms.[83]

The electrical conductivity and thermopower values for $Ba_3Cu_{15.3}S_{7.5}Te_{3.5}$ (125 $\Omega^{-1}cm^{-1}$ – 150 $\Omega^{-1}cm^{-1}$ and 130 $\mu V\ K^{-1}$ – 175 $\mu V\ K^{-1}$ between 300 K – 750 K respectively) were moderate compared to other Cu chalcogenides. The electrical conductivity exhibited a negative temperature dependence from 300 K to 535 K, because of the decreasing mobility. Above 535 K, the increasing amount of intrinsic charge carriers began to change the temperature trend, yielding a positive temperature dependence up to 653 K. At temperatures above 653 K appeared to be yet another turn-around, in which the electrical conductivity decreased, which was believed to be due to the materials reaching a softening point. Ultra-low thermal conductivity was observed throughout the temperature range of 300 K – 750 K of < 0.4 $W\ m^{-1}K^{-1}$, which could be attributed to the complex crystal structure, as well as the combination of Cu atom deficiencies and the mixing of Se/Te sites. The figure of merit for $Ba_3Cu_{15.3}S_{7.5}Te_{3.5}$ reached 0.88 at 750 K, making it a competitive thermoelectric material.[80]

The material $BaCu_{5.9}SeTe_6$ crystallizes in the cubic $Pm\bar{3}$ space group and contains Cu–Cu bonds that make up Cu_{8-x} cubes with the chalcogen atom residing in the center. There are also Te_2^{2-} dumbbells connecting the Cu_{8-x} cubes to a three-dimensional covalent network. The Ba atoms are located at the center of the Cu_8Te_{12} pentagonal dodecahedra.[81]

The electrical conductivity of $BaCu_{5.9}SeTe_6$ displayed a negative temperature dependence with values between 250 $\Omega^{-1}cm^{-1}$ – 100 $\Omega^{-1}cm^{-1}$ (300 K – 580 K). The negative temperature dependence is a consequence of the carriers being scattered due to a relatively high carrier concentration (~3 x 10^{20} cm^{-3}). These values are comparable to $Ba_3Cu_{16-x}(S,Te)_{11}$ but still lower than other high performance Cu chalcogenides. The Seebeck coefficient of $BaCu_{5.9}SeTe_6$ exhibited slightly higher thermopowers when in comparison to $Ba_3Cu_{16-x}(S,Te)_{11}$, with a thermopower of 150 $\mu V\ K^{-1}$ – 200 $\mu V\ K^{-1}$ (300 K – 580 K). The thermal conductivity values

within the temperature range of 300 K – 580 K were < 1 W $m^{-1}K^{-1}$, with the lowest value being 0.5 W $m^{-1}K^{-1}$ at 580 K. Ultimately a high *zT* of 0.81 was obtained at 600 K, overall making Cu chalcogenides containing Ba a potential family of competitive mid temperature ranged TE materials.[81]

1.4.3 Mixed Ion-Electron Conductors

Mixed ion-electron conductors (MIECs) have been implemented for various applications, with the most notable being batteries and solar cells.[84] The potential of MIECs ($Cu_{1.97}Ag_{0.03}Se_{1+y}$) for thermoelectrics have been investigated by NASA in the 1970's, but the studies were abandoned due to a lack of stability.[3] It was reported that due to the copper ion migration, the material was inhomogeneous with Cu- and Ag-rich areas formed. At higher temperatures selenium would evaporate due to the lack of Cu, and as a result, Cu solid is precipitated. More recently, researchers have been taking a second look at these materials, due to the high figure of merit values that have been achieved. Strategies to prevent the degradation of these materials, as well as understanding the mechanisms of Cu ion movement of the mixed carrier systems, have been devised in order to synthesize stable and competitive thermoelectric materials.[85]

Some materials that are characterized as MIECs can be described as having two sublattices. The first is comprised of one type of atom that is fixed and forms a crystalline lattice, and the second in which a different type of atom forms a 'liquid-like' sublattice. This 'liquid-like' sublattice is made up of highly mobile ions that can diffuse through the empty sites of the rigid lattice.[86] Materials with mixed ionic and electronic carriers have been coined as to having 'phonon-liquid electron-crystal' (PLEC) properties. Some examples of PLEC materials with

potential for thermoelectric applications are $Cu_{2-x}Q$ (Q = S, Se, Te),[58] Ag_2Se,[58] Ag_8SiSe_6,[87] Cu_7PSe_6,[88] and $Cu_{12}Sb_4S_{13}$.[89]

Compounds with highly mobile Cu^+ and Ag^+ ions exhibit ultra-low thermal conductivity values as a result of the reduction in specific heat capacities, as well as unprecedented high figures of merit ($zT > 2$).[90] Although the TE properties are excellent, stability and degradation due to the highly mobile atoms have proven to be problematic. Cu^+ ions have been observed to deposit as Cu metal on the surface of the materials, which leads to negative effects on the thermoelectric performance.[85,91] Recent studies have attempted to restrict Cu^+ ion movement by creating ion blocking interfaces such as grain boundaries or the insertion of large atoms.[81,85]

1.4.3.1 $Cu_{2-x}S$ and $Cu_{2-x}Se$

Binary copper chalcogenides have been studied for their potential thermoelectric applications since the 1960s by various entities, one example being NASA.[3] As previously stated, issues with degradation and stability have caused these projects to be abandoned, despite the excellent thermoelectric performance. However, because of the high performance of these materials, researchers have recently been studying ways to improve the stability, through understanding the various mechanisms involved in Cu^+ ion transport.[85]

The high temperature crystal structures of $Cu_{2-x}Q$ (where Q = S, Se, and Te) are complex, which is one of the major causes that yields low thermal conductivity values. All three compounds exhibit phase transitions, albeit the number of transitions and the temperature at which the transition occurs is different. Although $Cu_{2-x}Te$ is considered a MIEC, the thermoelectric properties are not as favorable when compared to the sulfide and the selenide, and will therefore not be discussed here.[57]

Copper sulfide undergoes two phase transitions. At temperatures below 370 K, Cu_2S crystallizes in the monoclinic space group $P2_1/c$ (α-phase), and above 370 K in the hexagonal $P6_3/mmc$ (β-phase). The second phase transition occurs around 700 K, beyond which Cu_2S adopts the high temperature $Fm\bar{3}m$ cubic structure (γ-phase). Copper selenide undergoes one phase transition around 400 K from the α-phase to the high temperature $Fm\bar{3}m$ cubic structure, the γ-phase.[92,93] As of late there is still no agreement on the crystal structure of the α-phase of Cu_2Se, due to multiple variants being found.[58,93] The high temperature cubic phases of Cu_2S and Cu_2Se can be described as the antifluorite structure type with Cu occupying the tetrahedral sites and S/Se forming an ordered rigid sublattice.

Due to the Cu positions being highly disordered within the cubic phases, both $Cu_{1.97}S$ and Cu_2Se have impressive thermoelectric properties (peak $zT > 1$). Both materials exhibit fairly low electrical conductivity values in comparison to other high-performance Cu chalcogenides (Cu_2S, $\sigma = 100\ \Omega^{-1}cm^{-1}$ at 1000 K; Cu_2Se, $\sigma = 130\ \Omega^{-1}cm^{-1}$ at 1000 K). The thermopower, however, is high for both the sulfide and selenide in comparison to the typical Cu chalcogenide, with 300 $\mu V\ K^{-1}$ being obtained for both compounds at 1000 K. Due to the 'liquid-like' nature of both materials, ultra-low thermal conductivity values were exhibited at 1000 K (Cu_2S, $\kappa = 0.6\ W\ m^{-1}K^{-1}$ at 1000 K; Cu_2Se, $\kappa = 0.8\ W\ m^{-1}K^{-1}$ at 1000 K). Ultimately, the figure of merit exceeds unity for both compounds (Cu_2S, $zT = 1.7$ at 1000 K; Cu_2Se, $zT = 1.5$ at 1000 K).[58,94]

As previously mentioned, while these TE properties are impressive, there are still many improvements that are necessary in order for $Cu_{2-x}Q$ to be competitive as TE materials. Problems with stability still exist even with the modifications of the temperature gradients and current. While the 'ion hopping' mechanisms have been elucidated, the prevention of ion migration

through the use of ion blocking interfaces is still insufficient. Future efforts to enhance the stability of these materials should be a priority.[93,95]

1.4.3.2 Argyrodites and Canfieldites

The argyrodite family[96] encompasses a large variety of compounds with the general formula of A_8EQ_6 (where A = Cu, Ag, E = Si, Ge, Sn, and Q = S, Se, Te) and have been studied for their potential uses in solid-state batteries,[97] photovoltaics,[98] and thermoelectric materials.[87,88,99,100]

These materials, like other mixed ion-electron conductors, all exhibit ultra-low thermal conductivity values at elevated temperatures due to a high temperature cubic phase in which the anion forms a rigid lattice, and the cations (e.g. Cu^+, Ag^+) occupy a number of cation deficient sites. The presence of multiple deficient sites as well as weak cation-anion (e.g. Ag-Se) bonding throughout the lattice allows for highly mobile cations, giving rise to 'liquid-like' behavior.[58] A brief summary of the space groups and phase transition temperatures for selected argyrodites can be seen in Table 1.1.

Table 1.1. Space groups and phase transition temperatures of selected argyrodites

Compound	Space group (LT)	Space group (HT)	Phase transition temp.	Ref.
Ag_8SiS_6	$Pna2_1$, $P\bar{1}$	n/a	n/a	96,101,102
Ag_8SiSe_6	$I\bar{4}m2$, $P4_232$	n/a	n/a	96,101,102
Ag_8SiTe_6	$Pm3m$ (163 K)	$F\bar{4}3m$	293 K	103
Ag_8GeS_6	$Pna2_1$	$F\bar{4}3m$	488 K	96,104,105
Ag_8GeSe_6	$Pba2$, $Pmn2_1$	$F\bar{4}3m$	473 K	96,102
Ag_8GeTe_6	$R3$	$F\bar{4}3m$	400 K	102,106
Ag_8SnS_6	$Pna2_1$	$F\bar{4}3m$	421 K	96,100
Ag_8SnSe_6	$Pmn2_1$	$F\bar{4}3m$	356 K	96,107
*Ag_8SnTe_6	n/a	n/a	n/a	108,109

*Not thermodynamically stable

The material Ag_8SnSe_6 is an *n*-type semiconductor and has been reported to exhibit ultra-low thermal conductivity from ~0.2 W $m^{-1}K^{-1}$ to 0.45 W $m^{-1}K^{-1}$ over the temperature range of 300 K – 700 K and a high zT value of ~1.1 at 700 K.[99] These values are attributed to the low lattice thermal conductivity, which is a direct consequence of a low sound velocity (~1500 m s^{-2}).[110] Doping and alloying studies have been performed in order to enhance the thermoelectric properties, where $(Ag_{1-x}Nb_x)_8SnSe_6$[111] and $Ag_{8-x}Cu_xSnSe_6$[112] have also displayed excellent zT values of 1.1 at 800 K and 0.85 at 645 K, respectively.

The canfieldite Ag_8SnS_6 (bulk sample) has been reported to have a peak zT of 0.5 at 750 K.[100] Ag_8SnS_6 as a thin film produced an even higher figure of merit of 0.55 at room temperature.[113] Like $Cu_{2-x}Q$, for the canfieldite to be a competitive thermoelectric material, the stability should be explored, as well as the thermoelectric properties further enhanced.

1.5 Scope of this Thesis

It can be ascertained from the introduction that coinage metal chalcogenides not only exhibit excellent thermoelectric properties, but also have the potential to be competitive thermoelectric materials. In order to improve these materials, different strategies were implemented (e.g. alloying, doping) as well as utilizing the intrinsic characteristics (e.g. complex crystal structures, heavy atoms). Three different materials were examined in this thesis: $Cu_5Sn_2Q_7$ (where Q = Se, Te), $Ba_3Cu_{14-\delta}Te_{12}$, and Ag_8SnS_6, which will be discussed in Chapters 3, 4, and 5, respectively.

The third chapter discusses the material $Cu_5Sn_2Q_7$. Previously, $Cu_5Sn_2Se_7$[114,115] and $Cu_5Sn_2Te_7$[116] were shown to exhibit large electrical conductivity and low thermopower values, the latter being detrimental for thermoelectric materials. The strategy employed was to dope each

compound with Zn, in an effort to increase the thermopower, which could ultimately lead to a higher figure of merit.

The fourth chapter discusses the compound $Ba_3Cu_{14-\delta}Te_{12}$,[117] which was originally discovered and characterized by the Kleinke group in 2006. The initial study determined $Ba_3Cu_{14-\delta}Te_{12}$ to have relatively promising thermoelectric properties (such as high electrical conductivity). However, there was no relationship (or trend) observed between the TE properties and the varying copper deficiencies across multiple samples. This could be attributed to the samples being cold-pressed, and the grain boundary effects dominating over all other trends. This chapter exhibits a proper correlation between hot-pressed copper deficient samples and the electrical conductivity, as well as a previously missed phase transition. A high temperature study of the TE properties was performed to investigate the potential Cu^+ movement, as with other barium copper chalcogenides. Lastly, in an attempt to improve the TE properties, a brief alloying study of Cu with Ag was performed.

The fifth chapter discusses the canfieldite Ag_8SnS_6. To date, only two studies on the thermoelectric properties of Ag_8SnS_6 have been published. The first involved a bulk sample,[100] and the second a thin film at room temperature.[113] As with the argyrodites, the canfieldite is expected to have mobile Ag^+ ions, which the previous studies do not report. This chapter addresses the stability issues of Ag_8SnS_6 with physical evidence of highly mobile Ag^+. Since Ag_8SnS_6 is a charge balanced and therefore an intrinsic semiconductor with very few charge carriers, the material of nominal composition $Ag_{8.1}SnS_6$ was explored. With the introduction of more Ag, the charge carrier concentration should increase, as well as the thermoelectric properties.

CHAPTER 2: Experimental Methods

2.1 Sample Preparation

2.1.1 Synthesis

All starting reagents were stored in an argon-filled MBRAUN glove box, with oxygen and moisture levels below 0.6 ppm and 0.1 ppm, respectively. The starting reagents were weighed inside the glove box in accordance with the appropriate stoichiometries of the targeted compounds. The compounds to be discussed were synthesized by either utilizing the traditional solid-state quartz tube method or through mechanochemical synthesis (ball-milling).

For the quartz tube method, the starting materials were loaded into fused silica tubes inside the glove box. The tubes were then transferred to a vacuum line, evacuated to 2×10^{-3} mbar, and sealed by a H_2/O_2 flame. The resulting ampoules were then placed into high temperature muffle furnaces. In the cases where the reagents reacted with the silica ampoule, the tubes were subsequently carbon coated on the inside. The heating profiles used varied with each targeted compound and will thus be discussed in each respective chapter.

For the mechanochemical synthesis, the starting materials were loaded into zirconia lined stainless-steel ball mill jars and zirconia balls were added. The jars were placed into a FRITSCH Pulverisette 7 planetary micro mill. The specific ball-milling details will be discussed in the appropriate chapter.

2.1.2 Densification

The resulting ingots from the ampoules were ground into powders. These and the powders from the ball mill were placed into a hardened graphite die with an inner diameter of 12.7 mm. The die was then placed into an Oxy-Gon FR-210-30T-ASA-160-EVC hot press furnace system under an atmosphere of argon. The particulars of the temperatures and weights used are unique to each compound and will be discussed in the appropriate chapter.

The density of each pellet was determined by using a Sartorius YDK01 density determination kit for analytical balances.[118] The Archimedes principle has historically been implemented in order to determine the density of irregularly shaped objects. This is done by submerging the object in a liquid in order to determine the buoyancy. The mass of the object in the liquid (M_f) is equal to the actual mass (M_a) of the object minus the mass of the water that is displaced. By knowing the density of the liquid (ρ_f), the volume of liquid that is displaced can be calculated, which is also equal to the volume of the object. With this information the density of the pellet (ρ_p) can be determined by the following equation:

$$\rho_p = \frac{M_a\left(\rho_f - 0.0012\ g\ cm^{-3}\right)}{\left(M_a - M_f\right) \times 0.99983\ g} + 0.0012\ g\ cm^{-3} \qquad (2\text{-}1)$$

The masses (M_a, M_f) have units of grams, while the density of the liquid (ρ_f) and the constant 0.0012 have units of g cm^{-3}. The constant 0.0012 g cm^{-3} is used as a correction factor for the buoyancy of air for the solid weighed in air, and 0.99983 g is the correction factor associated with the buoyancy of the wires of this particular kit. The liquid used to determine the~~all~~ densities for all compounds was water.

2.2 Sample Characterization

Multiple methods are typically used in order to characterize the synthesized materials. The two most widely used methods to gain insight into a solid's structure are single crystal and powder X-ray diffraction. Scanning electron microscopy (SEM) and energy-dispersive analysis of X-ray spectroscopy (EDAX) are also used to gain insight into elemental distribution, homogeneity, and the shapes and sizes of crystals. All four methods will be discussed in depth.

2.2.1 Powder X-Ray Diffraction

The purity and phases of each sample to be discussed in the following chapters were determined by an INEL X-ray powder diffractometer with a position-sensitive detector and Cu radiation source under the acceleration voltage and current of 30 kV and 30 mA, respectively. All powder patterns (PXRD) were collected in air at room temperature, with 2θ values between 5° and 120°.

Powder X-ray diffraction functions off of the principle that X-ray beams are diffracted by electrons in crystalline solids. To produce X-rays, a beam of high-energy electrons is aimed at a target metal, where it dislodges core electrons in the atoms creating an inner electron hole. Electrons from higher energy levels will fall into the vacancy, emitting electromagnetic radiation in the X-ray range with a specific energy. When targeting a crystal with a beam of monochromatic X-rays, the electrons of the atoms in the crystal will scatter those X-rays, and these reflections are measured in a detector. Since X-rays interact with the crystal planes in three dimensions, the translational symmetry of the crystal can be determined.

In crystalline systems with repeating structural units, the planes are parallel and equally spaced to each other, identified by Miller indices (h, k, l). The separation between the planes is

known as the *d*-spacing (d_{hkl}). The difference of the path length is dependent on two parameters: *d*-spacing (d_{hkl}) and the angle of incidence of the x-ray beam (θ), which is given by Bragg's Law[119] (Fig. 2.1):

$$2d_{hkl}sin\theta = n\lambda \tag{2-2}$$

where *n* is an integer and λ is the wavelength of the X-ray.

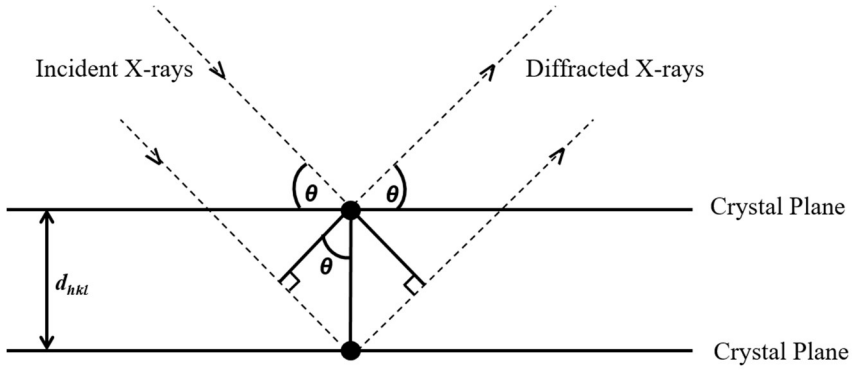

Figure 2.1. Depiction of Bragg's law that shows the constructive interference and scattering of X-rays.

The data collected at different angles of incidence, reported as theta values (θ) represent different sets of planes in the crystal lattice. The result is a diffraction pattern that exhibits a series of peaks of different positions and relative intensities.[120]

2.2.2 Single Crystal X-ray Diffraction

Single crystal X-ray diffraction is another analytical method used to characterize a solid-state material. This technique is not as widely used as powder diffraction because of the difficulty in synthesizing a single crystal of suitable size and quality (the crystal's largest edge should ideally be larger than 0.1 mm).

This method, similar to that of powder diffraction, involves the interaction of X-rays with the electrons of the atoms in a crystal structure, which in turn produces a diffraction pattern. The

diffraction pattern is a culmination of small spots, and each spot represents a reflection from the *d*-spacing between the planes.

The electron density map obtained results in structural information such as unit cell dimensions, crystal symmetry, and atomic positions, which provides useful information such as the bond lengths and angles.[120]

All single crystal information that is presented in the following chapters was obtained using a Bruker Kappa APEX II CCD, with a Mo Kα X-ray radiation at room temperature. The collected data was then treated for Lorenz and polarization effects by the APEX II software package (Bruker), followed by an absorption correction with the program SADABS embedded in the same software package.[121,122]

Thereafter, the structure can be solved via Direct Methods using the program SHELXS or taken from a previous publication. Subsequent refinements were carried out by using the least-squares method via SHELXL, in which the refinement was characterized by the unweighted and weighted factors 'R' and 'R_w' respectively, which is given by the following:

$$R(F_o) = \frac{\sum\left||F_o| - |F_c|\right|}{\sum|F_o|} \tag{2-3}$$

$$R_w(F_o^2) = \left[\frac{\sum[w(F_o^2 - F_c^2)^2]}{\sum[w(F_o^2)^2]}\right]^{1/2} \tag{2-4}$$

where F_o and F_c are the observed and calculated structure factors, respectively, and w is a weighting factor.

2.2.3 General Structure Analysis System (GSAS)

Analysis of X-ray powder diffraction data is commonly carried out through the use of the Rietveld refinement method.[123,124] This analytical technique uses a least squares approach in order to refine a theoretical profile fit that will best match the experimental data. Various experimental parameters are used in order to achieve the best fit between the experimental data and the model. If the crystal structure is unknown a 'pattern decomposition' is performed, in which the individually observed Bragg reflections and intensities are separately assigned in order to solve the structure. If a model of the crystal structure is known, then the Bragg reflections are fixed, and with known (model) intensities the observed intensities can also be refined more easily. These refinements are performed by the program 'General Structure Analysis System' (GSAS) and its graphical user interface EXPGUI.[125,126]

Before the refinement is performed, the experimental powder pattern must be converted into a format that the software can use. The intensities from the powder pattern are converted into numerical intensity values (y_i) at each increment (i) of the scattering angle (2θ). During the refinement, the least-squares fit determines all y_i values simultaneously.[124]

Important information is then extracted from the individual peaks of the powder diffraction pattern that is to be utilized during the least-squares refinement (such as peak position, height, width, etc.). The integrated area of the peak is proportional to the Bragg intensity (I_K), where K represents the Miller indices h, k, l for a Bragg reflection. Furthermore, (I_K) is proportional to the square of the structure factor (F_K). The Bragg reflections are used to determine the intensities of y_i at any given increment (i) of 2θ. The calculated intensities from a model (y_{ci}) are determined from the structure factor values ($|F_K|^2$) and summing the contributions from neighboring Bragg reflections and the background (within a designated 2θ range) as seen in Eq. 2-5:

$$y_{ci} = s\sum_{K} L_K |F_K|^2 \phi(2\theta_i - 2\theta_K) P_K A + y_{bi} \tag{2-5}$$

where s is the scale factor, L_K is the Lorentz, polarization, and multiplicity factors, ϕ is the reflection profile function, P_K is the preferred orientation function, A is the absorption factor, and y_{bi} is the background intensity at the i^{th} increment.

The Rietveld refinement method utilizes a least-squares approach.[124] In short, this technique is used to estimate the values that are variable dependent within a model ($M(\boldsymbol{x})$). In the case of the Rietveld refinement, information about the powder pattern (such as peak position, intensity, width etc.) of the observed data is modeled using the following:

$$M(S_i, \boldsymbol{x}) = b(S_i, \boldsymbol{x_b}) + \sum_{k=k_1}^{k_2} I_k(\boldsymbol{x_s}) \phi\left(S_i - S_k, \boldsymbol{x_p}\right) \tag{2-6}$$

where the background, structure, and peak shape parameters are $\boldsymbol{x_b}$, $\boldsymbol{x_s}$, and $\boldsymbol{x_p}$ respectively. The term S_i is given as $2\sin\theta_i/\lambda_i$ (where θ_i and λ_i are the angle and energy dispersive diffraction variables respectively). The background function is denoted as $b(S_i, \boldsymbol{x_b})$, while $I_k(\boldsymbol{x_s})$ is the integrated intensity of the kth Bragg reflection, and $\phi(S_i\text{-}S_k,\boldsymbol{x_p})$ is a peak shape function.

The goal is to continuously refine the dependent variables until the residuals (or offsets) are minimized (S_y), and therefore the model and observable data should coincide (Eq. 2-7)

$$S_y = \sum_i w_i (y_i - y_{ci})^2 \tag{2-7}$$

where w_i is $1/y_i$, and y_i and y_{ci} are the observed and calculated intensities at the ith step respectively. By using the calculated intensity values, the 'best fit' is obtained by the Rietveld refinement.

In order to ascertain the reliability of the Rietveld refinement typically the 'R-weighted value' (R_{wp}), the 'Goodness-of-fit' (S) and the 'Chi-squared' (χ^2) value are calculated.[124,127] The R-weighted value is determined by the following equation:

$$R_{wp} = \left\{ \frac{\sum w_i \left(y_i(obs) - y_i(calc) \right)^2}{\sum w_i \left(y_i(obs) \right)^2} \right\}^{1/2} . \quad (2\text{-}8)$$

The 'Goodness-of-fit' is calculated from R_{wp} and R_e ('R-expected') as:

$$S = \left[S_y/(N-P) \right]^{1/2} = R_{wp}/R_e \quad (2\text{-}9)$$

with R_e defined as:

$$R_e = \left[(N-P) / \sum w_i y_{i(obs)}^2 \right]^{1/2} . \quad (2\text{-}10)$$

The 'Goodness-of-fit' is then related to 'Chi-squared' as

$$\chi^2 = \left(R_{wp}/R_e \right)^2 . \quad (2\text{-}11)$$

In all cases where GSAS was used in this thesis, the structure types were known.

2.2.4 Scanning Electron Microscopy (SEM) and Energy Dispersive X-Ray Analysis (EDAX)

SEM and EDAX are surface techniques used to determine sample homogeneity, elemental distribution, as well as the morphology of solids.[20,128] The samples chosen for SEM and EDAX were analyzed using a FEI Quanta FEG ESEM (with EDAX) with an acceleration voltage of 20 kV. The results will be discussed in the respective chapters in this thesis.

SEM uses electrons that are thermionically emitted, usually from a tungsten filament (commonly known as an electron gun), and accelerated via high voltage. This beam of electrons is then focused into a small spot (typically 50 Å - 500 Å) on the surface of the sample. The electrons only penetrate a depth of a couple of microns, depending on the accelerating voltage and the type of material. Detection of secondary electrons is used to create images of samples consisting of lighter elements, whereas backscattered electrons are analyzed for samples consisting of heavier elements.

EDAX is possible if a SEM is equipped with an EDAX detector. When electrons from the electron gun hit the sample, electrons from the inner shell of the atoms will be ejected, and electrons from the outer shells will fall into the vacancy. This creates X-rays of characteristic wavelengths which in turn can be detected by the EDAX detector and analyzed. The analysis can determine which elements and approximate the ratios that are present in a material.

2.2.5 Density Functional Theory (DFT)

Density functional theory (DFT) is used to calculate the electronic structures of materials. Through the knowledge of the electronic structure, properties can be determined, as well as any contributions the electrons have to certain energy levels.[129] The basic principle of DFT focuses on the electron density (ρ).

DFT is based on the Hohenberg-Kohn theorems, as long as the electron system is not within a magnetic field. The first theorem postulates that the electron density determines the Hamiltonian operator, which uniquely coincides with the ground-state properties of the system. This can be achieved by solving the Schrödinger equation:

$$\hat{H}_{elec}\Psi_{elec} = E_{elec}\Psi_{elec} \tag{2-12}$$

where $\widehat{H}_{elec}$ is the electronic Hamiltonian, Ψ_{elec} is the electronic wave function, and E_{elec} is the total electronic energy of the system. The second theorem states that the ground state electron density can minimize the energy functional for a given system.

Coulombic interactions between electrons (exchange and correlation) are also important in determining the electronic band structure as stated earlier. To simplify this, the local-density approximation (LDA) can be utilized. This assumes that the exchange-correlation energy depends on the local density:

$$E_{XC}[\rho] = \int \rho(r)\varepsilon_{XC}[\rho(r)]dr \tag{2-13}$$

The assumption made in LDA is the electron density is uniform throughout, however in actuality this is known to not be completely true. This method as a result tends to underestimate the exchange energies and overestimate the correlation energies.

Instead, the band structures that are presented in this research were calculated utilizing the Perdew-Burke-Ernzerhof (PBE) generalized gradient approximation (GGA) method.[130] This method, unlike LDA, expands the gradient terms to allow for non-homogeneity of the electron densities. Although the GGA method is an improvement to calculate more accurate band structures, it is known to underestimate the band gap. In order to calculate more accurate band gaps, the Tran-Blaha modified Becke-Johnson (mBJ) potential was utilized. This is an approximation in which the 'exact exchange' correlation potential is used as a screening term. All calculations (DFT[131] and Boltzmann Transport Properties[23,132]) were performed using the Wien2k package.[133]

2.2.6 Boltzmann Transport Properties

The Boltzmann transport properties were calculated utilizing the BoltzTraP code within the Wien2K package.[134] The code uses a Fourier expansion of the band energies, in which the group symmetry always remains constant by utilizing star functions,

$$\mathcal{E}_i(\boldsymbol{k}) = \sum_{\boldsymbol{R}} c_{\boldsymbol{R}i} S_{\boldsymbol{R}}(\boldsymbol{k}) \quad , \quad S_{\boldsymbol{R}}(\boldsymbol{k}) = \frac{1}{n} \sum_{\{\Lambda\}} e^{i\boldsymbol{k}\cdot\Lambda\boldsymbol{R}} \tag{2-14}$$

where $\boldsymbol{R}$ is a direct lattice vector, and $\{\Lambda\}$are the n point group rotations. The Fourier expansion uses more star functions than band energies available. The fit is also constrained so that any extrapolated energies will always be exactly equal to the calculated band energies. The following roughness function ($\rho_{\boldsymbol{R}}$) was used and also continually minimized:

$$\rho_{\boldsymbol{R}} = \left(1 - C_1 \left(\frac{|\boldsymbol{R}|}{|\boldsymbol{R}_{min}|}\right)^2\right)^2 + C_2 \left(\frac{|\boldsymbol{R}|}{|\boldsymbol{R}_{min}|}\right)^6 \tag{2-15}$$

where $\boldsymbol{R}_{min}$ is the smallest nonzero lattice vector, and the parameters C_1 and C_2 are fixed to ¾. The last parameter needed for the code is sufficient freedom, in which the number of planewaves exceeds the number of band energies. From this, the expansion coefficients are calculated, and all of the information needed to generate an analytical representation of the band structure is complete.

A series of conductivity tensors are generated by simulating the materials in the presence of an electric and magnetic field as well as a thermal gradient, which gives the energy of the conductivity tensors:

$$\sigma_{\alpha\beta}(\mathcal{E}) = \frac{1}{N} \sum_{i,\boldsymbol{k}} \sigma_{\alpha\beta}(i,\boldsymbol{k}) \frac{\delta(\mathcal{E} - \mathcal{E}_{i,\boldsymbol{k}})}{d\mathcal{E}} \tag{2-16}$$

Where N is the number of $\boldsymbol{k}$-points. Fourier transformations are then used with the expansion of the band energies (see Eq. 2-16) to derive the transport tensors. With the transport tensors calculated the Seebeck and Hall coefficients are also calculated.

2.3 Physical Property Measurements

2.3.1 Electrical Conductivity and Seebeck Coefficient

The electrical conductivity and the Seebeck coefficient were obtained by using an ULVAC-Riko ZEM-3 unit. Hot-pressed samples were cut into bars with the dimensions of approximately 10 × 2 × 2 mm. The bar was set into the instrument between two electrodes with two probes (thermocouples) pressed against the side of the sample (Fig. 2.2).

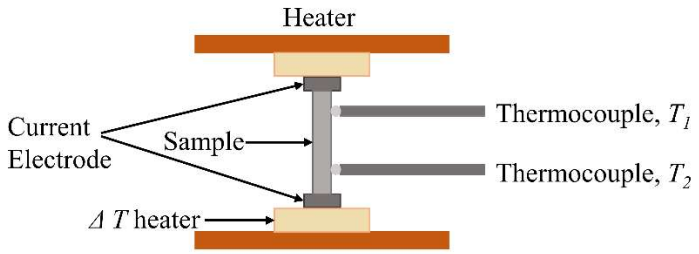

Figure 2.2. Schematic of the sample set up in the ULVAC-Riko ZEM-3.

The measurement was run under an atmosphere of ultra-pure helium. During the measurement, the sample was heated in a furnace to the target temperature, while the heater in the bottom block provided the desired temperature gradient. To measure the Seebeck coefficient,[135] the temperature difference was determined by measuring T_1 and T_2 by the respective thermocouples. The thermal electromotive force (dE) was then measured between the same type of wires within the thermocouples, which is a change in the voltage potential (dV). The thermopower is determined by

$$S = \frac{dV}{dT}. \tag{2-17}$$

The electrical resistance was measured by a four-probe method, in which a constant current (I) is provided through each electrode and the voltage difference (dV) between the same type of wires

within the thermocouples was obtained. Only the resistance (R) of the area between the two thermocouples is measured, which is found by

$$R = \frac{dV}{I}. \tag{2-18}$$

The electrical resistivity and therefore the electrical conductivity of the sample can then be determined by using Ohm's law:

$$\rho = R \cdot \frac{A}{D} = \frac{1}{\sigma} \tag{2-19}$$

where A is the surface area of the sample, and D is the distance between the thermocouples. The experimental errors of each measurement are estimated to be ±5% and ±5% for the electrical conductivity and Seebeck coefficient, respectively.

2.3.2 Determination of the Thermal Conductivity

In order to determine the thermal conductivity, the thermal diffusivity (α) was measured by utilizing a TA-Instruments DLF-1200 system. The hot-pressed pellets with diameters of 12.7 mm and heights of 2 mm were coated with graphite via an aerosol spray in order to promote homogenous heating, as well as better absorption and emissivity. The samples were then loaded into the instrument with the measurement taking place under an atmosphere of argon. During the measurement a laser-flash pulses the front face of the pellet and the temperature as a function of time (thermogram) is recorded at the rear face (Fig. 2.3).[24,136,137]

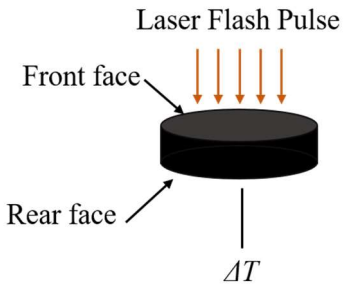

Figure 2.3. Depiction of the laser flash pulse hitting a sample for the thermal diffusivity measurement.

The thermogram is utilized to find the amount of time that it takes to reach half of the maximum temperature ($t_{1/2}$). The thermal diffusivity can then be determined by

$$\alpha = 0.1388 \frac{L^2}{t_{1/2}} \tag{2-20}$$

where L is the thickness of the pellet. The thermal conductivity can then be determined by

$$\kappa = \alpha \cdot c_p \cdot \rho \tag{2-21}$$

where c_p can be determined via the Dulong-Petit equation (Eq. 1-24) or experimentally, and ρ is the density of the pellet.[25] The experimental error for the thermal conductivity was estimated to be ± 5%.

Combining the electrical conductivity, Seebeck coefficient, and the thermal conductivity when calculating zT, the error was deduced to be ±10%.

2.3.3 Specific Heat Capacity Determination

The specific heat capacity can be determined with a Quantum Design PPMS Dynacool (WATLab) on a cube cut from the previously hot-pressed pellet.[138] The resulting cube had the dimensions of 2 x 2 x 2 mm (Fig. 2.4).

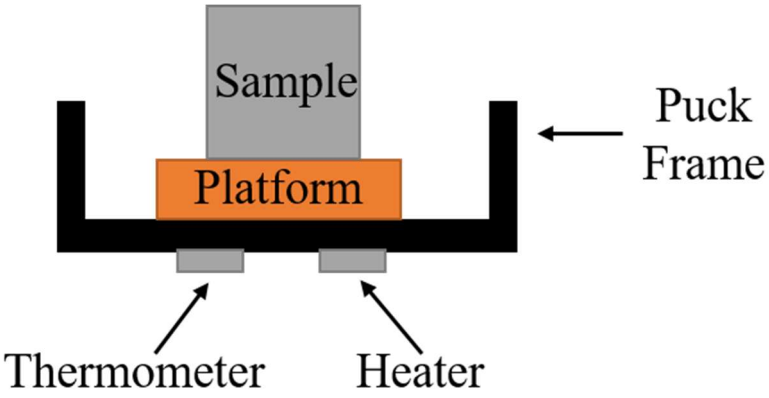

Figure 2.4. Depiction of the set-up for the specific heat capacity measurement.

The specific heat capacity software employs a two-tau method, in which the temperature response of both the sample and sample platform are simulated as a function of time. This method is used when poor thermal contact is established between the sample and the sample platform. The specific heat of the platform ($C_{platform}$) is determined by the heat flow between the sample platform and the puck:

$$C_{platform}\frac{dT_p}{dt} = P(t) - K_w\left(T_p(t) - T_b\right) + K_g\left(T_s(t) - T_p(t)\right) \tag{2-22}$$

and specific heat capacity of the sample (C_{sample}) is determined by the heat flow between the sample and the sample platform:

$$C_{sample}\frac{dT_s}{dt} = -K_g\left(T_s(t) - T_p(t)\right), \tag{2-23}$$

where $P(t)$ is the heater power, T_b is the temperature of the puck, K_g is the thermal conductance of the grease between the sample and sample platform, and $T_p(t)$ and $T_s(t)$ are the temperatures of the sample platform and the sample respectively. The data taken during the actual measurement is then fit to the two-tau model to determine the specific heat capacity.[138]

2.3.4 Thermogravimetry (TG) and Differential Scanning Calorimetry (DSC)

The two techniques thermogravimety and differential scanning calorimetry are typically coupled together and can provide useful information such as phase transitions. heat capacity, and mass changes as a function of temperature.[20] This data can be used to understand solid-state reactions (phase diagrams) and gain information about thermal stability. TG and DSC was performed using a NETZSCH STA 409 Luxx instrument.

Thermogravimetry measures the mass of a sample as a function of temperature. During this experiment, the sample is heated over a temperature range, in which it may experience an event such as a decomposition, in which the mass will change.

Differential scanning calorimetry is a way to record the enthalpy (*H*) change of a sample. During this experiment both the sample and reference (in this case sapphire) are held at the same temperature, and when a thermal event is experienced by the sample, the sample's temperature changes. This will cause the temperature of the sample to differ from that of the reference. In order to compensate for this temperature difference, the instrument then applies extra heat to the sample or the reference. This gives information about heat flow throughout the entire measurement.

2.3.5 Hall Measurement

The Hall coefficient and the nature of the charge carriers can be studied by performing a Hall measurement.[21,139] All Hall measurements were performed at the Department of Physics and Astronomy at the University of Waterloo (Kycia group). Hall data was collected at ambient conditions on bars with the dimensions of 8 x 2 x 1 mm, where the temperature was stabilized by a PID temperature controlled system equipped with a Peltier thermoelectric cooler. A four-wire

AC measurement system was employed with two SRS 830 lock-in amplifiers to obtain the electrical conductivity, with the current below 15 mA to minimize self-heating of the sample. Measuring the Hall voltage, V_H, with a 12 mA AC excitation current and an external magnetic field of 0.5 T yielded the Hall resistance, R_H. A PAR 190 transformer was used to improve the signal-to-noise ratio.

The Hall measurement is done by passing a current (I_x) through the smallest face of a rectangular bar, with a magnetic field (B_z) applied perpendicular to the direction of the current. This causes the charge carriers to drift to the sides of the bar, which generates an electric field (E_y) orthogonal to the current (Fig. 2.5).

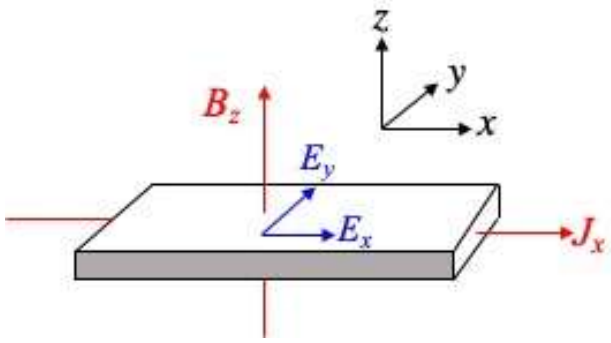

Figure 2.5. Depiction of the Hall measurement experiment.

The force on the holes generated by the electric field can be determined by the drift velocity (v_x) and the magnetic field

$$eE_y = ev_xB_z \tag{2-24}$$

where e is the charge of the charge carriers being studied. The current density (J_x) can be determined by

$$J_x = n_h e v_x. \tag{2-25}$$

The carrier density (*ne*) remains constant and is temperature independent and can be equated to the Hall coefficient (R_H) by

$$\frac{E_y}{B_z J_x} = \frac{1}{ne}. \tag{2-26}$$

In practice (Eq. 2-26) can be written as

$$R_H = \frac{V_y t_z}{B_z I_x} = \frac{1}{ne} \tag{2-27}$$

where V_y is the voltage drop as a result of the electric field, and t_z is the thickness. The Hall coefficient can be used to determine the density of the charge carriers, as well as the type (e.g. if R_H is negative, the electrons are the dominant charge carriers).

The largest errors in the carrier mobility and concentrations stem from the measurements of the dimensions, estimated to be below ±3%.

2.3.6. Low Temperature Electrical Conductivity Measurements

Low temperature electrical conductivity measurements were performed on pristine bars with the approximate dimensions of 10 x 2 x 2 mm. Cryogenic temperatures were achieved with a copper cold finger apparatus using a helium compressor. A standard 4-probe resistivity (see *Section 2.3.1*) method was used for the measurements with a Keithley 2400 SourceMeter and Agilent 34420 nanoVolt/micro-Ohm Meter. Temperature measurements were acquired through a Lake Shore Cryogenics 330 temperature controller.

CHAPTER 3:

Thermoelectric Properties of Zn-doped $Cu_5Sn_2Q_7$ (Q = Se, Te)

This chapter is reproduced in part with permission from Dalton Transactions:
Cheryl Sturm, Leilane R. Macario, Takao Mori, and Holger Kleinke, *Dalton Transactions*, **2021**, *50*, 6561-6567 (DOI: 10.1039/D1DT00615K).

3.1 Introduction

The ternary and quaternary Cu-based chalcogenides within the crystal family of $Cu_5M_2Q_7$ (Q = S, Se, Te) have seldom been reported in the literature until more recently. The earliest example was $Cu_4NiSi_2S_7$, described by Schäfer in 1980.[140] The crystal structures and thermoelectric properties of the compounds $Cu_5Sn_2Se_7$ and $Cu_5Sn_2Te_7$ were reported by Fan et al.in 2014[141] and Adhikary et al. in 2016,[116] respectively. Both groups concluded that both the selenide and telluride of $Cu_5Sn_2Q_7$ adopted a superstructure of the sphalerite phase, and crystallized in the $C2$ space group. All atoms are tetrahedrally coordinated, while Cu and Sn are surrounded by four Q atoms, while the chalcogen atom is surrounded by three Cu atoms and one Sn atom (Fig. 3.1).

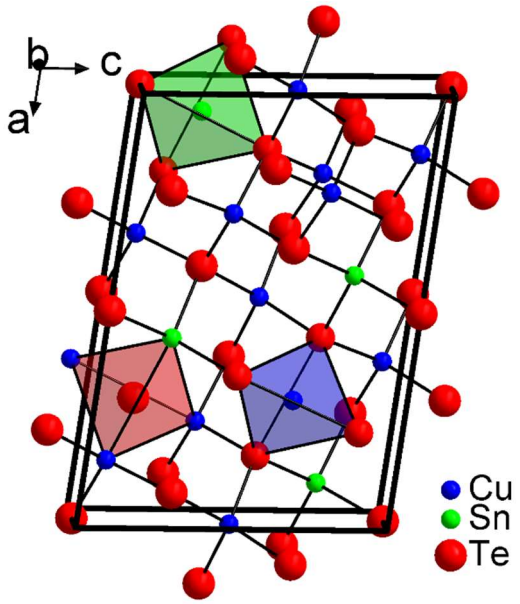

Figure 3.1. Crystal structure of $Cu_5Sn_2Q_7$, highlighting the coordination tetrahedra.

Both compounds were reported as exhibiting very low figure of merits, therefore a doping study was introduced in an effort to decrease the electrical and thermal conductivity in order to achieve more desirable *zT* values.

3.2 Sample Synthesis and Consolidation Parameters

All preparatory work was performed inside an argon-filled glove box to synthesize all four compounds, starting with stoichiometric amounts of Cu powder (99.5%, Alfa Aesar), Zn powder (99.9%, Alfa Aesar), Sn granules (99.9%, Aldrich), Se pellets (99.99%, Aldrich), and Te broken ingots (99.999%, Strem).

The compounds $Cu_5Sn_2Se_7$ and $Cu_4ZnSn_2Se_7$ were synthesized utilizing the traditional solid state tube method, in which the starting reagents were loaded into a fused silica tube, sealed under a dynamic vacuum of 2 x 10^{-3} mbar, and placed into a high temperature muffle furnace. The samples were then heated to 1173 K for 24 hours, and then annealed at 873 K for one week.

The compound $Cu_5Sn_2Te_7$ was prepared in the same fashion as the selenides, with the exception of a different heating profile. The starting reagents were heated to 923 K for four days and then cooled to room temperature. The resulting ingot was then ground into a powder, placed again into a fused silica tube, evacuated, and heated to 673 K for 72 hours, with agitation every 24 hours.

Finally, $Cu_4ZnSn_2Te_7$ was synthesized utilizing a planetary ball mill, in which starting reagents were loaded into ball milling jars (lined with zirconia) that contained 3 mm diameter zirconia balls. The ball to powder ratio was approximately 10:1. The reactions were run at 600 rpm for four hours. The resulting powders contained the target phase as well as some binary compounds, and were subsequently loaded into fused silica tubes, sealed under a dynamic vacuum and placed into a high temperature muffle furnace. The samples were then heated to 673 K for 72 hours with intermittent shaking, which resulted in a pure product. Attempts to make $Cu_4ZnSn_2Te_7$ utilizing the traditional solid state tube method failed to produce a phase pure sample. The powders were then consolidated at 563 K (selenide) and 453 K (telluride) under 46 mPa for three hours. The resulting pellets had the densities determined through utilizing the Archimedes method, and all materials exhibited densities > 95%. The pellets were then used for physical property measurements.

3.3 Results and Discussion

3.3.1. Characterization of Zn-doped $Cu_5Sn_2Q_7$ (Q = Se, Te)

Powder X-ray diffraction was implemented to determine the phase purity of all synthesized samples (Fig. A-1). No other side products were observed in the powder patterns and small changes were seen in the lattice parameters with the introduction of Zn (Table A-1). The powder

patterns for all materials were indexed to previously published powder patterns of $Cu_5Sn_2Se_7$ (ICSD Coll. Code 194592) and $Cu_5Sn_2Te_7$ (ICSD Coll. Code 291607), and all four compounds crystallized in the space group *C*2.

To further characterize the materials SEM and EDAX was performed on $Cu_4ZnSn_2Se_7$ and $Cu_4ZnSn_2Te_7$ in order to determine the homogeneity of the samples. The nominal compositions were determined by averaging three to four area scans on four pieces of the bars that were broken. The EDAX mappings (Figs. A-2 and A-3) showed that no other side products (e.g. binaries such as Cu_2Te and ZnTe) and impurities (e.g. Oxides, Si from reaction vessel) were detected. The mappings also show a homogenous distribution of elements throughout the scanned areas of the samples.

3.3.2 Thermoelectric Properties of Zn-doped $Cu_5Sn_2Q_7$ (Q = Se, Te)

The density of states of $Cu_5Sn_2Te_7$ is depicted in Fig. 3.2. The Fermi level cuts through the top of the valence band, composed of Cu-*d* and Te-*p* states. A narrow gap of 0.2 eV occurs about 0.5 eV above the Fermi level, predicting degenerate semiconducting properties for $Cu_5Sn_2Te_7$. Similar features were calculated for the isoelectronic and isostructural $Cu_5Sn_2Se_7$.[115]

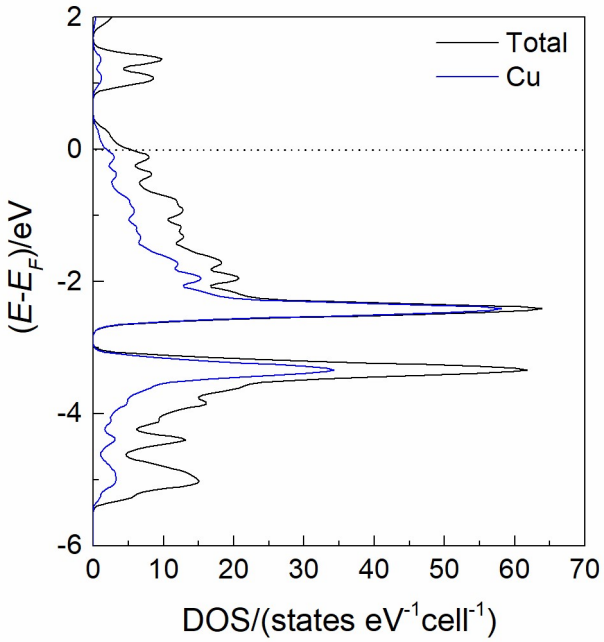

Figure 3.2. Density of states of $Cu_5Sn_2Te_7$.

Substituting one Cu site with Zn results in the formula $Cu_4ZnSn_2Te_7$, and moves the Fermi level into the band gap (Fig 3.3). Besides that shift, only minor changes occur between -2 eV and + 2 eV around the Fermi level. With that, semiconducting properties are to be expected for the charge-balanced $(Cu^{+})_4(Zn^{2+})(Sn^{4+})_2(Te^{2-})_7$.

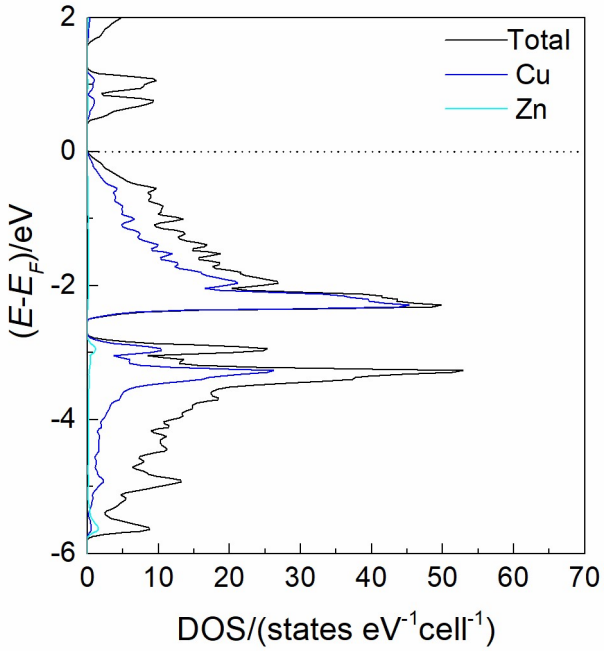

Figure 3.3. Density of states of $Cu_4ZnSn_2Te_7$.

The thermoelectric properties of the materials of nominal compositions $Cu_5Sn_2Se_7$ and $Cu_4ZnSn_2Se_7$ were studied in the temperature range of 300 K – 630 K, and of $Cu_5Sn_2Te_7$ and $Cu_4ZnSn_2Te_7$ from 300 K – 575 K. The temperature dependence of the electrical conductivity is displayed in Fig 3.4. Due to the location of the Fermi level in the valence band, a large amount of charge carriers for both ternary (Zn-free) compounds was observed earlier, namely ~3.0 x 10^{21} cm^{-3} and ~1.4 x 10^{21} cm^{-3} at 300 K for the selenide[141] and telluride,[116] respectively. Therefore, a decrease in the (high) electrical conductivity was expected for the ternaries with increasing temperature. This negative temperature dependence was indeed displayed, typical of heavily doped/degenerate semiconductors and metals, as the carrier concentration barely changes with temperature, and the charge carriers are more scattered with an increase in temperature, resulting in a decrease in carrier mobility. In the temperature range of 300 K – 630 K, electrical conductivity values of 8800 $\Omega^{-1}cm^{-1}$ – 3700 $\Omega^{-1}cm^{-1}$ were obtained for the selenide, while Fan et al. reported

24% lower electrical conductivity values within the same temperature range (6700 $\Omega^{-1}cm^{-1}$ – 2900 $\Omega^{-1}cm^{-1}$).[141] This is at least in part a consequence of Fan et al. obtaining higher porosity samples as determined from the lower relative density of 92%, compared to our 96%. These values are significantly higher than in other known diamond-like structures, such as Cu_2SnSe_3 (200 $\Omega^{-1}cm^{-1}$ – 100 $\Omega^{-1}cm^{-1}$), which also displayed the same negative temperature dependence.[142]

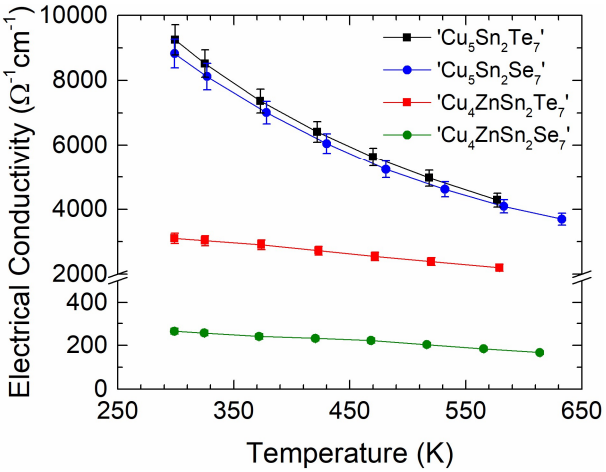

Figure 3.4. Temperature dependence of the electrical conductivity of '$Cu_5Sn\mathit{Q}_7$' and '$Cu_4ZnSn_2Q_7$' with 5% error bars.

Similarly, the electrical conductivity of $Cu_5Sn_2Te_7$ experienced a three-fold decrease from 9200 $\Omega^{-1}cm^{-1}$ to 3100 $\Omega^{-1}cm^{-1}$ at 300 K after the introduction of Zn. Our room temperature results on the ternary telluride are in qualitative agreement with the (low temperature) data from Adhikary et al. who reported an electrical conductivity of 9800 $\Omega^{-1}cm^{-1}$ at 300 K.[116] At 575 K, there was a roughly 50% reduction of the electrical conductivity with the inclusion of Zn, with values of 4300 $\Omega^{-1}cm^{-1}$ and 2200 $\Omega^{-1}cm^{-1}$, respectively. The same negative temperature dependence is observed for the kesterite $Cu_2CdSnTe_4$, but with higher electrical conductivity values (σ = 2500 $\Omega^{-1}cm^{-1}$ at 300 K to 1300 $\Omega^{-1}cm^{-1}$ at 600 K).[143] As such a dependence is indicative of extrinsic semiconductors, all of the above-mentioned materials have defects, likely Cu atom deficiencies,

that contribute to itinerant charge carriers. These conductivity values are also significantly higher than those of the chalcopyrite $CuInTe_2$ (σ = 22 $\Omega^{-1}cm^{-1}$ at 300 K to 70 $\Omega^{-1}cm^{-1}$ at 600 K), which does exhibit the positive temperature trend expected for intrinsic semiconductors.[48]

The temperature dependence of the Seebeck coefficient is displayed in Fig. 3.5. For all compounds, there is an increase in the thermopower with an increase in temperature, which is typical behavior for both degenerate and extrinsic semiconductors. The Seebeck coefficient for $Cu_5Sn_2Se_7$ was found to be +16 μV K^{-1} – +40 μV K^{-1} within the temperature range of 300 K - 630 K. These results are in good agreement with Fan et al., who reported values of +20 μV K^{-1} – +43 μV K^{-1}.[141] The intended and desired overall increase in the Seebeck coefficient was observed with the introduction of Zn, resulting in +80 μV K^{-1} – +165 μV K^{-1}. The Zn doped sample has values comparable to $Cu_2ZnSnSe_4$ (S = +50 μV K^{-1} – +110 μV K^{-1} from 340 K - 630 K)[70] as well as Cu_2SnSe_3 (S = +90 μV K^{-1} – +150 μV K^{-1} from 300 K – 600 K).[142] The positive sign of the Seebeck coefficient is indicative of dominant *p*-type character, which is typical for Cu chalcogenides, in accord with the postulated, common Cu defects. One such example is Cu_2S, in which Zhao et al. found extrinsic semiconducting behavior from 400 K – 650 K, which was a result of Cu deficiencies.[92] The latter Seebeck values are in the desired range for thermoelectric materials, whereas *p*-type materials with S < +50 μV K^{-1} need further enhancements.

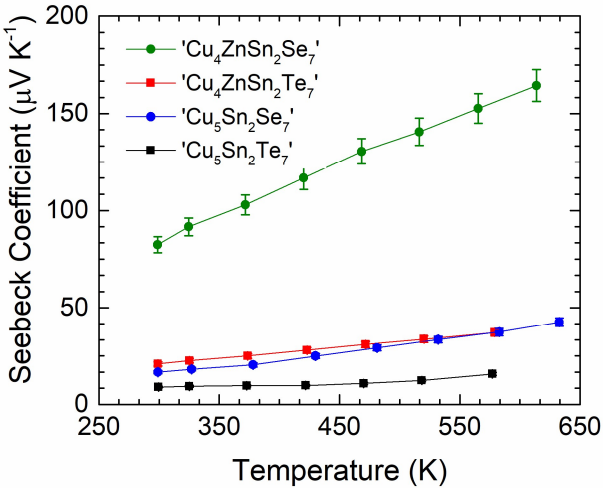

Figure 3.5. Temperature dependence of the Seebeck coefficient of 'Cu_5SnQ_7' and '$Cu_4ZnSn_2Q_7$' with 5% error bars.

At 300 K, we found a Seebeck coefficient of +9 μV K^{-1} for $Cu_5Sn_2Te_7$, in qualitative agreement with the earlier published value of +6 μV K^{-1}.[116] With the inclusion of Zn, the Seebeck coefficient experienced an over two-fold improvement at 300 K, from +9 μV K^{-1} ($Cu_5Sn_2Te_7$) to +21 μV K^{-1} ($Cu_4ZnSn_2Te_7$). At 575 K, a maximum of +37 μV K^{-1} was obtained for $Cu_4ZnSn_2Te_7$. Even with the inclusion of Zn, the thermopower values are still significantly lower than those of $Cu_2CdSnTe_4$ (S = +60 μV K^{-1} at 600 K)[143] and $CuInTe_2$ (S = +250 μV K^{-1} at 600 K).[48]

The increase of the Seebeck coefficient can be attributed to the decrease in carrier concentration with the introduction of Zn, as the carrier concentration is almost inversely proportional to the thermopower.[144] The Seebeck coefficient for degenerate semiconductors can be expressed via $S = \frac{8\pi^2 k_B^2}{3eh^2} m^* \left(\frac{\pi}{3n}\right)^{2/3}$, where k_B is the Boltzmann constant, e is the charge of an electron, m^* is the average effective mass, and T is the temperature. Boltzmann transport calculations were carried out on $Cu_4ZnSn_2Te_7$, which revealed Seebeck coefficients in excess of +300 μV K^{-1} in the vicinity of the Fermi level (Fig. 3.6). There is thus a possibility that such high

values could be experimentally obtained, if for example the apparent Cu atom defects could be minimized, or more Zn could be introduced.

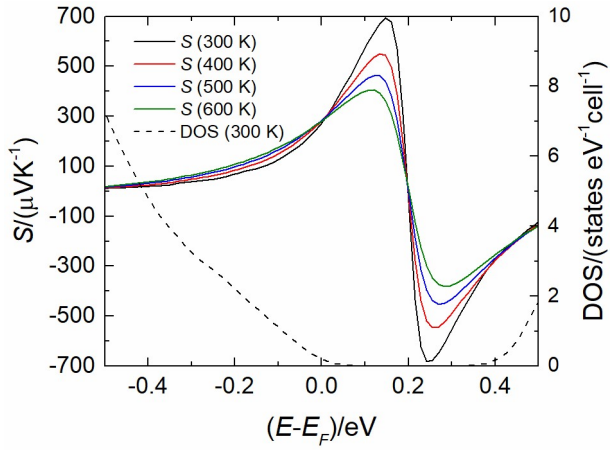

Figure 3.6. Calculated Seebeck coefficient and density of states relative to the Fermi energy for $Cu_4ZnSn_2Te_7$.

An overall, desired decrease in the thermal conductivity was also observed with the introduction of Zn for both the selenide and the telluride (Fig. 3.8). The reduction in the thermal conductivity is a direct consequence from decreasing the electrical conductivity. The thermal conductivity is a summation of two components: electrical (κ_{el}) and lattice (κ_{latt}) (Fig. A-3). The electrical component of the thermal conductivity can be derived using the Wiedemann-Franz law, $\kappa_{el} = L_0\ \sigma\ T$ (where L_0 is the Lorenz number). Due to all samples investigated here displaying extrinsic semiconducting-behavior, the Lorenz number was estimated by using the equation $L = \left(1.5 + \exp\left[\frac{-|S|}{116\ \mu V\ K^{-1}}\right]\right) 10^{-8}\ V^2\ K^{-2}$.[29] The lattice component can then be estimated by subtracting the electrical component from the total thermal conductivity. The κ_{latt} value obtained for $Cu_5Sn_2Se_7$ is 0.41 W $m^{-1}K^{-1}$, and with the addition of Zn, κ_{latt} increased to 2.88 W $m^{-1}K^{-1}$. The κ_{latt} value observed for $Cu_5Sn_2Te_7$ is 3.58 W $m^{-1}K^{-1}$, and with the addition of Zn, κ_{latt} decreased to 2.46 W $m^{-1}K^{-1}$.

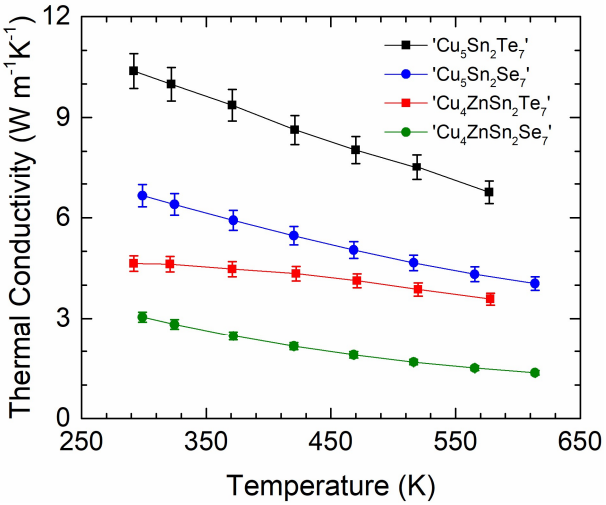

Figure 3.7. Temperature dependence of the thermal conductivity of '$Cu_5Sn\mathit{Q}_7$' and '$Cu_4ZnSn_2\mathit{Q}_7$' with 5% error bars.

The thermal conductivity values obtained for $Cu_5Sn_2Se_7$ are 6.7 W $m^{-1}K^{-1}$ – 4.0 W $m^{-1}K^{-1}$ from 300 K – 630 K (which qualitatively match Fan et al. with values of 5.3 W $m^{-1}K^{-1}$ – 3.5 W $m^{-1}K^{-1}$ within the same temperature range[141]). In accord with its lower electrical conductivity, $Cu_4ZnSn_2Se_7$ had lower thermal conductivity values of 3.0 W $m^{-1}K^{-1}$ – 1.4 W $m^{-1}K^{-1}$. Again, these values are quite comparable to $Cu_2ZnSnSe_4$ (κ = 1.9 W $m^{-1}K^{-1}$ – 1.1 W $m^{-1}K^{-1}$),[70] but higher than those of Cu_2SnSe_3 (κ = 1.5 W $m^{-1}K^{-1}$ – 0.7 W $m^{-1}K^{-1}$ between 300 K and 600 K).[142] The thermal conductivity values for $Cu_4ZnSn_2Se_7$ are somewhat on the high side, as many of the state of the art thermoelectric materials and Cu chalcogenides have κ values below 1 W $m^{-1}K^{-1}$.[92,145,146]

The telluride $Cu_5Sn_2Te_7$ also displayed thermal conductivity values higher than that of the sample containing Zn (κ = 10 W $m^{-1}K^{-1}$ – 6.8 W $m^{-1}K^{-1}$ versus 4.6 W $m^{-1}K^{-1}$ – 3.6 W $m^{-1}K^{-1}$, respectively, in the range of 300 K – 575 K). The room temperature thermal conductivity result for $Cu_5Sn_2Te_7$ is in reasonable agreement with Adhikary et al. (15 W $m^{-1}K^{-1}$).[116] The thermal conductivity values of $Cu_4ZnSn_2Te_7$ are comparable to $Cu_2CdSnTe_4$ (5.0 W $m^{-1}K^{-1}$ – 2.0 W $m^{-1}K^{-1}$)[143] and $CuInTe_2$ (6.0 W $m^{-1}K^{-1}$ – 2.5 W $m^{-1}K^{-1}$)[48] within the same temperature range. Although substantial improvements were made with the addition of Zn, the thermal conductivity values are

still too high for a thermoelectric material. We obtained lattice thermal conductivity values of 2.9 W $m^{-1}K^{-1}$ for $Cu_4ZnSn_2Se_7$ and 2.5 W $m^{-1}K^{-1}$ for $Cu_4ZnSn_2Te_7$ at room temperature.

The figure of merit curve of $Cu_5Sn_2Se_7$ nicely resembles the one calculated in 2016.[115] The figure of merit doubled for the Zn containing selenide, from 0.10 to 0.20 at 630 K (Fig. 3.8), and is higher than that of $Cu_2ZnSnSe_4$ (maximum zT of 0.16 at 630 K),[70] but significantly lower than Cu_2SnSe_3, which attained a maximum zT of 0.95 at 800 K.[142] This could be attributed to Cu_2SnSe_3 having a much larger Seebeck coefficient as well as lower thermal conductivity values.

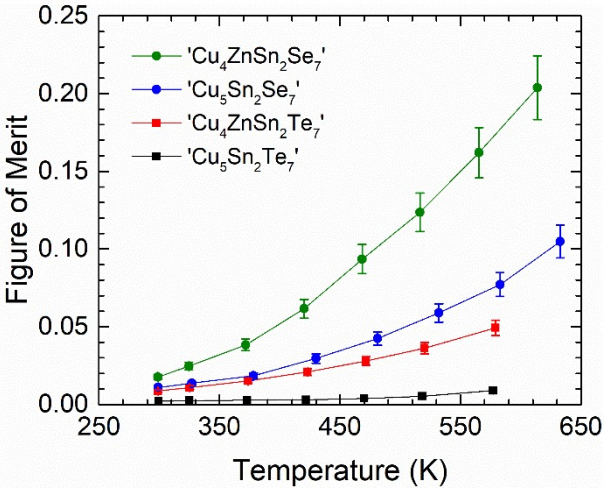

Figure. 3.8. Temperature dependence of the figure of merit of 'Cu_5SnQ_7' and '$Cu_4ZnSn_2Q_7$' with 10% error bars.

The quaternary telluride experienced a five-fold improvement in the figure of merit after incorporation of Zn, with a maximum of 0.05 for $Cu_4ZnSn_2Te_7$ at 575 K, whereas the corresponding zT for $Cu_5Sn_2Te_7$ was 0.009. For comparison, the maximum figure of merit value reported for $Cu_2CdSnTe_4$ was 0.12 at 510 K,[143] and 0.60 at 850 K for $CuInTe_2$.[48]

3.4 Conclusion

By doping both the selenide and telluride materials with Zn, the carrier concentration decreased, resulting in an overall decrease in the electrical conductivity, which had values that are comparable to some of the stannites and kesterites. Although substantial improvements were made, especially in case of the less toxic selenide, high *zT* values (closer to unity) were not possible due to low Seebeck coefficient and relatively high thermal conductivity values. It can be predicted based on our Boltzmann calculations that with the introduction of more Zn, higher thermopower values would be possible, but at the cost of a decrease in the electrical conductivity. Furthermore, due to the diamond-like structures, as well as the lack of heavy atoms for mass fluctuations, the lattice components of the thermal conductivity with 2.5 W $m^{-1}K^{-1}$ – 2.9 W $m^{-1}K^{-1}$ at 300 K need to be improved as well.

The tetrahedrites with their high *zT* values are considered to include some of the best tellurium-free copper chalcogenide TE materials in the mid temperature range. This is due to their complex frameworks and heavy atoms, which increases phonon scattering which reduces the thermal conductivity, while retaining a high electrical conductivity and thermopower values. One such example is $Cu_{11}MnSb_4S_{13}$, whose electrical conductivity and Seebeck coefficient were comparable to those of $Cu_4ZnSn_2Se_7$ (σ = 200 $\Omega^{-1}cm^{-1}$, S = 125 μV K^{-1} at 575 K), however the thermal conductivity was very low (κ = 0.30 W $m^{-1}K^{-1}$ at 575 K), which culminated in a high *zT* of 1.1 at 575 K.[146] Future work on the materials presented here could include attempts in which mass fluctuations are introduced (e.g. alloying Ag on Cu site or Cd on Zn), or nanostructuring in order to further reduce the thermal conductivity of these compounds.

CHAPTER 4:

Thermoelectric Properties of Hot-Pressed $Ba_3Cu_{14-\delta}Te_{12}$

This chapter is reproduced in part with permission from Inorganic Chemistry:
Cheryl Sturm, Natalie Boccalon, Abdeljalil Assoud, Tianze Zou, Jan B. Kycia and Holger Kleinke, *Inorganic Chemistry* (DOI: 10.1021/acs.inorgchem.1c00925).

4.1 Introduction

As previously mentioned in *Section 1.4.2,* our group has taken an interest in barium copper chalcogenides such as $Ba_{6.76}Cu_{2.42}Te_{14}$,[76] $Ba_2Cu_{4-x}Se_yTe_{5-y}$,[77] $BaCuSiTe_3$,[147] and $Ba_3Cu_{16-x}Se_{11-y}Te_y$[79,80] due to favorable thermoelectric properties. These materials exhibit recognizable copper chalcogenide attributes, such as Cu tetrahedral frameworks and *p*-type semiconductivity within a moderate temperature range (300 K – 600 K), with zT values up to 0.9.[80]

Previously our group published the crystal structure of $Ba_3Cu_{14-\delta}Te_{12}$, as well as the thermoelectric properties of cold-pressed pellets.[117] The crystal structure of $Ba_3Cu_{14-\delta}Te_{12}$ (Fig. 4.1) is complex, with a three-dimensionally extended network of Cu-Te polyhedra. The Cu atoms are either in a distorted tetrahedron of four Te atoms, or in a triangular coordination with three Te atoms. Each Ba atom is surrounded by nine Te atoms, forming a distorted mono-capped square antiprism. The structure also contains Te_2^{2-} pairs, which yields an electron precise material when $\delta = 0$: $(Ba^{2+})_3(Cu^{+})_{14}(Te_2^{2-})_2(Te^{2-})_8$.

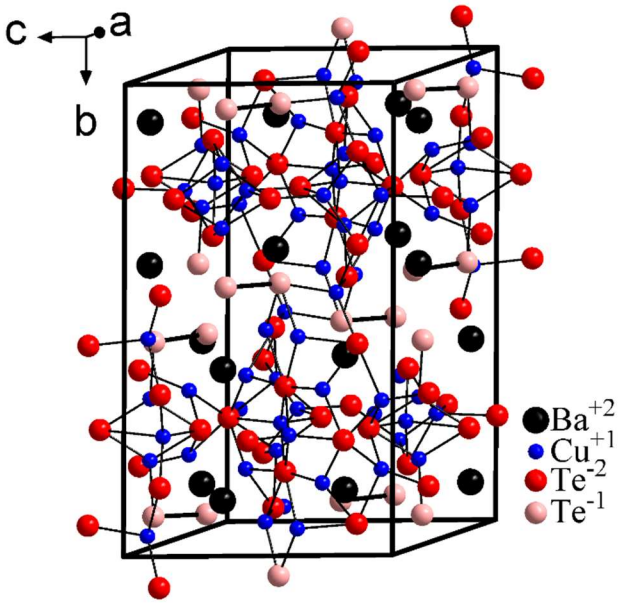

Figure 4.1. Crystal structure of $Ba_3Cu_{14-\delta}Te_{12}$, highlighting the coordination sphere of copper.

Due to the complex nature of the crystal structure, the thermal conductivity was reported to be a low 1.1 W $m^{-1}K^{-1}$ at 300 K, which is already as low as some of the best performing copper chalcogenide TE materials.[62] The Seebeck coefficient values obtained ranged from +38 μV K^{-1} to +100 μV K^{-1} from 300 K to 600 K, and in general did not have a clear trend corresponding to the value of δ(Cu deficiency), which may have been a consequence of the uncertainties caused by the cold-pressing procedure. The electrical conductivity values ranged from 150 $\Omega^{-1}cm^{-1}$ to 1000 $\Omega^{-1}cm^{-1}$ within the low temperature region of 180 K to 300 K. Again, there was no general trend correlating the electrical conductivity to the value of δ.[117]

This chapter aims to improve upon previously published data on varying the Cu deficiencies of hot-pressed $Ba_3Cu_{14-\delta}Te_{12}$. The stability with regards to copper ion migration was also explored, as well as attempts at enhancing the thermoelectric properties through alloying with Ag ($Ba_3Cu_{14-\delta-x}Ag_xTe_{12}$).

4.2 Sample Synthesis and Consolidation Parameters

All preparatory work to synthesize all compounds was performed inside an argon-filled glove box, starting with stoichiometric amounts of Ba pieces (99.7%, Strem), Cu powder (99.5%, Alfa Aesar), Te broken ingots (99.999%, Strem), and Ag powder (99.95%, Alfa Aesar).

All compounds were synthesized by utilizing the traditional solid-state tube method, in which the starting reagents were loaded into a fused silica tube, sealed under a dynamic vacuum of 2×10^{-3} mbar, and placed into high temperature muffle furnaces. The samples were then heated at 773 K for 12 hours, at 1073 K for two hours, then annealed at 873 K for two weeks, and subsequently air quenched to room temperature.

Thermoelectric properties were determined after hot pressing powders under an atmosphere of argon with an Oxy-Gon FR-210-30T-ASA-160-EVC hot-press furnace system, in a hardened graphite die with an inner diameter of 12.7 mm. The densification was done at 600 K under 46 MPa for three hours with a pressure free cool down, which resulted in > 95% of the theoretical density, as determined via the Archimedes method. The resulting pellets had a diameter of 12.7 mm and a height of 2 mm.

4.3 Results and Discussion

4.3.1 Characterization of $Ba_3Cu_{14-\delta}Te_{12}$ and $Ba_3Cu_{14-\delta-x}Ag_xTe_{12}$

Powder X-ray diffraction was used to determine the phase purity of all synthesized samples. All samples were found to be phase pure with no unwanted side products detected (Figs. 4.2 and 4.3). The experimentally obtained powder patterns for all materials were indexed to the previously published powder patterns of $Ba_3Cu_{13.65}Te_{12}$ (ICSD Coll. Code 194592). All compounds studied crystallize in the space group $P2_1/m$.

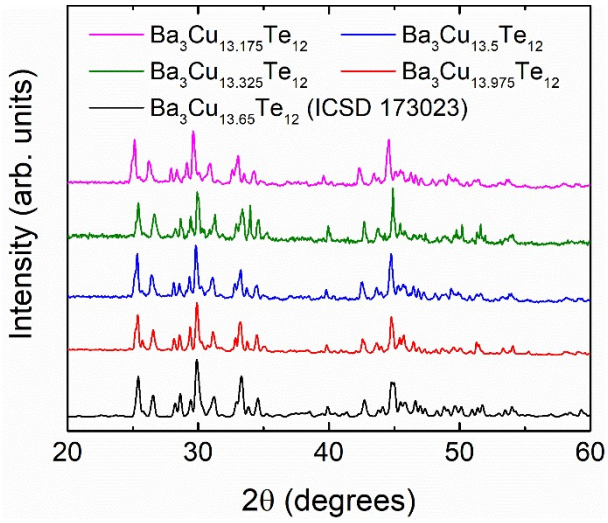

Figure 4.2. X-ray powder diffraction patterns of $Ba_3Cu_{14-\delta}Te_{12}$ (where δ = 0.825, 0.675, 0.50, 0.025).

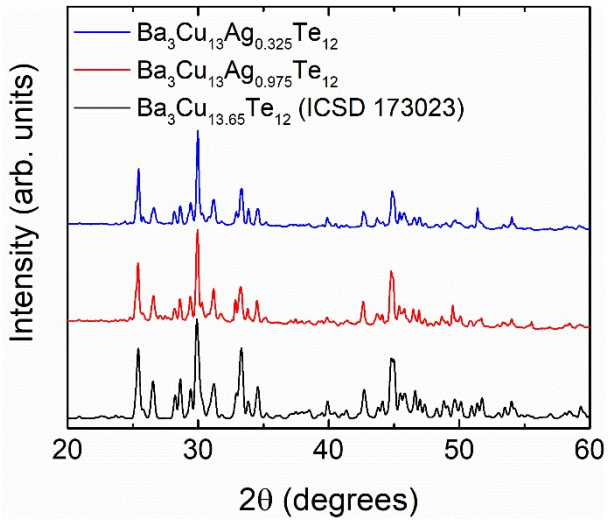

Figure 4.3. X-ray powder diffraction patterns of $Ba_3Cu_{13}Ag_{0.325}Te_{12}$ (blue) and $Ba_3Cu_{13}Ag_{0.925}Te_{12}$ (red).

An EDX (energy dispersive analysis of X-rays) study was performed on $Ba_3Cu_{14-\delta}Te_{12}$ (where δ = 0.025, 0.50, 0.675, 0.825) and $Ba_3Cu_{13}Ag_{0.975}Te_{12}$ and $Ba_3Cu_{13}Ag_{0.50}Te_{12}$. Experimental elemental ratios were determined by averaging over four to five analyzed spots over three crystals each, with the standard deviations determined by the population standard deviation method. The analysis showed all samples were homogenous, and the EDX mappings determined

that all three (or four) elements were distributed evenly throughout the scanned areas for the materials of the nominal compositions $Ba_3Cu_{13.975}Te_{12}$, $Ba_3Cu_{13.50}Te_{12}$, $Ba_3Cu_{13.325}Te_{12}$, $Ba_3Cu_{13.175}Te_{12}$, $Ba_3Cu_{13}Ag_{0.975}Te_{12}$, and $Ba_3Cu_{13}Ag_{0.50}Te_{12}$. For example, the averaged Ba : Cu : Te ratios for $Ba_3Cu_{13.975}Te_{12}$ were found to be 11.1(6) : 46.0(4) : 43(1) atomic-%, and the averaged Ba : Cu : Ag : Te ratios for $Ba_3Cu_{13}Ag_{0.975}Te_{12}$ were 11.1(2) : 44(2) : 2.3(7) : 43.0(7) at.-%. These ratios compare well to the expected values for $Ba_3Cu_{13.975}Te_{12}$ and for $Ba_3Cu_{13}Ag_{0.975}Te_{12}$ of 10.4 : 48.2 : 41.4 at.-% and 10.4 : 44.9 : 3.4 : 41.4 at.-%, respectively (Fig. A-5 and Tables A-4 and A-5). On the other hand, the differences in the Cu amounts appear to be within error, ranging from 45.9(5) at.-% - 46.9(5) at.-%. It is also noted that no binary chalcogenide or oxide side products (e.g., BaTe, Cu_2Te, Cu_2O, BaO_2 etc.) or impurities from the reaction vessels were detected in any of the scans.

Two single crystals were studied from the same sample with the nominal composition "$Ba_3Cu_{13.53}Te_{12}$" (two bars were cut from the same pellet). The first single crystal studied was retrieved from a bar which had property measurements performed up to 573 K, and has a refined formula of $Ba_3Cu_{13.54(1)}Te_{12}$. The second single crystal was retrieved from a bar which had property measurements performed up to 673 K, and has a refined formula of $Ba_3Cu_{13.53(1)}Te_{12}$. Finally, a third single crystal was retrieved from an ingot with a nominal composition of "$Ba_3Cu_{13}Ag_{0.5}Te_{12}$" and has a refined formula of $Ba_3Cu_{13.43(2)}Ag_{0.238(7)}Te_{12}$. Our results matched well with the previous data[117] with the exception of two additional peaks. These stood out in the difference Fourier map with the highest peak being 4.7 $e^-/Å^3$, while having distances > 2.5 Å to neighboring Te atoms like the other Cu sites. After refining these two peaks as Cu sites, namely as Cu7B and Cu8B because of their proximities to Cu7 and Cu8, $R1$ improved from 0.050 to 0.047 (observed reflections) in case of the 573 K data and from 0.062 to 0.061 in case of the 673 K data.

In order to elucidate the atomic positions of Ag, all Cu site occupancies were refined independently in case of the Ag containing crystal. All Cu positions with the exception of Cu2 had occupancies that were either 100% or less, and closely resembled the corresponding occupancies of the Ag-free samples. Cu2 exhibited an impossible occupancy of above 100% (namely 113%), and when refined with a mixed occupancy with Ag instead of as 100% Cu, an improvement in the *R*1 value from 0.030 to 0.028 (observed reflections) was noted. The average individual Cu-Te distances throughout $Ba_3Cu_{13.43}Ag_{0.24}Te_{12}$ were found to be 2.69 Å, compared to the average of the Cu2/Ag2-Te bond distances of 2.75 Å, which further supports the presence of the larger Ag atoms on the Cu2 site. In the Ag-free examples, the Cu2 site also stood out with larger Cu-Te distances, albeit not as noticeably, e.g. in $Ba_3Cu_{13.53}Te_{12}$ with Cu2-Te distances 2.73 Å, compared to an average of the other Cu-Te distances of 2.69 Å. Crystallographic details are summarized in Table 4.1, and Cu/Ag atom occupancies in Table 4.2. The crystallographic information files are available via the CCDC/FIZ Karlsruhe deposition service (CCDC 2071343, 2071344 and 2071345).

Table 4.1. Crystallographic data for $Ba_3Cu_{14-\delta-x}Ag_xTe_{12}$

Refined formula	‡$Ba_3Cu_{13.54(1)}Te_{12}$	‡‡$Ba_3Cu_{13.53(1)}Te_{12}$	$Ba_3Cu_{13.43(2)}Ag_{0.238(7)}Te_{12}$
Formula weight [g/mol]	2803.07	2802.76	2822.02
T of measurement [K]	300(2)	296(2)	300(2)
λ [Å]	0.71073	0.71073	0.71073
space group	$P2_1/m$	$P2_1/m$	$P2_1/m$
a [Å]	11.9572(5)	11.9470(6)	11.9737(2)
b [Å]	21.2408(10)	21.2340(11)	21.2654(4)
c [Å]	11.9985(6)	11.9968(6)	12.0175(2)
β [deg]	117.0112(2)	117.0553(14)	116.9770(5)
V [Å^3]	2715.0(2)	2710.3(2)	2727.00(8)
Z	4	4	4
μ [mm^{-1}]	27.252	27.294	27.217
ρ_{calcd} [g cm^{-3}]	6.858	6.869	6.874
$R(F_o^2)^a/R_w(F_o^2)^b$	0.047/0.086	0.061/0.113	0.028/0.059

‡Crystal taken from sample that was tested up to 573 K

‡‡Crystal taken from sample that was tested up to 673 K
[a] $R(F_o) = \Sigma||F_o| - |F_c||/\Sigma|F_o|$, [b] $R_w(F_o^2) = [\Sigma[w(F_o^2 - F_c^2)^2]/\Sigma[w(F_o^2)^2]]^{1/2}$

Table 4.2. Cu/Ag sites, coordinates and occupancy factors of $Ba_3Cu_{14-\delta-x}Ag_xTe_{12}$

Atom	Site	*x*	*y*	*z*	occ.[a]	occ.[b]	occ.[c]
Cu1	4f	0.03846(19)	0.65111(19)	0.27480(19)	0.848(6)	0.852(9)	0.883(4)
Cu2/Ag2	4f	0.06566(17)	0.67639(11)	0.06454(17)	1/0	1/0	0.762(7)/0.238(7)
Cu3	4f	0.14312(15)	0.54651(9)	0.40602(16)	1	1	1
Cu4	4f	0.16363(14)	0.18151(8)	0.70243(15)	1	1	1
Cu5	4f	0.1773(4)	0.0438(2)	0.2787(4)	0.412(6)	0.393(9)	0.401(3)
Cu6	4f	0.25638(17)	0.68415(7)	0.00032(17)	1	1	1
Cu7A	4f	0.33711(19)	0.17494(11)	0.3139(2)	0.886(5)	0.892(8)	0.888(2)
Cu7B	4f	0.3122(15)	0.1518(9)	0.3657(18)	0.114(5)	0.108(8)	0.112(2)
Cu8A	4f	0.5419(2)	0.15073(10)	0.27751(18)	0.927(6)	0.927(11)	0.935(3)
Cu8B	4f	0.600(3)	0.1665(13)	0.274(2)	0.073(6)	0.073(11)	0.065(3)
Cu9	4f	0.54714(15)	0.18196(9)	0.06756(15)	1	1	1
Cu10	4f	0.65505(14)	0.04696(9)	0.39317(16)	1	1	1
Cu11	4f	0.97047(19)	0.04212(11)	0.0780(2)	0.784(6)	0.773(9)	0.835(4)
Cu12	2e	0.1735(2)	¼	0.3296(2)	0.968(9)	1	1
Cu13	2e	0.3269(2)	¼	0.6734(2)	1	1	1
Cu14	2e	0.3332(2)	¼	0.9057(2)	1	1	1
Cu15	2e	0.5461(2)	¼	0.8728(2)	1	1	1
Cu16	2e	0.5758(2)	¼	0.4211(3)	0.942(9)	0.933(13)	0.936(5)
Cu17	2e	0.9273(2)	¼	0.5863(2)	0.940(9)	0.946(13)	1
Cu18	2e	0.9457(2)	¼	0.1280(3)	1	1	1
Cu19	2e	0.1631(12)	¼	0.1030(14)	0.151(8)	0.169(8)	0.157(5)

[a]Occupancy factors of $Ba_3Cu_{13.53}Te_{12}$ heated up to 573 K
[b]Occupancy factors of $Ba_3Cu_{13.53}Te_{12}$ heated up to 673 K
[c]Occupancy factors of $Ba_3Cu_{13.43}Ag_{0.24}Te_{12}$

Density Functional Theory (DFT) calculations were performed via the WIEN2k package, utilizing the full potential linearized augmented plane wave method (LAPW). The PBE (Perdew, Burke and Ernzerhof) functional was initially adopted for the generalized gradient approximation

(GGA),[148] followed by the modified Becke-Johnson (mBJ) exchange potential correction to obtain a more accurate band gap.[149] To model $Ba_3Cu_{14}Te_{12}$, we took the crystallographic data from $Ba_3Cu_{13.54(1)}Te_{12}$, treated all Cu sites with occupancies above 75% as fully occupied, and removed all Cu sites with occupancies below 20%. This leaves Cu5 on 4f with its refined occupancy of 41%. We removed two of its four sites per unit cell in two different ways, one resulting in space group $P2_1$, and one in space group *Pm*. This yielded Cu5 as 50% occupied in two different orders, and overall a formula of $Ba_3Cu_{14}Te_{12}$ in both cases. Due to the large unit cells, both calculations were performed on a grid of 5 × 2 × 5 *k* points along the respective vectors of the reciprocal lattice, until energy convergence was achieved within 0.0001 Ry.

For the band structure calculations with the WIEN2k package, we used the same path through the first Brillouin zone as in the LMTO[150] calculation published earlier.[117] In addition to using a higher level theory, we now also considered another ordering of the Cu sites, leading to the space group $P2_1$ (Fig. 4.4a). The shapes of the bands in $P2_1$ and *Pm* (Fig. 4.4b) around the Fermi level (E_F) are very comparable, with the exception of the different degeneracies in the conduction band comprised of antibonding *p* states of the Te_2^{2-} dumbbells at the Y point.

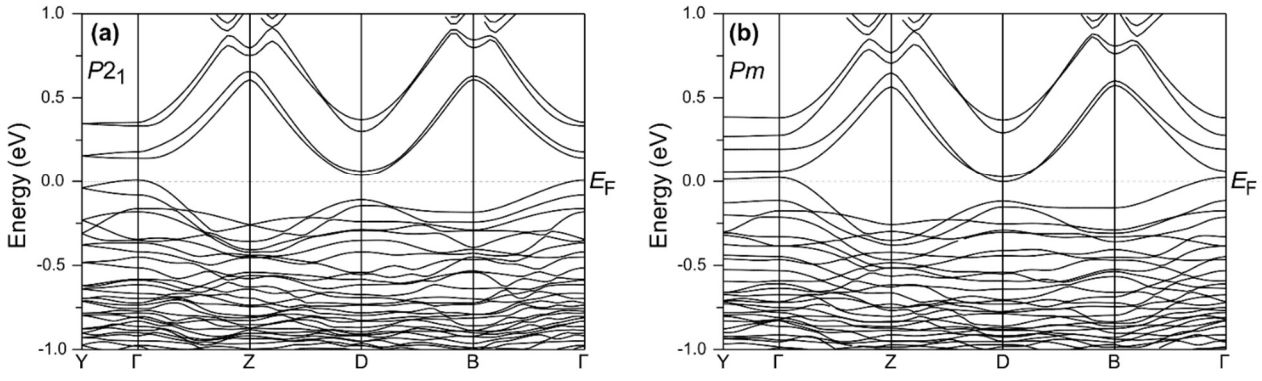

Figure 4.4. Band structures of the $Ba_3Cu_{14}Te_{12}$ models in (a) space group $P2_1$ and (b) in space group *Pm*, with the Fermi level E_F placed at 0 eV.

Comparing the WIEN2k calculation with the LMTO calculation, we noticed almost identical band shapes, but lower energies of the lowest lying conduction bands at D in case of the WIEN2k calculation. In this case, the conduction band at D actually overlaps energetically with the valence band at Γ, which was neither the case in the LMTO calculation of the *Pm* model nor in the WIEN2k calculation of the $P2_1$ model. In conclusion, two of the three model calculations were indicative of narrow gap semiconducting behavior, and one of semimetallic behavior. As both different models use different but complete ordering, the real material should exhibit intermediate properties, given its disordered nature.

The thermal behavior of $Ba_3Cu_{13.5}Te_{12}$ was analyzed via differential scanning calorimetry (DSC) using a TA Instruments DSC Q2000 under a flow of nitrogen from room temperature to 673 K. Endothermic phase transitions were detected at 520 K and at 645 K (Fig. A-6). Based on the single crystal refinements above-mentioned, these were reversible phase transitions.

4.3.2 Thermoelectric Properties of $Ba_3Cu_{14-\delta}Te_{12}$

The thermoelectric properties of $Ba_3Cu_{14-\delta}Te_{12}$ were studied between 300 K and at least 575 K. The temperature dependence of the electrical conductivity is shown in Fig. 4.5a. Although previously published data displayed no clear connection between the Cu deficiency and the electrical conductivity, it was now clearly exhibited. This more consistent behavior may be attributed to the hot-pressed samples being denser, as the previously reported cold-pressed pellets only had densities of 70% - 80% of the theoretical maximum, whereas our new pellets had densities > 95%. The sample that was the most Cu deficient (nominal δ = 0.825) exhibited the highest electrical conductivity values, while the sample that was the least Cu deficient (δ = 0.025) had the lowest values. As the nominal Cu concentration decreased (increasing δ), the *p*-type carrier

concentration increased, due to fewer valence electrons. The trend of the electrical conductivity can be directly linked to the carrier concentration, as defined by the equation $\sigma = n \mu e$, where n is the carrier concentration, μ is the carrier mobility, and e is the charge of an electron. The Hall data obtained on the samples with $\delta = 0.675$ and $\delta = 0.825$ supported these arguments, with $n = 2.9 \times 10^{21}$ cm^{-3} for the more Cu-deficient and $n = 7.2 \times 10^{20}$ cm^{-3} for the less Cu-deficient sample. The sample with the higher carrier concentration exhibited the lower mobility ($\mu = 1.9$ cm^{2}V^{-1}s^{-1} vs. 3.2 cm^{2}V^{-1}s^{-1}), due to increased carrier-carrier scattering.

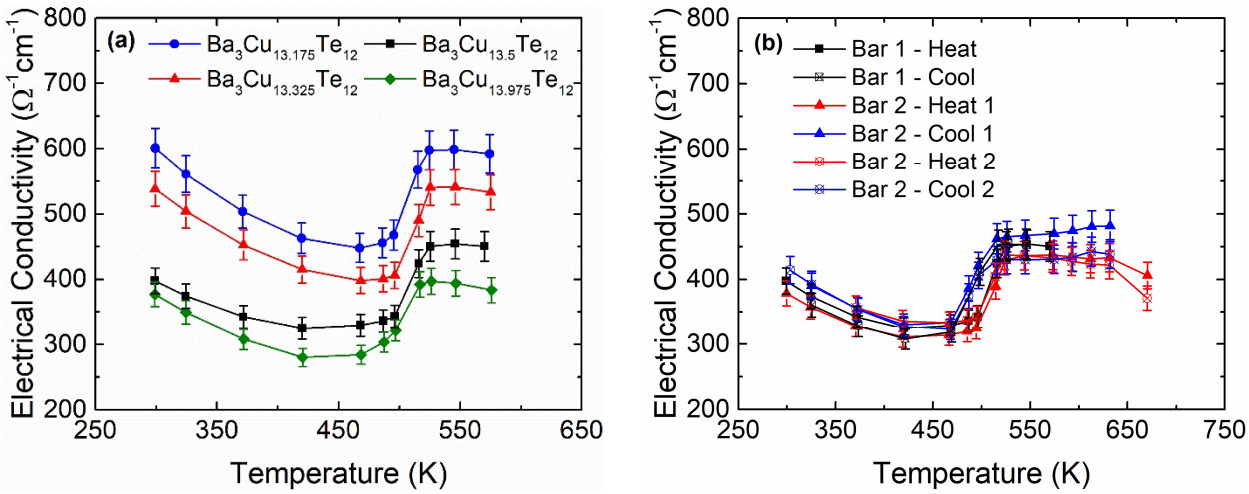

Figure 4.5. Temperature dependence of the electrical conductivity of (a) $Ba_3Cu_{14-\delta}Te_{12}$ and (b) $Ba_3Cu_{13.5}Te_{12}$ (comparisons of two bars cut from the same pellet) with 5% error bars.

All four materials exhibit a negative temperature dependence between 300 K - 470 K, which is typical for degenerate semiconductors, due to increasing scattering with increasing temperature and therefore decreasing mobility of charge carriers. From 470 K to 540 K, a positive temperature dependence was observed, likely due to thermally activated intrinsic carriers, and finally a slight negative temperature dependence was exhibited above that, which is attributed to the phase transition around 520 K as detected by the DSC experiment.

The $Ba_3Cu_{13.175}Te_{12}$ material exhibited the highest electrical conductivity of 600 $\Omega^{-1}cm^{-1}$ at 300 K with the lowest σ observed at 470 K (450 $\Omega^{-1}cm^{-1}$), which is expected due to it being the most deficient in Cu. $Ba_3Cu_{13.325}Te_{12}$ had the next highest electrical conductivity of 540 $\Omega^{-1}cm^{-1}$ at 300 K, with the lowest value being σ = 400 $\Omega^{-1}cm^{-1}$ at 470 K, followed by $Ba_3Cu_{13.5}Te_{12}$ with σ = 400 $\Omega^{-1}cm^{-1}$ at 300 K and a minimum of σ = 320 $\Omega^{-1}cm^{-1}$ at 420 K. The least conducting material, $Ba_3Cu_{13.975}Te_{12}$, exhibited electrical conductivity values of σ = 375 $\Omega^{-1}cm^{-1}$ at 300 K and 280 $\Omega^{-1}cm^{-1}$ at 420 K.

While the expected general trend was observed, the two most conducting samples ($Ba_3Cu_{13.175}Te_{12}$ and $Ba_3Cu_{13.325}Te_{12}$) had electrical conductivity values that were in part within the experimental error of each other. This could be attributed to the small difference in the nominal compositions. The two least conducting materials ($Ba_3Cu_{13.5}Te_{12}$ and $Ba_3Cu_{13.975}Te_{12}$) also had electrical conductivity values partly within error of each other, despite a larger difference in composition. This could be explained by $Ba_3Cu_{13.975}Te_{12}$ being more Cu deficient than the formula implies, as seen in the respective EDAX analysis and implied by the relatively high carrier concentration.

Generally the electrical conductivity values obtained at 300 K were higher than what was previously published (δ = 0.025: σ = 250 $\Omega^{-1}cm^{-1}$; δ = 0.500: σ = 375 $\Omega^{-1}cm^{-1}$; δ = 0.675: σ = 475 $\Omega^{-1}cm^{-1}$; δ = 0.825: σ = 675 $\Omega^{-1}cm^{-1}$).[117] The increase in electrical conductivity is attributed to samples being hot pressed, rather than cold pressed, in which higher density values were obtained (75% - 80% of the theoretical density versus our > 95%). The electrical conductivity values obtained are comparable to those of high performance copper chalcogenides. More specifically barium copper chalcogenides have also been observed to have electrical conductivity values between 100 $\Omega^{-1}cm^{-1}$ and 700 $\Omega^{-1}cm^{-1}$. Our electrical conductivity values were comparable to

those of Cu_2Se (σ = 750 $\Omega^{-1}cm^{-1}$ to 250 $\Omega^{-1}cm^{-1}$ from 300 K to 900 K),[56] but higher than those of the polychalcogenide $BaCu_{5.9}SeTe_6$ (σ = 250 $\Omega^{-1}cm^{-1}$ to 150 $\Omega^{-1}cm^{-1}$ from 300 K to 575 K)[82] and the high performance tetrahedrite $Cu_{10.5}NiZn_{0.5}Sb_4S_{13}$ (σ = 130 $\Omega^{-1}cm^{-1}$ to 180 $\Omega^{-1}cm^{-1}$ from 300 K to 700 K).[151]

A comparison of the heating curve with the cooling curve of $Ba_3Cu_{13.5}Te_{12}$ was inconclusive, after noting that the data appear to differ by up to 30%, e.g. at 546 K, σ = 454 $\Omega^{-1}cm^{-1}$ was measured while heating and σ = 452 $\Omega^{-1}cm^{-1}$ while cooling, and at 323 K, 374 $\Omega^{-1}cm^{-1}$ and 361 $\Omega^{-1}cm^{-1}$, respectively. Thus, a second bar of $Ba_3Cu_{13.5}Te_{12}$ was cut from the same pellet and cycled twice up beyond the second phase transition at 645 K to 670 K (Fig. 4.5b) to further analyze the stability at higher temperatures. The results revealed an overall lack of reproducibility, with a noticeable jump above 600 K. At 631 K, we determined σ = 433 $\Omega^{-1}cm^{-1}$ while heating and then right after that, σ = 482 $\Omega^{-1}cm^{-1}$ while cooling, corresponding to an increase of 11%. This was at least in part an irreversible change, as the low temperature data differed by a similar amount, e.g. at 323 K we found 357 $\Omega^{-1}cm^{-1}$ and 390 $\Omega^{-1}cm^{-1}$, respectively. Interestingly, both the next heating and cooling cycles resulted in lower numbers, for example 422 $\Omega^{-1}cm^{-1}$ and 439 $\Omega^{-1}cm^{-1}$ at 631 K. To investigate whether this irreversible behavior could be due to a change in the positions of the Cu^+ ions, as observed in case of $Ba_3Cu_{16-x}Se_{11-y}Te_y$,[79] single crystal analyses were performed from both bars. The analyses showed no significant changes in the site occupancies of Cu and overall stoichiometry (Table 4.2), and therefore we concluded that other irreversible material changes must have occurred, most likely caused by a hysteresis in the second phase transition.

The temperature dependence of the Seebeck coefficient is displayed in Fig. 4.6a. All compounds initially experienced an increase in their thermopower as the temperature increases. This behavior is common for both extrinsic and degenerate semiconductors as well as semimetals.

The positive sign of the Seebeck coefficient is indicative of *p*-type conduction, and is typical for Cu chalcogenides due to Cu deficiencies. The materials with the nominal Cu deficiencies of δ = 0.500, 0.675, and 0.825 all had very similar thermopower values of 23 μV K^{-1} to 60 μV K^{-1} in the temperature range of 300 K to 570 K, while $Ba_3Cu_{13.975}Te_{12}$ exhibited slightly higher values of 28 μV K^{-1} to 62 μV K^{-1}. A noticeable negative temperature dependence was observed for all four compounds just above 500 K, which is the same temperature of the above discussed onset of the increase in the electrical conductivity. This can be attributed to an increase in the intrinsic carriers, that begin to have enough energy above 500 K to become thermally activated. This increase would then decrease the thermopower, as the carrier concentration is almost inversely proportional to the Seebeck coefficient for extrinsic semiconductors, which is given as $S = \frac{8\pi^2 k_B^2}{3eh^2} m^* \left(\frac{\pi}{3n}\right)^{2/3}$, where k_B is the Boltzmann constant, e is the charge of an electron, m^* is the effective mass, and T is the temperature. Beyond the phase transition at 520 K, the Seebeck values began to increase again.

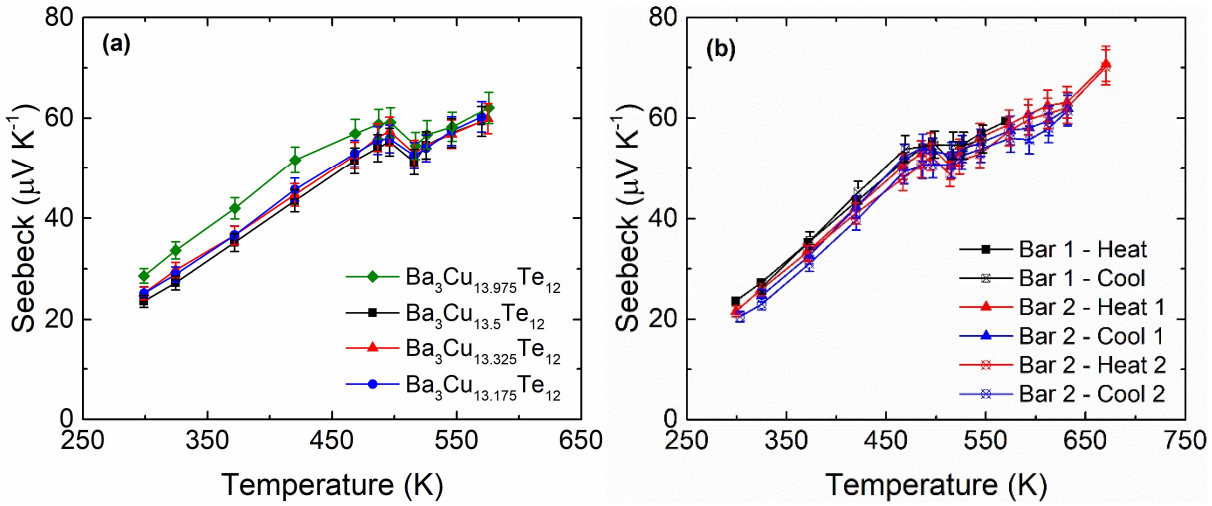

Figure 4.6. Temperature dependence of the Seebeck coefficient of (a) $Ba_3Cu_{14-\delta}Te_{12}$ and (b) $Ba_3Cu_{13.5}Te_{12}$ (comparisons of two bars cut from the same pellet) with 5% error bars.

Overall, these Seebeck values were consistently lower than those previously reported. Those earlier data displayed no apparent correlation between Cu concentration and thermopower within the temperature range of 300 K to 550 K (δ = 0.025: 49 μV K^{-1} to 110 μV K^{-1}; δ = 0.500: 49 μV K^{-1} to 110 μV K^{-1}; δ = 0.675: 35 μV K^{-1} to 70 μV K^{-1}; δ = 0.825: 52 μV K^{-1} to 100 μV K^{-1}).[117] Typically, high performance *p*-type thermoelectric materials exhibit thermopower values well in excess of 50 μV K^{-1}.[53] While the highest thermopower obtained here was 60 μV K^{-1} at 570 K, this value was still lower than that of most advanced *p*-type thermoelectric materials such as Cu_2Se (75 μV K^{-1} to 250 μV K^{-1} at 300 K to 900 K),[56] $BaCu_{5.9}SeTe_6$ (150 μV K^{-1} to 225 μV K^{-1} at 300 K to 575 K),[152] and $Cu_{10.5}NiZn_{0.5}Sb_4S_{13}$ (150 μV K^{-1} to 200 μV K^{-1} at 300 K to 700 K).[151] Thus, further attempts to enhance the Seebeck coefficient of $Ba_3Cu_{14-\delta}Te_{12}$ are required for this material to become competitive.

The reproducibility of the Seebeck coefficient for the material $Ba_3Cu_{13.5}Te_{12}$ was also explored up to 670 K (Fig. 4.6b). The changes appeared to be insignificant, as for example the values ranged only from 31 μV K^{-1} to 33 μV K^{-1} at 373 K, and from 61 μV K^{-1} to 63 μV K^{-1} at 631 K during the two heating and two cooling cycles.

The thermal conductivity had a similar temperature dependence as the electrical conductivity (Fig. 4.7a). All samples displayed a negative temperature dependence from 300 K to 450 K, then had a positive temperature dependence for most of the rest of the range measured. The samples with the highest Cu deficiencies, thus the highest electrical conductivity, also had the highest thermal conductivity values (δ = 0.025: 0.97 W $m^{-1}K^{-1}$ - 0.84 W $m^{-1}K^{-1}$; δ = 0.500: 0.80 W $m^{-1}K^{-1}$ - 0.91 W $m^{-1}K^{-1}$; δ = 0.675: 0.81 W $m^{-1}K^{-1}$ - 0.91 W $m^{-1}K^{-1}$; δ = 0.825: 0.92 W $m^{-1}K^{-1}$ - 1.01 W $m^{-1}K^{-1}$).

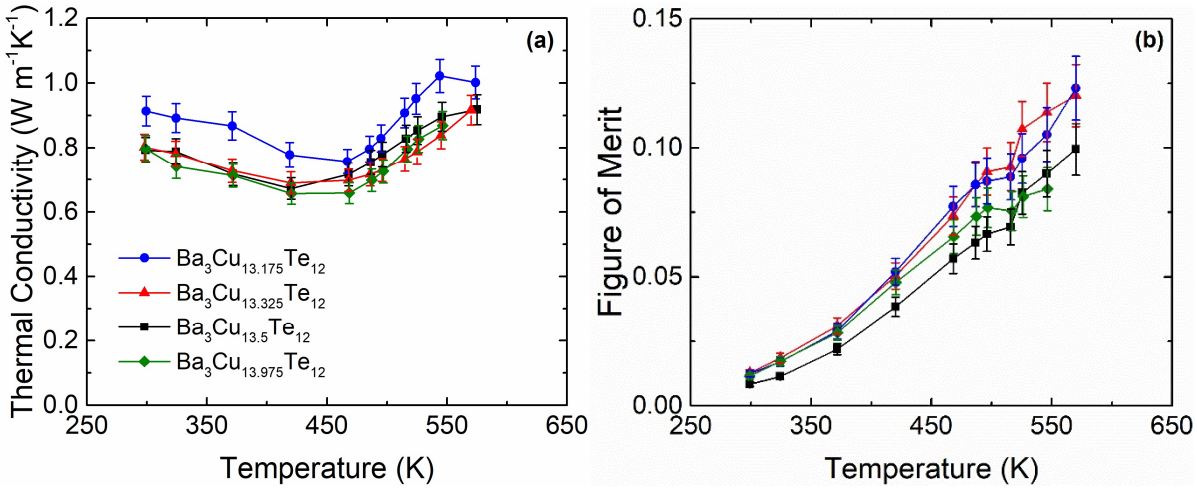

Figure 4.7. Temperature dependence of (a) the thermal conductivity with 5% error bars and (b) the figure of merit with 10% error bars of $Ba_3Cu_{14-\delta}Te_{12}$.

This trend can be explained by analyzing the electrical (κ_e) and lattice (κ_l) components, which when combined yield the total value of the thermal conductivity ($\kappa = \kappa_e + \kappa_l$). The electrical component is directly related to the electrical conductivity by the Wiedemann-Franz law, $\kappa_e = L\,\sigma\,T$, where L is the Lorenz number. The Lorenz number can be estimated via $L = 1.5 + exp\left[\frac{-|S|}{116}\right]$ (where L is in 10^{-8} V^2 K^{-2} and S is in μV K^{-1}).[29] The lattice component is then derived by subtracting the electrical component from the total thermal conductivity. Both the electrical and the lattice contributions were about equal in all cases (Fig. A-8).

Overall the thermal conductivity values obtained for all the materials studied were very low, e.g. mostly below 1 W $m^{-1}K^{-1}$. Additionally, the thermal conductivity values of $Ba_3Cu_{14-\delta}Te_{12}$ were on the order of those of high performance copper chalcogenides such as Cu_2Se (from 1.2 W $m^{-1}K^{-1}$ to 0.6 W $m^{-1}K^{-1}$ from 300 K to 900 K),[56] $BaCu_{5.9}SeTe_6$ (0.85 W $m^{-1}K^{-1}$ to 0.5 W $m^{-1}K^{-1}$ from 300 K to 575 K),[82] and $Cu_{10.5}Ni_{0.5}Sb_4S_{13}$ (0.5 W $m^{-1}K^{-1}$ to 0.55 W $m^{-1}K^{-1}$ from 300 K to 700 K).[151]

The lowest figure of merit values were obtained from the least Cu deficient samples ($Ba_3Cu_{13.975}Te_{12}$, zT values from 0.012 to 0.084) and the highest figure of merit from the most Cu deficient, most conducting samples ($Ba_3Cu_{13.175}Te_{12}$, from 0.012 to 0.123) between 300 K - 570 K (Fig. 4.7b). All of these values were significantly lower than those of the high performance copper chalcogenides such as Cu_2Se (zT = 1.2 at 900 K),[56] $BaCu_{5.9}SeTe_6$ (zT = 0.7 at 580 K),[82] and $Cu_{10.5}Ni_{0.5}Sb_4S_{13}$ (zT = 1.03 at 700 K),[151] largely because of the uncompetitive Seebeck values.

4.3.3 Thermoelectric Properties of $Ba_3Cu_{14-\delta-x}Ag_xTe_{12}$

A brief alloying study was initiated in an effort to potentially lower the thermal conductivity to obtain a higher figure of merit. The thermoelectric properties of the samples of nominal composition $Ba_3Cu_{13}Ag_{0.975}Te_{12}$ and $Ba_3Cu_{13}Ag_{0.325}Te_{12}$ were studied within the same temperature range as $Ba_3Cu_{14-\delta}Te_{12}$ (Fig. 4.8a). The electrical conductivity values increased by 20% when alloyed with silver for both compounds ($Ba_3Cu_{13}Ag_{0.975}Te_{12}$: from 480 $\Omega^{-1}cm^{-1}$ to 455 $\Omega^{-1}cm^{-1}$; $Ba_3Cu_{13}Ag_{0.325}Te_{12}$: from 660 $\Omega^{-1}cm^{-1}$ to 645 $\Omega^{-1}cm^{-1}$ between 300 K and 530 K. The thermopower remained largely unaffected after the incorporation of silver ($Ba_3Cu_{13}Ag_{0.975}Te_{12}$: from 23 $\mu V\ K^{-1}$ to 63 $\mu V\ K^{-1}$; $Ba_3Cu_{13}Ag_{0.325}Te_{12}$: from 25 $\mu V\ K^{-1}$ to 60 $\mu V\ K^{-1}$) in the same temperature range (Fig. 4.8b).

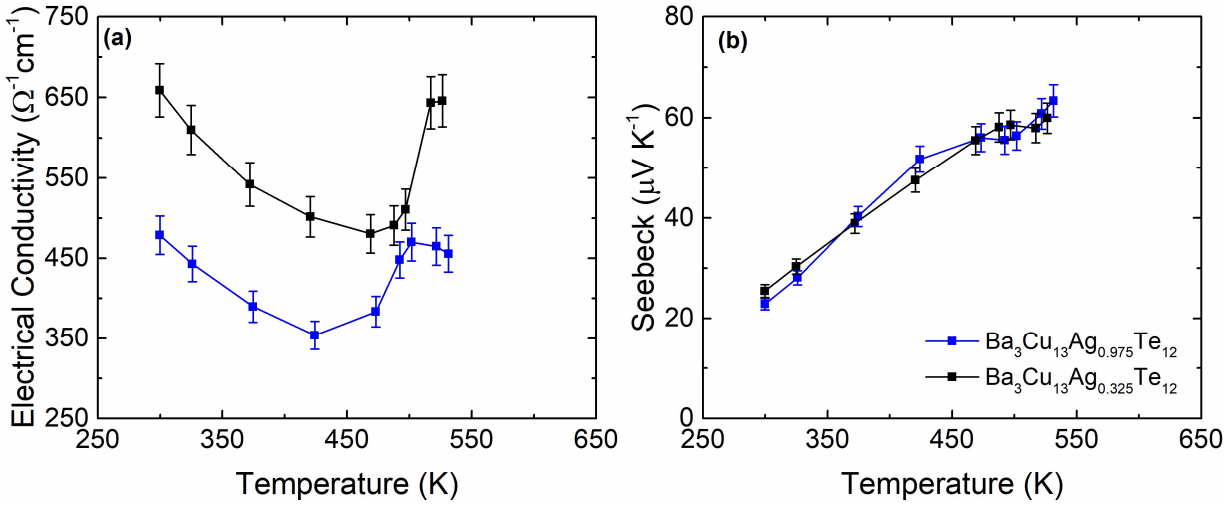

Figure 4.8. Temperature dependence of (a) the electrical conductivity and (b) the Seebeck coefficient both with 5% error bars of $Ba_3Cu_{13}Ag_{0.975}Te_{12}$ and $Ba_3Cu_{13}Ag_{0.325}Te_{12}$.

The thermal conductivity values (Fig. 4.9a) were slightly increased ($Ba_3Cu_{13}Ag_{0.975}Te_{12}$: from 0.88 W m^{-1}K^{-1} to 0.86 W m^{-1}K^{-1}; $Ba_3Cu_{13}Ag_{0.325}Te_{12}$: from 0.94 W m^{-1}K^{-1} to 1.1 W m^{-1}K^{-1}), due to the increased electrical component of the thermal conductivity (Fig A-10). All of these parameters resulted in a figure of merit that was basically unchanged for both samples ($Ba_3Cu_{13}Ag_{0.975}Te_{12}$: zT_{max} = 0.11; $Ba_3Cu_{13}Ag_{0.325}Te_{12}$,: zT_{max} = 0.12), as displayed in Fig. 4.9b.

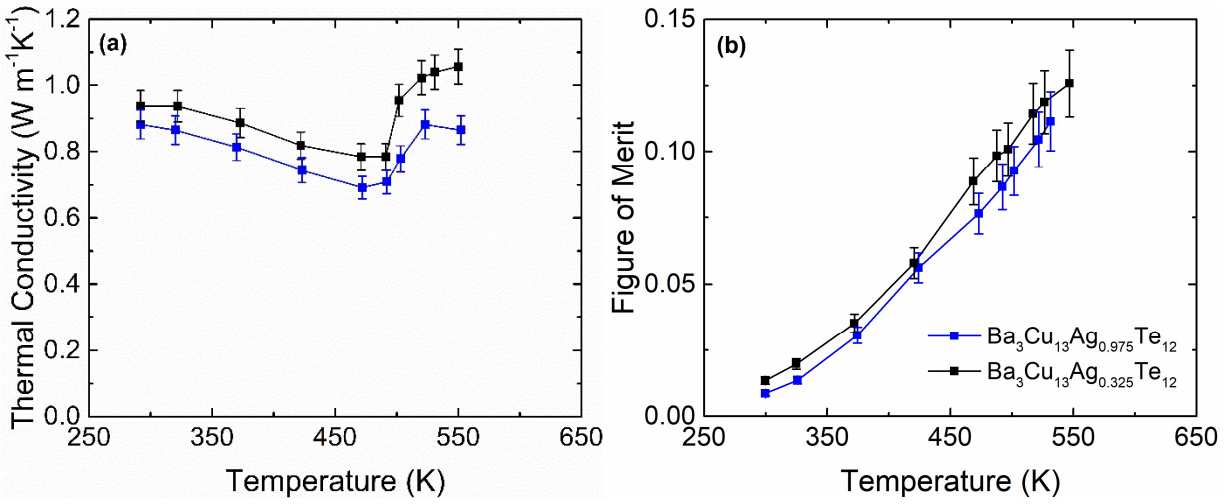

Figure 4.9. Temperature dependence of (a) the thermal conductivity with 5% error bars and (b) the figure of merit with 10% error bars of $Ba_3Cu_{13}Ag_{0.975}Te_{12}$ and $Ba_3Cu_{13}Ag_{0.325}Te_{12}$.

4.4 Conclusion

By decreasing the Cu concentration in $Ba_3Cu_{14-\delta}Te_{12}$, the electrical conductivity increased, resulting in values similar to those of high performance Cu chalcogenide thermoelectric materials. At the same time, the thermal conductivity remained competitive with values below 1 W $m^{-1}K^{-1}$. However, the Seebeck coefficient values were lower than those of high performance thermoelectric materials, and therefore efforts should be made in the future to increase the thermopower, if possible. The use of nanostructuring (such as the introduction of more grain boundaries) could increase the thermopower while retaining the electrical conductivity via the energy filtering approach.

Our single crystal studies on crystals selected from samples tested up to 573 K and 673 K showed no changes in the Cu site occupancies, which is indicative of the absence of irreversible changes in the crystal structure stemming from Cu ion migration. Our attempts to increase the Seebeck coefficient by alloying with Ag did not produce any significant changes. Although all samples presented here exhibited desirable electrical and thermal conductivity values, the Seebeck coefficients were low, which overall produced low figure of merit values, with the highest being $zT = 0.12$ at 570 K for $Ba_3Cu_{13.175}Te_{12}$.

CHAPTER 5:

Thermoelectric Properties of the Mixed Ion-Electron Conductor Ag_8SnS_6

This chapter is reproduced in part with permission from ACS Applied Energy Materials: Cheryl Sturm, Natalie Boccalon, Daniel C. Ramirez and Holger Kleinke, *ACS Applied Energy Materials*, in press.

5.1 Introduction

As stated in *Section 1.4.3.2*, due to the inherently low thermal conductivity and potential for superionic conductivity, there is increasing interest in the thermoelectric properties of Ag_8SnS_6. The Ag atoms become mobile after the phase transition from the low temperature orthorhombic phase (space group $Pna2_1$) to the high temperature cubic phase ($F\bar{4}3m$) at 420 K (Fig. 5.1).[96,100] Ag_8SnS_6 (bulk sample) was previously reported to exhibit a peak zT of 0.5 at 750 K.[100] Ag_8SnS_6 as a thin film produced a similar figure of merit of 0.55 at room temperature.[113] These previous studies suggest Ag_8SnS_6 could be a competitive thermoelectric material, however the stability and ionic mobility could pose potential problems.

The aim of this chapter is to report on the stability of Ag_8SnS_6. The thermoelectric properties were also studied and attempts were made to enhance the electrical conductivity with the addition of excess Ag atoms.

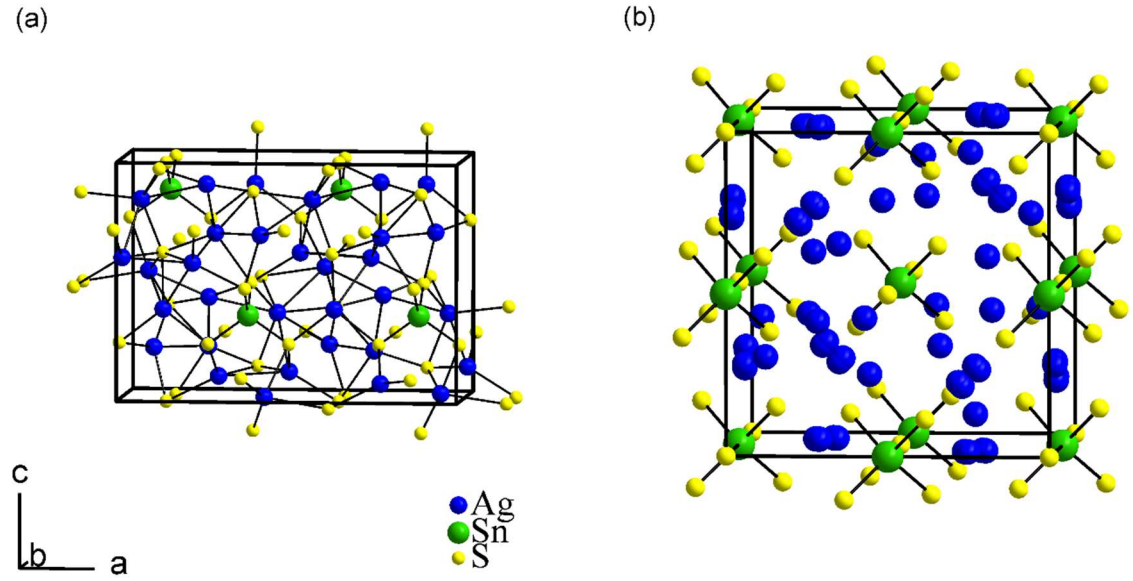

Figure 5.1. Crystal structures of Ag_8SnS_6 in the (a) orthorhombic low-temperature and (b) cubic high temperature modification.

5.2 Sample Synthesis and Consolidation Parameters

All preparatory work to synthesize the materials of nominal compositions Ag_8SnS_6 and '$Ag_{8.1}SnS_6$' was performed inside an argon-filled glove box, starting with stoichiometric amounts of Ag shots (99.9%, Alfa Aesar), Sn granules (99.9%, Alfa Aesar), and S flakes (99.999%, Alfa Aesar). The materials were synthesized using the traditional solid-state tube method. The starting reagents were loaded into fused silica tubes, sealed under a dynamic vacuum of 2×10^{-3} mbar and placed into high temperature muffle furnaces. The sealed ampoules were heated to 723 K at a ramp rate of 50 K per hour and annealed for four hours. The ampoules were then ramped to 1273 K at a rate of 50 K per hour and annealed for 48 hours and then finally air quenched to room temperature by opening the furnace to save time.

The resulting ingots retrieved from the ampoules were ground into a polycrystalline powder and hot pressed in a graphite hardened die at 573 K under 46 MPa for three hours with a pressure free cool down, which resulted in over 95% of the theoretical density, as determined via

the Archimedes method. No depositions of any elements were detected in the press. The resulting pellets had a diameter of 12.7 mm and a height of 1.8 mm.

The resulting pellet was then cut into a 2 x 2 x 2 mm^3 cube for specific heat capacity determination. The specific heat capacity was determined by a low temperature measurement that resulted in a room temperature value of 0.308 J $g^{-1}K^{-1}$, slowly approaching the Dulong-Petit limit of 0.319 J $g^{-1}K^{-1}$.

5.3 Results and Discussion

5.3.1 Characterization of 'Ag$_8$SnS$_6$' and 'Ag$_{8.1}$SnS$_6$'

We checked for phase purity of the ground samples using an Inel powder X-ray diffractometer with a position-sensitive detector utilizing Cu-Kα_1 radiation. No additional peaks other than those from the target compound were identified (Fig A-11).

Energy dispersive X-ray analysis and scanning electron microscopy were performed with a FEI Quanta FEG ESEM (with EDAX) with an acceleration voltage of 20 kV. The homogeneity of Ag_8SnS_6 after hot-pressing is demonstrated in Fig. A-14. The nominal compositions were determined by averaging three to four area scans on three pieces of the pellets after hot-pressing. No side products (e.g. binaries such as Ag_2S or SnS_2) and impurities (e.g. oxides, Si from reaction vessel) were detected. The Ag : Sn : S ratios matched closely the expected values, namely 52(1) : 6.6(8) : 41.1(6) for Ag_8SnS_6 (theoretical: 53.3 : 6.7 : 40.0) and 54.3(5) : 6.2(3) : 39.6(2) for '$Ag_{8.1}SnS_6$' (theoretical: 53.6 : 6.6 : 39.7).

A combined Differential Scanning Calorimetry and Thermal Gravimetry (DSC/TG) measurement was performed on a Netzsch STA 409 PC Luxx under a flow of argon to confirm the phase transition of Ag_8SnS_6 and to check for potential weight loss due to evaporation of sulfur.

The TG curve indicated that no noticeable weight loss occurred. The DSC curve revealed an endothermic peak upon heating around 453 K (Fig. A-12), and an exothermic peak at a slightly lower temperature upon cooling back to room temperature. This corresponds nicely to the low temperature orthorhombic to high temperature cubic phase transition at 457 K previously reported in literature.[100] The PXRD pattern obtained after the DSC and TG measurements showed no evidence of decomposition.

Electronic structure calculations were performed on the low temperature modification of Ag_8SnS_6 using the Density Functional Theory (DFT) within the WIEN2k program package,[153] which employs the full potential linearized augmented plane wave method (LAPW). First, we used the Perdew, Burke and Ernzerhof functional (PBE) for the generalized gradient approximation (GGA),[148] and then utilized the modified Becke-Johnson (mBJ) exchange potential correction for a more accurate band gap.[149] 216 independent *k* points on a grid of 8 × 17 × 12 points along the respective vectors of the reciprocal lattice were used for the iterative calculation, and iterations were performed until energy convergence was achieved within 0.0001 Ry.

5.3.2 Thermoelectric Properties and Stability of 'Ag_8SnS_6' and '$Ag_{8.1}SnS_6$'

Ag_8SnS_6 was reported to crystallize in the canfieldite structure type below 450 K, space group $Pna2_1$ in contrast to the argyrodite's space group $Pnm2_1$.[96] Its structure is comprised of a covalent network of AgS_4 and SnS_4 tetrahedra with numerous Ag–Ag contacts between 2.9 Å and 3.2 Å (Fig. 5.1a). Notably all atomic positions of the low temperature modification are fully occupied with no apparent disorders or deficiencies. As there are no vacancies for the additional Ag atoms in case of '$Ag_{8.1}SnS_6$', we expect the Sn and S sites to be slightly deficient to accommodate the change in stoichiometry, as in $Ag_8Sn_{0.99}S_{5.93}$.

Above 450 K, a cubic structure with highly disordered Ag sites in space group $F\bar{4}3m$ is adopted, with Ag site occupancies below 50% and a multitude of short distances between these sites, while the SnS_4 tetrahedra remain well ordered (Figure 5.1b).

The density of states of the low temperature modification of Ag_8SnS_6 is depicted in Fig. 5.2. Ag_8SnS_6 is a charge balanced semiconductor according to the formula $(Ag^+)_8(Sn^{4+})(S^{2-})_6$ with a calculated band gap of 1.3 eV, in qualitative agreement with the experimentally determined gap of 1.4 eV.[154] Previously, Shen et al. calculated a band gap of 0.40 eV,[100] however this underestimation was caused by the use of the density functional theory without any correction.[155]

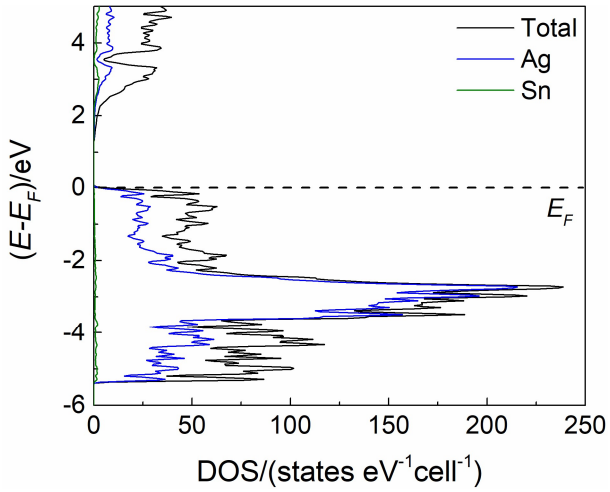

Figure 5.2. Density of states of the low temperature modification of Ag_8SnS_6.

The band structure of the low temperature modification of Ag_8SnS_6 is shown in Fig. 5.3. The bands from -2 eV to -4 eV are dominated by Ag 4*d* bands. The flat bands just below the Fermi level correspond to the filled 4*p* states of S. The bands above the Fermi level from 1.3 eV to 3.0 eV can be assigned to empty Ag and Sn states. The noticeably steep bands occur along a^* ($\Gamma \rightarrow$ X), b^* (Y $\rightarrow \Gamma$) and c^* (Z $\rightarrow \Gamma$), i.e. all three directions, which contributes to high velocity electrons if filled, in contrast to the flat bands below the Fermi level.

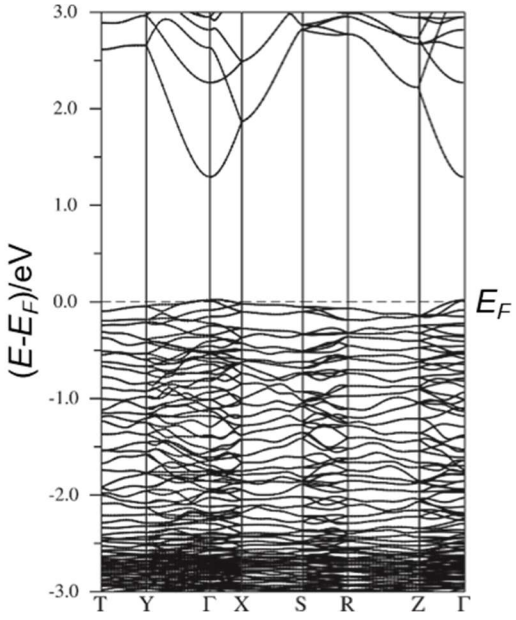

Figure 5.3. Band structure of the low temperature modification of Ag_8SnS_6.

A low temperature conductivity experiment was performed on Ag_8SnS_6, which displayed an exponential temperature dependence (Fig. 5.4a), indicative of intrinsic semiconducting behavior, and followed the Arrhenius' activation model ($\sigma = \sigma_o \exp(-\Delta E/(2kT))$, where k is the Boltzmann constant and ΔE is the activation energy). The activation energy was thus determined by plotting the electrical conductivity logarithmically as a function of inverse temperature (Fig. 5.4b). A linear curve was obtained with a slope equal to $-\Delta E/(2k)$, and the activation energy was calculated to be 0.58 eV.

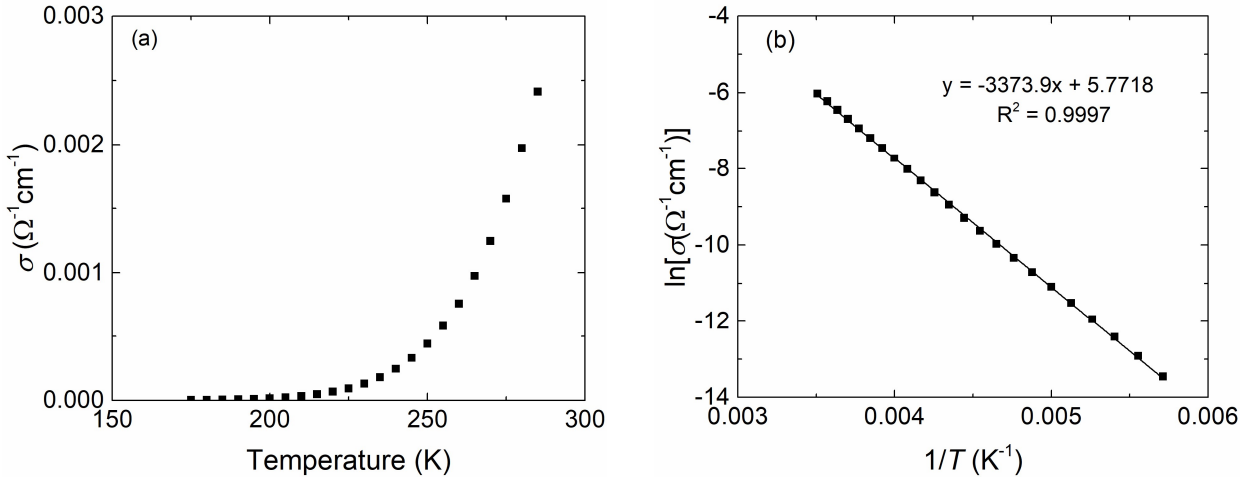

Figure 5.4. (a) Temperature dependent electrical conductivity of Ag_8SnS_6 and (b) the logarithmic dependence of electrical conductivity versus $1/T$.

The electrical conductivity of the high temperature modification of Ag_8SnS_6 was also studied from 470 K to 685 K with the ZEM-3 (Fig. 5.5a) simultaneously with the Seebeck coefficient (Fig. 5.5b). Attempts to determine the electrical conductivity between 300 K and 470 K were unsuccessful, due to the limitations of the ZEM-3 instrument when measuring samples with low conductivity. Measurements above 685 K resulted in the irreversible formation of Ag wires, limiting the temperature range to 470 K to 685 K. The formation of Ag wires is evidence of highly mobile Ag^+ ions at high temperatures. A similar behavior was observed in Cu_2Se, where Cu had precipitated into nanobundles on the surface of a bar that was held under (much higher) current flow for 24 hours.[91]

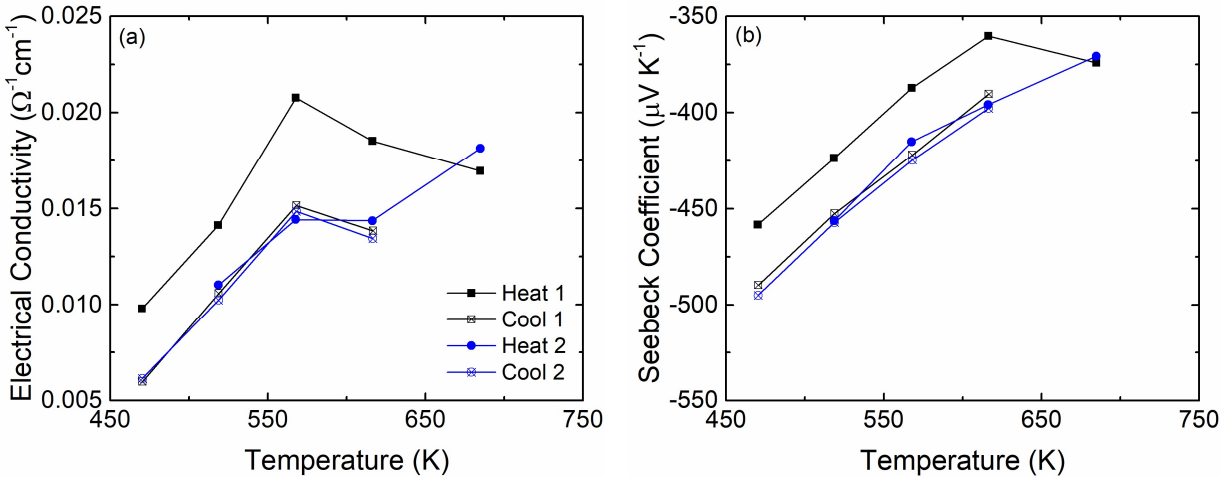

Figure 5.5. Temperature dependence of the (a) electrical conductivity and (b) Seebeck coefficient of Ag_8SnS_6.

The high temperature modification of Ag_8SnS_6 initially displayed a positive temperature dependence and very low electrical conductivity values, indicative of thermal activation as the main source of charge carriers. The first heating curve produced the highest σ values from 470 K to 565 K of 0.010 $\Omega^{-1}cm^{-1}$ to 0.021 $\Omega^{-1}cm^{-1}$ and then displayed a negative temperature dependence to 685 K with a final value of 0.017 $\Omega^{-1}cm^{-1}$. This negative temperature dependence could be due to the increasingly mobile Ag^+ ions above 565 K, resulting in many partially filled Ag atom sites and a gradient composition decreasing the mean free phonon path.

The first cooling curve generally showed significantly lower values, e.g. 0.006 $\Omega^{-1}cm^{-1}$ at 470 K, pointing to irreversible changes during the first cycle. The subsequent heating and cooling curves basically matched the values of the first cooling curve, indicating that stability has been achieved after the first cycle, as was observed in the case of Ag_9GaS_6.[156]

Generally, these values were lower than those reported for Ag_8SnS_6 by Shen et al. (σ from 5 $\Omega^{-1}cm^{-1}$ to 21 $\Omega^{-1}cm^{-1}$ from 525 K to 675 K).[100] Compared to the high-performance superionic conductors Cu_2Se (σ from 750 $\Omega^{-1}cm^{-1}$ to 250 $\Omega^{-1}cm^{-1}$ from 300 K to 900 K),[56] and the related

selenide, Ag_8SnSe_6 (σ from 235 $\Omega^{-1}cm^{-1}$ to 175 $\Omega^{-1}cm^{-1}$ from 423 K to 723 K),[112] the electrical conductivity values of Ag_8SnS_6 are uncompetitive.

Negative Seebeck coefficient values were obtained, indicating that Ag_8SnS_6 is an *n*-type semiconductor. The first heating curve showed a decrease in the absolute values of the Seebeck coefficient, decreasing from -470 μV K^{-1} to -360 μV K^{-1} from 470 K to 615 K. The first cooling curve displayed significantly higher absolute values, e.g. -470 μV K^{-1} at 470 K, once again demonstrating a lack of reproducibility during the first cycle. The subsequent heating and cooling curves matched the data of the first cooling curve, indicating again that no more irreversible changes occurred after the first heating.

These absolute values are higher than those obtained by Shen et al., who measured Seebeck coefficient values of -400 μV K^{-1} to -300 μV K^{-1} from 525 K to 675 K.[100] All of those are very competitive Seebeck coefficient values, for example in comparison to Cu_2Se (+75 μV K^{-1} to +250 μV K^{-1} from 300 K to 900 K) and Ag_8SnSe_6 (-150 μV K^{-1} to -180 μV K^{-1} from 300 K to 773 K).

In an effort to enhance the electrical conductivity and therefore the thermoelectric properties, we attempted to add more charge carriers (valence-electrons) by increasing the Ag content to the nominal composition '$Ag_{8.1}SnS_6$'. As mentioned previously, precipitation of Ag wires during electrical conductivity and Seebeck coefficient measurements of these materials above 685 K was observed, and in the case of Ag_8SnS_6, stability could be achieved after the first heating process by measuring within the appropriate temperature range. When initially attempting to determine the electrical properties of '$Ag_{8.1}SnS_6$', Ag wire formation was also observed above 685 K, with an even larger amount of Ag being precipitated. This revealed a reduced stability with the additional Ag content.

Limiting the current density to 0.15 μA cm^{-2} in the material of nominal composition '$Ag_{8.1}SnS_6$' was necessary during the measurement up to 770 K to avoid formation of Ag wires. Even in that case, irreversible changes still happened, as demonstrated in a decreased electrical conductivity after the first heating (Fig. 5.6a). Overall, the same positive temperature dependence as in case of Ag_8SnS_6 was observed, again indicative of thermal activation. The additional Ag enhanced the electrical conductivity substantially, with initial values of 0.13 $\Omega^{-1}cm^{-1}$ to 14 $\Omega^{-1}cm^{-1}$ from 480 K to 770 K. After two heating-cooling cycles, reproducibility was achieved, with lower σ values ranging from 0.12 $\Omega^{-1}cm^{-1}$ to 6.9 $\Omega^{-1}cm^{-1}$ within the same temperature range.

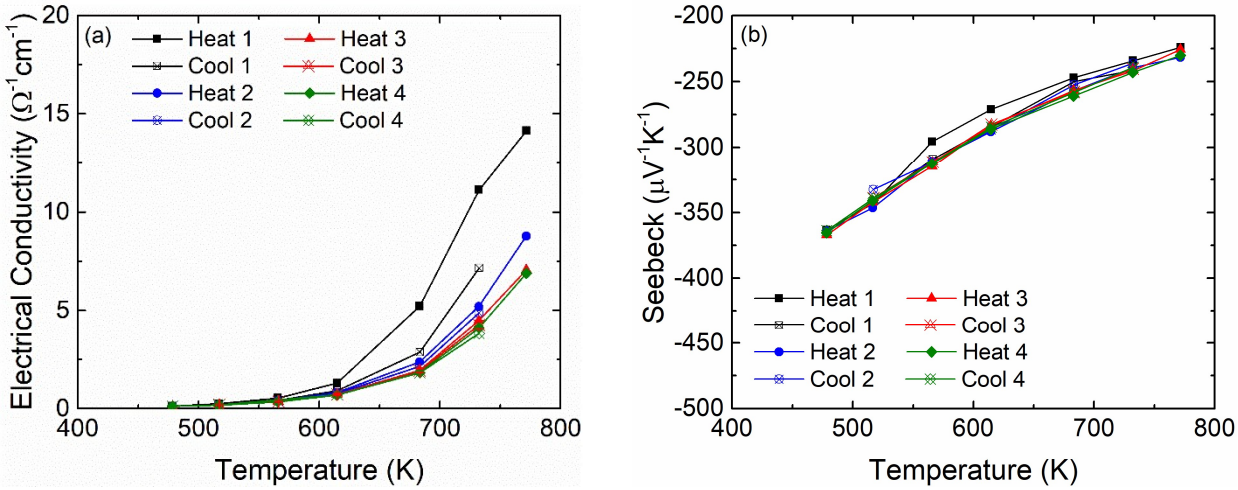

Figure 5.6. Temperature dependence of the (a) electrical conductivity and (b) Seebeck coefficient of '$Ag_{8.1}SnS_6$'.

The absolute values of the Seebeck coefficient (Fig. 5.6b) decreased as expected (*S* from -365 μV K^{-1} to -230 μV K^{-1} from 480 K to 770 K) in comparison to Ag_8SnS_6, as there was an overall increase in the electrical conductivity.

The first thermal diffusivity measurement was performed on a pellet of Ag_8SnS_6 from room temperature up to 850 K, which resulted in the formation of two distinctly different kinds of wires

on the surface, that faced the laser during the measurement, e.g. the hotter side. An EDAX analysis indicated the formation of both Ag and Ag_2S wires on the surface of the pellet (Fig. 5.7).

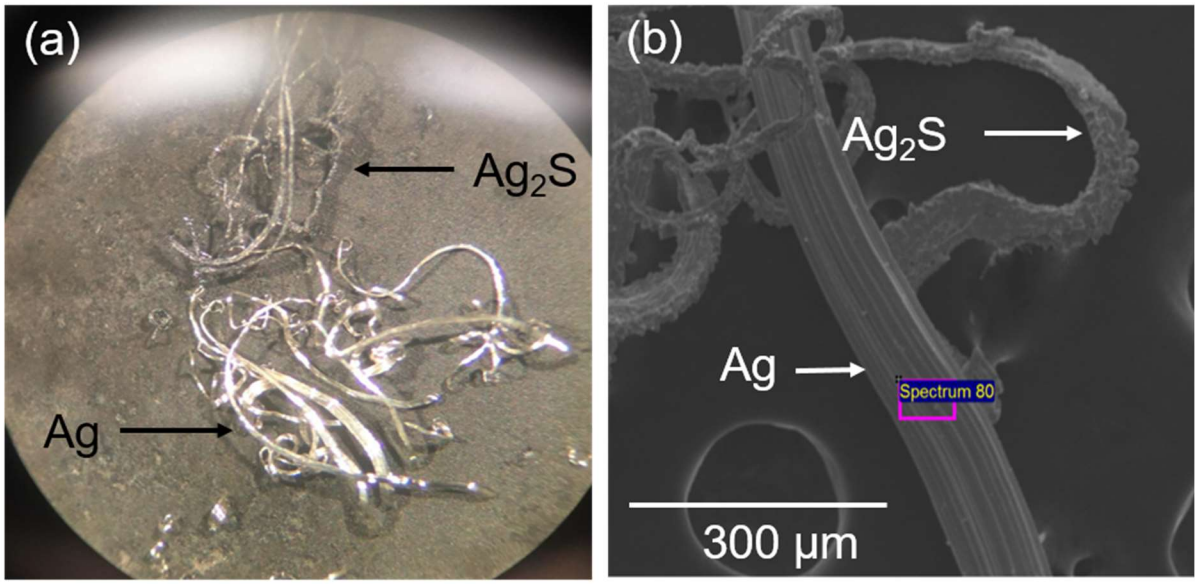

Figure 5.7. Presence of Ag and Ag_2S wires on the surface of a pellet of Ag_8SnS_6 after the thermal diffusivity measurement up to 850 K; (a) a view of the whole pellet of 12.7 mm diameter; (b) a higher magnification demonstrating the different morphologies of the Ag and the Ag_2S wires.

Based on these observations, the temperature dependence of the thermal conductivity for both Ag_8SnS_6 and $Ag_{8.1}SnS_6$ was investigated from 290 K to only 785 K (Fig. 5.8). Both materials exhibited very low thermal conductivity values throughout the entire temperature range. In accord with the higher stability of Ag_8SnS_6 compared to '$Ag_{8.1}SnS_6$' observed during the electrical measurements, only the former exhibited reversible curves in contrast to the latter. Here, the phase transition around 450 K in case of Ag_8SnS_6 occurs with a local minimum, which appeared to be shifted towards lower temperatures in case of the Ag-rich sample.

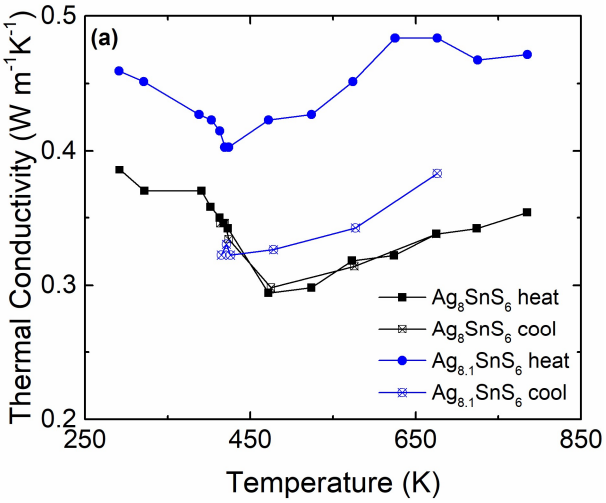

Figure 5.8. Temperature dependence of the thermal conductivity of Ag_8SnS_6 and '$Ag_{8.1}SnS_6$'.

Ag_8SnS_6 displayed a negative temperature dependence of the thermal conductivity from 290 K to 453 K (from 0.39 W $m^{-1}K^{-1}$ to 0.29 W $m^{-1}K^{-1}$). Because of the low electrical conductivity, these values stem to over 99% from the lattice thermal conductivity. From 453 K to 785 K, e.g. above the phase transition, the material exhibited a positive temperature dependence from 0.29 W $m^{-1}K^{-1}$ to 0.35 W $m^{-1}K^{-1}$. The heating curve of the material of nominal composition $Ag_{8.1}SnS_6$ exhibited the same trends as Ag_8SnS_6, however the thermal conductivity values were higher. A negative temperature dependence is displayed from 290 K to 420 K (from 0.46 W $m^{-1}K^{-1}$ to 0.40 W $m^{-1}K^{-1}$), and then a positive temperature dependence until 785 K (from 0.40 W $m^{-1}K^{-1}$ to 0.47 W $m^{-1}K^{-1}$). Upon cooling, significantly lower values were obtained, demonstrating lack of stability due to irreversible changes likely caused by the temperature gradient generated by the laser of the instrument. This demonstrated again the lower stability of '$Ag_{8.1}SnS_6$' in comparison to Ag_8SnS_6.

After removal from the instrument, it was noted that Ag wires (Fig. 5.9) had appeared on the surface on the '$Ag_{8.1}SnS_6$' pellet facing the laser, while the pellet of Ag_8SnS_6 remained clean,

without any noticeable wire formation. This explains the lack of reproducibility in case of '$Ag_{8.1}SnS_6$'.

Figure 5.9. Pellet of '$Ag_{8.1}SnS_6$' after the thermal diffusivity measurement up to 785 K.

Regardless, both Ag_8SnS_6 and '$Ag_{8.1}SnS_6$' have highly competitive thermal conductivity values in comparison to Cu_2Se (1.2 W $m^{-1}K^{-1}$ to 0.6 W $m^{-1}K^{-1}$ at 300 K to 900 K) and Ag_8SnSe_6 (0.45 W $m^{-1}K^{-1}$ to 0.35 W $m^{-1}K^{-1}$ at 423 K to 723 K). The thermal conductivity values obtained for Ag_8SnS_6 by Shen et al. were slightly higher (0.30 W $m^{-1}K^{-1}$ to 0.38 W $m^{-1}K^{-1}$ from 300 K to 773 K) and did not display the sharp decrease in thermal conductivity values between 391 K and 453 K.[100]

Because of the instability during the first cycles, the figure of merit values *zT* were calculated from the second heating curve of Ag_8SnS_6 and the fourth heating curve of '$Ag_{8.1}SnS_6$' of the electrical measurements and the first heating curve of the thermal measurements. Furthermore, the calculation of *zT* was limited to 615 K in case of '$Ag_{8.1}SnS_6$'. This was due to the flattening of the thermal conductivity curve around 625 K, which is not observed in the curve of Ag_8SnS_6 (which displays a positive temperature dependence). This 'flattening' could be attributed to the formation of silver wires at higher temperatures. Even so, these *zT* calculations need to be considered with caution, as the exact onset of Ag wire formation is not clear.

Disregarding these limitations, the zT values for both Ag_8SnS_6 and '$Ag_{8.1}SnS_6$' as-prepared are both very low (Fig. 5.10) because of the low electrical conductivity. The zT values for Ag_8SnS_6 ranged from 2x 10^{-4} to 5x 10^{-4} between 470 K and 685 K, while '$Ag_{8.1}SnS_6$' had values of 0.002 to 0.006 between 480 K and 615 K. In comparison to the values determined for Ag_8SnS_6 by Shen et al. (zT = 0.06 at 615 K and 0.5 at 773 K),[100] our figure of merit values were significantly lower, most likely a consequence of lower charge carrier concentrations as seen in the significantly lower electrical conductivity.

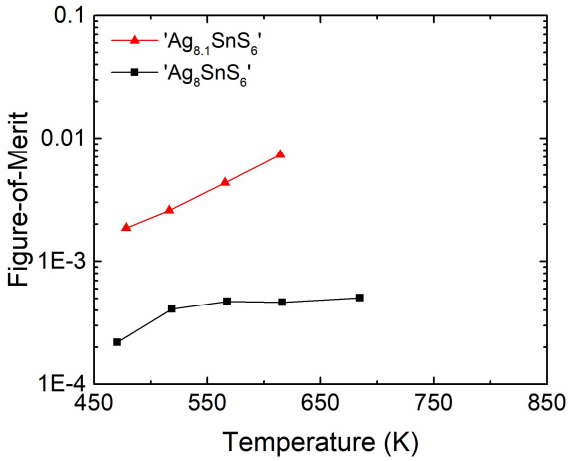

Figure 5.10. Temperature dependence of the figure of merit of Ag_8SnS_6 and '$Ag_{8.1}SnS_6$'.

5.4 Conclusion

This chapter aimed to address the stability issues regarding Ag_8SnS_6, as well as enhancing the thermoelectric properties with additional silver. We confirmed that Ag_8SnS_6 is an *n*-type semiconductor with ultralow thermal conductivity. As-prepared, it exhibited high absolute values of the Seebeck coefficient, and low electrical conductivity. The latter can be enhanced by adding more Ag, as demonstrated here, or by increasing the carrier concentration as shown by Shen et al.[100]

Our measurements demonstrated that stability concerns for this sulfide were indeed well founded, as standard data collections resulted in the formation of Ag wires. In case of Ag_8SnS_6, we found out that limiting the temperatures to remain below 685 K was sufficient to avoid Ag wire formation and achieve reproducibility in the second measurement cycle. In case of '$Ag_{8.1}SnS_6$', a reduction of the current density was also required. These findings indicate that special care needs to be applied when investigating such canfieldites, and other ionic conductors, for usage as thermoelectric materials. Doping with immobile cations might mitigate against this detrimental ionic conductivity, as for example demonstrated for the case of Cu_2Se.

CHAPTER 6: Summary and Outlook

The work presented in this thesis examined three different coinage metal chalcogenides for their potential use as thermoelectric materials. The overarching goal was to use the intrinsic nature of the materials (e.g. heavy atoms, complicated crystal structures) as a starting point and modify the carrier concentrations in order to improve the thermoelectric performance.

Chapter three presents the materials $Cu_5Sn_2Q_7$ (where Q = Se, Te), which both exhibit metal-like behavior with high electrical and thermal conductivity and low thermopower. By doping both compounds with Zn, the amount of charge carriers decreased, and therefore a dramatic increase in the thermopower was achieved from +16 μV K^{-1} for $Cu_5Sn_2Se_7$ to +80 μV K^{-1} for $Cu_4ZnSn_2Se_7$, and from +9 μV K^{-1} for $Cu_5Sn_2Te_7$ to +21 μV K^{-1} for $Cu_4ZnSn_2Te_7$ (all data at 300 K). Moreover, the electrical conductivity and thermal conductivity decreased. Ultimately $Cu_4ZnSn_2Se_7$ achieved a zT of 0.20 at 630 K and $Cu_4ZnSn_2Te_7$a zT of 0.05 at 575 K. Although the thermoelectric properties as a whole improved, these materials are not yet suitable for use in thermoelectric devices because of their still relatively high thermal conductivity. Further work could be performed to improve the figure of merit by further decreasing the thermal conductivity by introducing mass fluctuations or nanostructuring, but these improvements would not turn these materials into competitive thermoelectrics.

Chapter four revisits $Ba_3Cu_{14-\delta}Te_{12}$, which was previously discovered and characterized by the Kleinke group. The previous study did not observe a correlation between copper deficiency and any of the thermoelectric properties. In this thesis, the samples were hot-pressed, and subsequently it was noted that increasing the Cu defects δ in $Ba_3Cu_{14-\delta}Te_{12}$ caused an increase in the electrical conductivity. The thermal conductivity values were very competitive (< 1 W $m^{-1}K^{-1}$), however the thermopower values were poor. Due to the uncompetitive thermopowers, the

figure of merit values were not competitive either, with $Ba_3Cu_{13.175}Te_{12}$ exhibiting the highest peak *zT* of 0.12 at 570 K. Stability of these materials is an issue, but problems can be avoided by staying below a maximum temperature of 600 K. In order for $Ba_3Cu_{14-\delta}Te_{12}$ to be more competitive, the Seebeck coefficient should be improved. Due to the already appropriate electrical and thermal conductivity, nanostructuring (e.g. introduction of grain boundaries or nanodomains) should be implemented, which would increase the thermopower while retaining the electrical conductivity. However, due to the currently very low figure of merit, it is unlikely that any improvements would result in $Ba_3Cu_{14-\delta}Te_{12}$ becoming a competitive thermoelectric material.

Chapter five studies the stability and thermoelectric properties of the mixed ion-electron conductor Ag_8SnS_6. First measurements revealed serious stability problems with Ag and Ag_2S wires forming during the data collection. It was found that stability could be achieved when the operating temperature was limited, as well as the amount of current placed through the sample. By doing so, silver wires would not precipitate out of the sample anymore during physical property measurements. The maximum figure of merit was previously reported to be 0.5 at 750 K. Since Ag_8SnS_6 is charge compensated, with a low carrier concentration, the electrical conductivity was increased by introducing additional Ag atoms. The electrical conductivity overall increased from 0.17 $\Omega^{-1}cm^{-1}$ at 685 K (no additional Ag) to 6.9 $\Omega^{-1}cm^{-1}$ at 770 K (additional Ag). Since the electrical conductivity is still too low as well as issues with the stability limit the operating temperatures and currents, the canfieldite is not suitable for thermoelectrics without further modifications. In order for Ag_8SnS_6 to become a competitive thermoelectric material, the electrical conductivity should be increased. This could be done by doping with a 3+ cation, such as indium or antimony on the Sn site. Then the stability issues remain to be solved, which might be done via doping with immobile cations.

References

(1) He, J.; Tritt, T. M. Advances in Thermoelectric Materials Research: Looking Back and Moving Forward. *Science* **2017**, *357*, 1369/1-11.

(2) Bell, L. E. Cooling, Heating, Generating Power, and Recovering Waste Heat with Thermoelectric Systems. *Science* **2008**, *321*, 1457–1461.

(3) Hinderman, J. D. *Thermoelectric Materials Evaluation Program Annual Technical Report for Fiscal Years 1980/1981*; United States, 1981.

(4) Yang, Y.; Wei, X.-J.; Liu, J. Suitability of Thermoelectric Power Generator for Implantable Medical Devices. *J. Phys. D. Appl. Phys.* **2007**, *40*, 5790–5800.

(5) Leonov, V.; Vullers, R. J. M. Wearable Electronics Self-Powered by Using Human Body Heat: The State of the Art and the Perspective. *J. Renew. Sustain. Energy* **2009**, *1*, 062701/1-17.

(6) Francioso, L.; De Pascali, C.; Farella, I.; Martucci, C.; Cretì, P.; Siciliano, P.; Perrone, A. Flexible Thermoelectric Generator for Ambient Assisted Living Wearable Biometric Sensors. *J. Power Sources* **2011**, *196*, 3239–3243.

(7) Elsheikh, M. H.; Shnawah, D. A.; Sabri, M. F. M.; Said, S. B. M.; Hassan, M. H.; Bashir, M. B. A.; Mohamad, M. A Review on Thermoelectric Renewable Energy: Principle Parameters That Affect Their Performance. *Renew. Sustain. Energy Rev.* **2014**, *30*, 37–355.

(8) Dai, Y. J.; Wang, R. Z.; Ni, L. Experimental Investigation on a Thermoelectric Refrigerator Driven by Solar Cells. *Renew. Energy* **2003**, *28*, 949–959.

(9) Sharma, S.; Dwivedi, V. K.; Pandit, S. N. A Review of Thermoelectric Devices for Cooling Applications. *Int. J. Green Energy* **2014**, *11*, 899–909.

(10) Yang, L.; Chen, Z. G.; Dargusch, M. S.; Zou, J. High Performance Thermoelectric Materials: Progress and Their Applications. *Adv. Energy Mater.* **2018**, *8*, 1701797/1-28.

(11) Shin, W.; Imai, K.; Izu, N.; Murayama, N. Thermoelectric Thick-Film Hydrogen Gas Sensor Operating at Room Temperature. *Jpn. J. Appl. Phys* **2001**, *40*, L1232–L1234.

(12) Park, N.-H.; Akamatsu, T.; Itoh, T.; Izu, N.; Shin, W. Calorimetric Thermoelectric Gas Sensor for the Detection of Hydrogen, Methane and Mixed Gases. *Sensors* **2000**, *14*, 8350–8362.

(13) Swan, M. Sensor Mania! The Internet of Things, Wearable Computing, Objective Metrics, and the Quantified Self 2.0. *J. Sens. Actuator Networks* **2012**, *1*, 217–253.

(14) Zaia, E. W.; Gordon, M. P.; Yuan, P.; Urban, J. J. Progress and Perspective: Soft Thermoelectric Materials for Wearable and Internet-of-Things Applications. *Adv. Electron. Mater.* **2019**, *5*, 1800823/1-20.

(15) Freer, R.; Powell, A. V. Realising the Potential of Thermoelectric Technology: A Roadmap. *J. Mater. Chem. C* **2020**, *8*, 441–463.

(16) Ohta, M.; Jood, P.; Murata, M.; Lee, C.-H.; Yamamoto, A.; Obara, H. An Integrated Approach to Thermoelectrics: Combining Phonon Dynamics, Nanoengineering, Novel

Materials Development, Module Fabrication, and Metrology. *Adv. Energy Mater.* **2019**, 1801304/1-29.
(17) Snyder, G. J.; Toberer, E. S. Complex Thermoelectric Materials. *Nat. Mater.* **2008**, *7*, 105–114.
(18) Rowe, D. M. *Thermoelectrics Handbook: Macro to Nano*; Taylor & Francis Group: Boca Raton, FL, USA, 2006.
(19) Nolas, G. S.; Morelli, D. T.; Tritt, T. M. Skutterudites: A Phonon-Glass-Electron Crystal Approach to Advanced Thermoelectric Energy Conversion Applications. *Annu. Rev. Mater. Sci.* **1999**, *29*, 89–116.
(20) West, A. R. *Solid State Chemistry and Its Applications*, 2nd ed.; John Wiley & Sons, Ltd: West Sussex, 2014.
(21) Greig, D. *Electrons in Metals and Semiconductors*; McGraw-Hill: London, UK, 1969.
(22) Macia-Barber, E. *Thermoelectric Materials Advances and Applications*; CRC Press, Taylor & Francis Group: Boca Raton, 2015.
(23) Cutler, M.; Mott, N. F. Observation of Anderson Localization in an Electron Gas. *Phys. Rev.* **1969**, *181*, 1336–1340.
(24) *Thermal Conductivity*; Tritt, T. M., Ed.; Physics of Solids and Liquids; Springer US: New York, 2004.
(25) Wang, H.; Porter, W. D.; Böttner, H.; König, J.; Chen, L.; Bai, S.; Tritt, T. M.; Mayolet, A.; Senawiratne, J.; Smith, C.; Harris, F.; Gilbert, P.; Sharp, J.; Lo, J.; Kleinke, H.; Kiss, L. Transport Properties of Bulk Thermoelectrics: An International Round-Robin Study, Part II: Thermal Diffusivity, Specific Heat, and Thermal Conductivity. *J. Electron. Mater.* **2013**, *42*, 1073–1084.
(26) O'Neill, M. J. Measurement of Specific Heat Functions by Differential Scanning Calorimetry. *Anal. Chem.* **1966**, *38*, 1331–1336.
(27) Franz, R.; Wiedemann, G. Ueber Die Wärme-Leitungsfähigkeit Der Metalle. *Ann. der Phys. und Chemie* **1853**, *165*, 497–531.
(28) Lucas, A.; Das Sarma, S. *Electronic Hydrodynamics and the Breakdown of the Wiedemann-Franz and Mott Laws in Interacting Metals*; 2018.
(29) Kim, H.-S.; Gibbs, Z. M.; Tang, Y.; Wang, H.; Snyder, G. J. Characterization of Lorenz Number with Seebeck Coefficient Measurement. *APL Mater.* **2015**, *3*, 041506/1-5.
(30) Fleurial, J. .; Gaailliard, L.; Triboulet, R.; Scherrer, H.; Scherrer, S. Thermal Properties of High Quality Single Crystals of Bismuth Telluride-Part I: Experimental Characterization. *J. Phys. Chem. Solids* **1988**, *49*, 1237–1247.
(31) Chen, Z.-G.; Shi, X.; Zhao, L.-D.; Zou, J. High-Performance SnSe Thermoelectric Materials: Progress and Future Challenge. *Prog. Mater. Sci.* **2018**, *97*, 283–346.
(32) Wu, L.; Zheng, J.-C.; Zhou, J.; Li, Q.; Yang, J.; Zhu, Y. Nanostructures and Defects in Thermoelectric $AgPb_{18}SbTe_{20}$ Single Crystal. *J. Appl. Phys.* **2009**, *105*, 94317/1-9.
(33) Xie, W.; Tang, X.; Yan, Y.; Zhang, Q.; Tritt, T. M. Unique Nanostructures and Enhanced Thermoelectric Performance of Melt-Spun BiSbTe Alloys. *Appl. Phys. Lett* **2009**, *94*,

102111/1-3.
(34) Wu, F.; Song, H.; Gao, F.; Shi, W.; Jia, J.; Hu, X. Effects of Different Morphologies of Bi_2Te_3 Nanopowders on Thermoelectric Properties. *J. Electron. Mater.* **2013**, *42*, 1140–1145.
(35) Fu, Y.; Xu, J.; Liu, G.-Q.; Yang, J.; Tan, X.; Liu, Z.; Qin, H.; Shao, H.; Jiang, H.; Liang, B.; Jiang, J. Enhanced Thermoelectric Performance in P-Type Polycrystalline SnSe Benefiting from Texture Modulation. *J. Mater. Chem. C* **2016**, *4*, 1201–1207.
(36) Chotia, C.; Singh Okram, G.; Kuo, Y.-K.; Hussain, S. Enhanced Thermoelectric Properties of $(SnS)_{1-x}$ $(SnO)_x$: $X < 10.79\%$ Nanocomposites Prepared by Polyol Method. *J. Mater. Sci. Mater. Electron.* **2021**, *32*, 10702–10711.
(37) Sturm, C.; Jafarzadeh, P.; Kleinke, H. Thermoelectric Nanomaterials. In *Comprehensive Nanoscience and Nanotechnology*; Andrews, D. L., Lipson, R. H., Nann, T., Eds.; Academic Press, 2019; pp 349–358.
(38) Poudel, B.; Hao, Q.; Ma, Y.; Lan, Y.; Minnich, A.; Yu, B.; Yan, X.; Wang, D.; Muto, A.; Vashaee, D.; Chen, X.; Liu, J.; Dresselhaus, M. S.; Chen, G.; Ren, Z. High-Thermoelectric Performance of Nanostructured Bismuth Antimony Telluride Bulk Alloys. *Science* **2008**, *320*, 634–638.
(39) Hao, F.; Qiu, P.; Tang, Y.; Bai, S.; Xing, T.; Chu, H.-S.; Zhang, Q.; Lu, P.; Zhang, T.; Ren, D.; Chen, J.; Shi, X.; Chen, L. High Efficiency Bi_2Te_3-Based Materials and Devices for Thermoelectric Power Generation between 100°C and 300°C. *Energy Environ. Sci.* **2016**, *9*, 3120–3127.
(40) Zhao, L.-D.; Lo, S.-H.; Zhang, Y.; Sun, H.; Tan, G.; Uher, C.; Wolverton, C.; Dravid, V. P.; Kanatzidis, M. G. Ultralow Thermal Conductivity and High Thermoelectric Figure of Merit in SnSe Crystals. *Nature* **2014**, *508*, 373–377.
(41) Heremans, J. P.; Jovovic, V.; Toberer, E. S.; Saramat, A.; Kurosaki, K.; Charoenphakdee, A.; Yamanaka, S.; Snyder, G. J. Enhancement of Thermoelectric Efficiency in PbTe by Distortion of the Electronic Density of States. *Science* **2008**, *321*, 554–557.
(42) Pei, Y.; LaLonde, A.; Iwanaga, S.; Snyder, J. High Thermoelectric Figure of Merit in Heavy Hole Dominated PbTe. *Energy Environ. Sci.* **2011**, *7*, 2085–2089.
(43) Adam, A. M.; El-Khouly, A.; Novitskii, A. P.; Ibrahim, E. M. M.; Kalugina, A. V.; Pankratova, D. S.; Taranova, A. I.; Sakr, A. A.; Trukhanov, A. V.; Salem, M. M.; Khovaylo, V. Enhanced Thermoelectric Figure of Merit in Bi-Containing Sb_2Te_3 Bulkcrystalline Alloys. *J. Phys. Chem. Solids* **2020**, *138*, 109262/1-6.
(44) Xie, L.; Qin, H.; Zhu, J.; Yin, L.; Qin, D.; Guo, F.; Cai, W.; Zhang, Q.; Sui, J. Realizing Excellent Thermoelectric Performance of Sb_2Te_3 Based Segmented Leg with a Wide Temperature Range Using One-Step Sintering. *Adv. Electron. Mater.* **2020**, *6*, 1901178/1-8.
(45) Shi, Y.; Assoud, A.; Ponou, S.; Lidin, S.; Kleinke, H. A New Material with a Composite Crystal Structure Causing Ultralow Thermal Conductivity and Outstanding Thermoelectric Properties: $Tl_2Ag_{12}Te_{7+\delta}$. *J. Am. Chem. Soc.* **2018**, *140*, 8578–8585.

(46) Guo, Q.; Assoud, A.; Kleinke, H. Improved Bulk Materials with Thermoelectric Figure-of-Merit Greater than 1: $Tl_{10-x}Sn_xTe_6$ and $Tl_{10-x}Pb_xTe_6$. *Adv. Energy Mater.* **2014**, *4*, 1400348/1-8.

(47) Plirdpring, T.; Kurosaki, K.; Kosuga, A.; Day, T.; Firdosy, S.; Ravi, V.; Snyder, G. J.; Harnwunggmoung, A.; Sugahara, T.; Ohishi, Y.; Muta, H.; Yamanaka, S. Chalcopyrite $CuGaTe_2$: A High-Efficiency Bulk Thermoelectric Material. *Adv. Mater.* **2012**, *24*, 3622–3626.

(48) Ahmed, F.; Tsujii, N.; Matsushita, Y.; Sauerschnig, P.; Mori, T. Influence of Slight Substitution (Mn/In) on Thermoelectric and Magnetic Properties in Chalcopyrite-Type $CuInTe_2$. *J. Electron. Mater.* **2019**, *48*, 4524–4532.

(49) Kosuga, A.; Matsuzawa, M.; Horie, A.; Omoto, T.; Funahashi, R. High-Temperature Thermoelectric Properties and Thermal Stability in Air of Copper Zinc Tin Sulfide for the p-Type Leg of Thermoelectric Devices. *Jpn. J. Appl. Phys.* **2015**, *54*, 061801/1-6.

(50) Zhang, J.; Liu, R.; Cheng, N.; Zhang, Y.; Yang, J.; Uher, C.; Shi, X.; Chen, L.; Zhang, W. High-Performance Pseudocubic Thermoelectric Materials from Non-Cubic Chalcopyrite Compounds. *Adv. Mater.* **2014**, *26*, 3848–3853.

(51) Tippireddy, S.; Chetty, R.; Naik, M. H.; Jain, M.; Chattopadhyay, K.; Mallik, R. C. Electronic and Thermoelectric Properties of Transition Metal Substituted Tetrahedrites. *J. Phys. Chem. C* **2018**, *122*, 8735–8749.

(52) Chetty, R.; Bali, A.; Mallik, R. C. Tetrahedrites as Thermoelectric Materials: An Overview. *J. Mater. Chem. C* **2015**, *3*, 12364–12378.

(53) Shi, Y.; Sturm, C.; Kleinke, H. Chalcogenides as Thermoelectric Materials. *J. Solid State Chem.* **2019**, *270*, 273–279.

(54) Suekuni, K.; Takabatake, T. Research Update: Cu–S Based Synthetic Minerals as Efficient Thermoelectric Materials at Medium Temperatures. *APL Mater.* **2016**, *4*, 104503/1-11.

(55) Long, S. O. J.; Powell, A. V; Vaqueiro, P.; Hull, S. High Thermoelectric Performance of Bornite through Control of the Cu(II) Content and Vacancy Concentration. *Chem. Mater.* **2018**, *30*, 456–464.

(56) Ballikaya, S.; Chi, H.; Salvador, J. R.; Uher, C. Thermoelectric Properties of Ag-Doped Cu_2Se and Cu_2Te. *J. Mater. Chem. A* **2013**, *1*, 12478–12484.

(57) He, Y.; Zhang, T.; Shi, X.; Wei, S. H.; Chen, L. High Thermoelectric Performance in Copper Telluride. *NPG Asia Mater.* **2015**, *7*, 1–7.

(58) Liu, H.; Shi, X.; Xu, F.; Zhang, L.; Zhang, W.; Chen, L.; Li, Q.; Uher, C.; Day, T.; Snyder, G. J. Copper Ion Liquid-like Thermoelectrics. *Nat. Mater.* **2012**, *11*, 422–425.

(59) Pavan Kumar, V.; Supka, A. R.; Lemoine, P.; Lebedev, O. I.; Raveau, B.; Suekuni, K.; Nassif, V.; Al Rahal Al Orabi, R.; Fornari, M.; Guilmeau, E. High Power Factors of Thermoelectric Colusites $Cu_{26}T_2Ge_6S_{32}$ (T = Cr, Mo, W): Toward Functionalization of the Conductive "Cu-S" Network. *Adv. Energy Mater.* **2019**, *9*, 1803429/1-11.

(60) Zavjalov, A.; Tikhonov, S.; Kosyanov, D. TiO_2-$SrTiO_3$ Biphase Nanoceramics as

Advanced Thermoelectric Materials. *Materials* **2019**, *12*, 2895/1-31.
(61) Yu, J.; Xia, K.; Zhao, X.; Zhu, T. High Performance P-Type Half-Heusler Thermoelectric Materials. *J. Phys. D* **2018**, *51*, 113001/1-15.
(62) Wei, T-R.; Qin, Y.; Deng, T.; Song, Q.; Jiang, B.; Liu, R.; Qiu, P.; Shi, X.; Chen, L. Copper Chalcogenide Thermoelectric Materials. *Sci. China Mater.* **2019**, *62*, 8-24.
(63) Lei, J.; Ma, Z.; Zhang, D.; Chen, Y.; Wang, C.; Yang, X.; Cheng, Z.; Wang, Y. High Thermoelectric Performance in Cu_2Se Superionic Conductor with Enhanced Liquid-like Behavior by Dispersing SiC. *J. Mater. Chem. A* **2019**, *7*, 7006–7014.
(64) Lorenzi, B.; Contento, G.; Sabatelli, V.; Rizzo, A.; Narducci, D. Theoretical Analysis of Two Novel Hybrid Thermoelectric-Photovoltaic Systems Based on Cu_2ZnSnS_4 Solar Cells. *J. Nanosci. Nanotechnol.* **2017**, *17*, 1608–1615.
(65) Zeier, W. G.; Zhu, H.; Gibbs, Z. M.; Ceder, G.; Tremel, W.; Snyder, G. J. Band Convergence in the Non-Cubic Chalcopyrite Compounds Cu_2MGeSe_4. *J. Mater. Chem. C* **2014**, *2*, 10189–10194.
(66) Isotta, E.; Mukherjee, B.; Fanciulli, C.; Pugno, N. M.; Scardi, P. Order−Disorder Transition in Kesterite Cu_2ZnSnS_4: Thermopower Enhancement via Electronic Band Structure Modification. *J. Phys. Chem. C* **2020**, *124*, 7091–7096.
(67) Schäfer, W.; Nitsche, R. Tetrahedral Quaternary Chalcogenides. *Mat. Res. Bull* **1974**, *9*, 645–654.
(68) Raju, C.; Falmbigl, M.; Rogl, P.; Yan, X.; Bauer, E.; Horky, J.; Zehetbauer, M.; Mallik, R. C. Thermoelectric Properties of Chalcogenide Based $Cu_{2+x}ZnSn_{1-x}Se_4$. *AIP Adv.* **2013**, *3*, 032106/1-12.
(69) Liu, M.-L.; Huang, F.-Q.; Chen, L.-D.; Chen, I.-W. A Wide-Band-Gap *p*-Type Thermoelectric Material Based on Quaternary Chalcogenides of Cu_2ZnSnQ_4 (Q = S, Se). *Appl. Phys. Lett* **2009**, *94*, 202103/1-3.
(70) Tiwari, K. J.; Kumar, D. S. P.; Mallik, R. C.; Malar, P. Ball Mill Synthesis of Bulk Quaternary $Cu_2ZnSnSe_4$ and Thermoelectric Studies. *J. Electron. Mater.* **2017**, *46*, 30–39.
(71) Yang, H.; Jauregui, L. A.; Zhang, G.; Chen, Y. P.; Wu, Y. Nontoxic and Abundant Copper Zinc Tin Sulfide Nanocrystals for Potential High-Temperature Thermoelectric Energy Harvesting. *Nano Lett.* **2012**, *12*, 540–545.
(72) Kikuchi, Y.; Bouyrie, Y.; Ohta, M.; Suekuni, K.; Aihara, M.; Takabatake, T. Vanadium-Free Colusites $Cu_{26}A_2Sn_6S_{32}$ (A = Nb, Ta) for Environmentally Friendly Thermoelectrics. *J. Mater. Chem. A* **2016**, *4*, 15207–15214.
(73) Lu, X.; Morelli, D. T.; Xia, Y.; Zhou, F.; Ozolins, V.; Chi, H.; Zhou, X.; Uher, C. High Performance Thermoelectricity in Earth-Abundant Compounds Based on Natural Mineral Tetrahedrites. *Adv. Energy Mater.* **2013**, *3*, 342–348.
(74) Nielsen, M. D.; Ozolins, V.; Heremans, J. P. Lone Pair Electrons Minimize Lattice Thermal Conductivity. *Energy Environ. Sci.* **2013**, *6*, 570–578.
(75) Lai, W.; Wang, Y.; Morelli, D. T.; Lu, X. From Bonding Asymmetry to Anharmonic Rattling in $Cu_{12}Sb_4S_{13}$ Tetrahedrites: When Lone-Pair Electrons Are Not So Lonely. *Adv.*

Funct. Mater. **2015**, *25*, 3648–3657.
(76) Cui, Y.; Assoud, A.; Xu, J.; Kleinke, H. Structures and Physical Properties of New Semiconducting Gold and Copper Polytellurides: $Ba_7Au_2Te_{14}$ and $Ba_{6.76}Cu_{2.42}Te_{14}$. *Inorg. Chem.* **2007**, *46*, 1215–1221.
(77) Mayasree, O.; Cui, Y.; Assoud, A.; Kleinke, H. Structure Change via Partial Se/Te Substitution: Crystal Structure and Physical Properties of the Telluride $Ba_2Cu_{4-x}Te_5$ in Contrast to the Selenide-Telluride $Ba_2Cu_{4-x}Se_Y$. *Inorg. Chem.* **2010**, *49*, 6518–6524.
(78) Jafarzadeh, P.; Menezes, L. T.; Cui, M.; Assoud, A.; Zhang, W.; Shiv Halasyamani, P.; Kleinke, H. $BaCuSiTe_3$: A Noncentrosymmetric Semiconductor with $CuTe_4$ Tetrahedra and Ethane-like Si_2Te_6 Units. *Inorg. Chem* **2019**, *58*, 11656–11663.
(79) Jafarzadeh, P.; Assoud, A.; Ramirez, D.; Farahi, N.; Zou, T.; Müller, E.; Kycia, J. B.; Kleinke, H. Thermoelectric Properties and Stability of $Ba_3Cu_{16-x}Se_{11-y}Te_Y$. *J. Appl. Phys* **2019**, *126*, 25109/1-9.
(80) Jafarzadeh, P.; Oudah, M.; Assoud, A.; Farahi, N.; Müller, E.; Kleinke, H. High Thermoelectric Performance of $Ba_3Cu_{16-x}(S,Te)_{11}$. *J. Mater. Chem. C* **2018**, *6*, 13043–13048.
(81) Oudah, M.; Kleinke, K. M.; Kleinke, H. Thermoelectric Properties of the Quaternary Chalcogenides $BaCu_{5.9}STe_6$ and $BaCu_{5.9}SeTe_6$. *Inorg. Chem.* **2015**, *54*, 845–849.
(82) Jafarzadeh, P.; Rodrigues, M. R.; Shi, Y.; Assoud, A.; Zou, T.; Kycia, J. B.; Kleinke, H. Effect of Mixed Occupancies on the Thermoelectric Properties of $BaCu_{6-x}Se_{1-y}Te_{6+y}$ Polychalcogenides. *Dalt. Trans.* **2019**, *48*, 9357–9364.
(83) Kuropatwa, B.; Cui, Y.; Assoud, A.; Kleinke, H. Crystal Structure and Physical Properties of the New Selenide-Tellurides Ba_3Cu_{17-x} $(Se,Te)_{11}$. *Chem. Mater.* **2009**, *21*, 88–93.
(84) Knauth, P.; Tuller, H. L. Solid-State Ionics: Roots, Status, and Future Prospects. *J. Am. Ceram. Soc.* **2004**, *85*, 1654–1680.
(85) Qiu, P.; Agne, M. T.; Liu, Y.; Zhu, Y.; Chen, H.; Mao, T.; Yang, J.; Zhang, W.; Haile, S. M.; Zeier, W. G.; Janek, J.; Uher, C.; Shi, X.; Chen, L.; Snyder, G. J. Suppression of Atom Motion and Metal Deposition in Mixed Ionic Electronic Conductors. *Nat. Commun.* **2018**, *9*, 2910/1-8.
(86) Boyce, J. B.; Huberman, B. A. Superionic Conductors: Transitions, Structures, Dynamics. *Phys. Rep.* **1979**, *51*, 189–265.
(87) Heep, B. K.; Weldert, K. S.; Krysiak, Y.; Day, T. W.; Zeier, W. G.; Kolb, U.; Snyder, G. J.; Tremel, W. High Electron Mobility and Disorder Induced by Silver Ion Migration Lead to Good Thermoelectric Performance in the Argyrodite Ag_8SiSe_6. *Chem. Mater.* **2017**, *29*, 4833–4839.
(88) Reissig, F.; Heep, B.; Panthöfer, M.; Wood, M.; Anand, S.; Snyder, G. J.; Tremel, W. Effect of Anion Substitution on the Structural and Transport Properties of Argyrodites $Cu_7PSe_{6-x}S_X$. *Dalt. Trans.* **2019**, *48*, 15822–15829.
(89) Vaqueiro, P.; Guélou, G.; Kaltzoglou, A.; Smith, R. I.; Barbier, T.; Guilmeau, E.; Powell, A. V. The Influence of Mobile Copper Ions on the Glass-Like Thermal Conductivity of

Copper-Rich Tetrahedrites. *Chem. Mater.* **2017**, *29*, 4080–4090.
(90) Shi, X.; Chen, L.; Uher, C. Recent Advances in High-Performance Bulk Thermoelectric Materials. *Int. Mater. Rev.* **2016**, *61*, 379–415.
(91) Brown, D. R.; Day, T.; Caillat, T.; Snyder, G. J. Chemical Stability of $(Ag,Cu)_2Se$: A Historical Overview. *J. Electron. Mater.* **2013**, *42*, 2014–2019.
(92) Zhao, L.; Wang, X.; Fei, F. Y.; Wang, J.; Cheng, Z.; Dou, S.; Wang, J.; Snyder, G. J. High Thermoelectric and Mechanical Performance in Highly Dense $Cu_{2-x}S$ Bulks Prepared by a Melt-Solidification Technique. *J. Mater. Chem. A* **2015**, *3*, 9432–9437.
(93) Yang, D.; Benton, A.; He, J.; Tang, X. Novel Synthesis Recipes Boosting Thermoelectric Study of A_2Q (A = Cu, Ag; Q = S, Se, Te). *J. Phys. D. Appl. Phys.* **2020**, *53*, 19300/1-13.
(94) He, Y.; Day, T.; Zhang, T.; Liu, H.; Shi, X.; Chen, L.; Snyder, G. J. High Thermoelectric Performance in Non-Toxic Earth-Abundant Copper Sulfide. *Adv. Mater.* **2014**, *26*, 3974–3978.
(95) Liu, W.; Yang, L.; Chen, Z.; Zou, J. Promising and Eco-Friendly Cu_2X-Based Thermoelectric Materials: Progress and Applications. *Adv. Mater.* **2020**, *32*, 1905703/1-28.
(96) Piskach, L. V; Parasyuk, O. V; Olekseyuk, I. D.; Romanyuk, Y. E.; Volkov, S. V; Pekhnyo, V. I. Interaction of Argyrodite Family Compounds with the Chalcogenides of II-b Elements. *J. Alloys Compd.* **2006**, *421*, 98–104.
(97) Yu, C.; Zhao, F.; Luo, J.; Zhang, L.; Sun, X. Recent Development of Lithium Argyrodite Solid-State Electrolytes for Solid-State Batteries: Synthesis, Structure, Stability and Dynamics. *Nano Energy* **2021**, *83*, 105858/1-25.
(98) Hu, W.-Q.; Shi, Y.-F.; Wu, L.-M. Synthesis and Shape Control of Ag_8SnS_6 Submicropyramids with High Surface Energy. *Cryst. Growth Des.* **2012**, *12*, 3458–3464.
(99) Li, L.; Liu, Y.; Dai, J.; Hong, A.; Zeng, M.; Yan, Z.; Xu, J.; Zhang, D.; Shan, D.; Liu, S.; Ren, Z.; Liu, J.-M. High Thermoelectric Performance of Superionic Argyrodite Compound Ag_8SnSe_6. *J. Mater. Chem. C* **2016**, *4*, 5806–5813.
(100) Shen, X.; Xia, Y.; Yang, C.; Zhang, Z.; Li, S.; Tung, Y.; Benton, A.; Zhang, X.; Lu, X.; Wang, G.; He, J.; Zhou, X. High Thermoelectric Performance in Sulfide-Type Argyrodites Compound $Ag_8Sn(S_{1-x}Se_x)_6$ Enabled by Ultralow Lattice Thermal Conductivity and Extended Cubic Phase Regime. *Adv. Funct. Mater.* **2020**, *30*, 2000526/1-10.
(101) Venkatraman, M.; Blachnik, R.; Schlieper, A. The Phase Diagrams of M_2X-SiX_2 (M Is Cu, Ag; X Is S, Se). *Thermochim. Acta* **1995**, *249*, 13–20.
(102) von Unterrichter, J.; Range, K.-J. Ag_8GeTe_6, a Representative of the Argyrodite Family. *Z. Naturforsch.* **1978**, *33b*, 866–872.
(103) Boucher, F.; Evain, M.; Brec, R. Distribution and Ionic Diffusion Path of Silver in Gamma-Ag_8GeTe_6: A Temperature Dependent Anharmonic Single Crystal Structure Study. *J. Solid State Chem.* **1993**, *107*, 332–346.
(104) Chbani, N.; Cai, X.; Loireau-Lozac'h, A. M.; Guittard, M. Ternary Silver - Germanium -

Sulfur. Quasibinary Disulfide Germanium -Sulfide Silver Electric Conductivity of the Silver Richer Glass. *Mat. Res. Bull* **1992**, *27*, 1355–1992.
(105) Gorochov, O. Les Composes Ag_8MX_6 (M = Si, Ge, Sn et X = S, Se, Te). *Bull. Soc. Chim. Fr.* **1968**, *6*, 2263–2275.
(106) Boucher, F.; Evain, M.; Brec, R. Single-Crystal Structure Determination of Gamma-Ag_8SiTe_6 and Powder X-Ray Study of Low-Temperature Alpha and Beta Phases. *J. Solid State Chem.* **1992**, *100*, 341–355.
(107) Jin, M.; Lin, S.; Li, W.; Chen, Z.; Li, R.; Wang, X.; Chen, Y.; Pei, Y. Fabrication and Thermoelectric Properties of Single-Crystal Argyrodite Ag_8SnSe_6. *Chem. Mater.* **2019**, *31*, 2063–2610.
(108) Matje, P.; Schön, G. Ag_8SnTe_6 - A New Argyrodite. *Z. Naturf.* **1980**, *2*, 247.
(109) Gather, B.; Blachnik, R. "Ag_8SnTe_6" A New Stable Argyrodite? *Z. Naturf.* **1983**, *6*, 786–787.
(110) Li, W.; Lin, S.; Ge, B.; Yang, J.; Zhang, W.; Pei, Y. Low Sound Velocity Contributing to the High Thermoelectric Performance of Ag_8SnSe_6. *Adv. Sci.* **2016**, *3*, 1600196/1-7.
(111) Zhang, X.; Zhang, C.-L.; Lin, S.; Lu, H.; Pei, Y.; Jia, S. Thermoelectric Properties of N-Type Nb-Doped Ag_8SnSe_6. *J. Appl. Phys.* **2016**, *119*, 135101/1-6.
(112) Yang, C.; Luo, Y.; Li, X.; Cui, J. N-Type Thermoelectric Ag_8SnSe_6 with Extremely Low Lattice Thermal Conductivity by Replacing Ag with Cu. *RSC Adv.* **2021**, *11*, 3732–3739.
(113) Ghrib, T.; Al-Otaibi, A. L.; Almessiere, M. A.; Assaker, I. B.; Chtourou, R. High Thermoelectric Figure of Merit of Ag_8SnS_6 Component Prepared by Electrodeposition Technique. *Chin. Phys. Lett.* **2015**, *32*, 127402/1-5.
(114) Fan, J.; Carrillo-Cabrera, W.; Antonyshyn, I.; Prots, Y.; Veremchuk, I.; Schnelle, W.; Drathen, C.; Chen, L.; Grin, Y. Crystal Structure and Physical Properties of Ternary Phases around the Composition $Cu_5Sn_2Se_7$ with Tetrahedral Coordination of Atoms. *Chem. Mater.* **2014**, *26*, 5244–5251.
(115) Azam, S.; Khan, S. A.; Goumri-Said, S. DFT Combined to Boltzmann Transport Theory for Optoelectronic and Thermoelectric Properties Investigations for Monoclinic Metallic Selenide: $Cu_5Sn_2Se_7$. *Optik (Stuttg).* **2016**, *127*, 5472–5478.
(116) Adhikary, A.; Mohapatra, S.; Lee, S. H.; Hor, Y. S.; Adhikari, P.; Ching, W. Y.; Choudhury, A. Metallic Ternary Telluride with Sphalerite Superstructure. *Inorg. Chem.* **2016**, *55*, 2114–2122.
(117) Assoud, A.; Thomas, S.; Sutherland, B.; Zhang, H.; Tritt, T. M.; Kleinke, H. Thermoelectric Properties of the New Polytelluride $Ba_3Cu_{14-\delta}Te_{12}$. *Chem. Mater.* **2006**, *18*, 3866–3872.
(118) *User's Manual Sartorius YDK01, YDK01-0D, YDK01B, YDK01LP, YDK01MS, YDK02MS Density Determination Kit*; Göttingen, Germany, 2011.
(119) Bragg, W. H.; Bragg, W. L. The Reflection of X-Rays by Crystals . *Proc. R. Soc. A* **1913**, *88*, 428–438.
(120) Stout, G. H.; Jensen, L. H. *X-Ray Structure Determination: A Practical Guide*; John

Wiley & Sons, Inc.: New York, 1989.
(121) *M86-Exx078 APEX2 User Manual*; Bruker AXS Inc.: Madison, WI, 2006.
(122) Sheldrick, G. M. A Short History of SHELX. *Acta Crystallogr. A* **2008**, *64*, 112–122.
(123) Rietveld, H. M. A Profile Refinement Method for Nuclear and Magnetic Structures. *J. Appl. Crystallogr.* **1969**, *2*, 65–71.
(124) Young, R. A. *The Rietveld Method*; Oxford University Press: New York, 2002.
(125) Larson, A. C.; von Dreele, R. B. *GSAS - General Structure Analysis System*; Los Alamos National Laboratory: Los Alamos, NM, 2000.
(126) Toby, B. H. EXPGUI , a Graphical User Interface for GSAS. *J. Appl. Crystallogr.* **2001**, *34*, 210–213.
(127) Toby, B. H. R Factors in Rietveld Analysis: How Good Is Good Enough? *Powder Diffr.* **2006**, *21*, 67–70.
(128) Egerton, R. F. *Physical Principles of Electron Microscopy*; Springer US: Boston, MA, 2005.
(129) Schwarz, K. DFT Calculations of Solids with LAPW and WIEN2K. *J. Solid State Chem.* **2003**, *176*, 319–328.
(130) Perdew, J. P.; Burke, K.; Ernzerhof, M. Generalized Gradient Approximation Made Simple. *Phys. Rev. Lett.* **1996**, *77*, 3865–3868.
(131) Baseden, K. A.; Tye, J. W. Introduction to Density Functional Theory: Calculations by Hand on the Helium Atom. *J. Chem. Educ.* **2014**, *91*, 2116–2123.
(132) Macia-Barber, E. *Thermoelectric Materials Advances and Applications*; CRC Press, Taylor & Francis Group: Boca Raton, FL, USA, 2015; Vol. 6.
(133) Blaha, P.; Schwarz, K.; Tran, F.; Laskowski, R.; Madsen, G. K. H.; Marks, L. D. WIEN2k: An APW+lo Program for Calculating the Properties of Solids. *J. Chem. Phys.* **2020**, *152*, 074101/1-30.
(134) Madsen, G. K. H.; Singh, David, J. BoltzTraP. A Code for Calculating Band-Structure Dependent Quantities. *Comput. Phys. Commun.* **2006**, *175*, 67–71.
(135) De Boor, J.; Müller, E. Data Analysis for Seebeck Coefficient Measurements . *Rev. Sci. Instrum.* **2013**, *84*, 065102/1-9.
(136) Parker, W. J.; Jenkins, R. J.; Butler, C. P.; Abbott, G. L. Flash Method of Determining Thermal Diffusivity, Heat Capacity, and Thermal Conductivity. *J. Appl. Phys.* **1961**, *32*, 1684.
(137) Chu, F. I.; Taylor, R. E.; Donaldson, A. B. Thermal Diffusivity Measurements at High Temperatures by the Radial Flash Method . *J. Appl. Phys.* **1980**, *51*, 341.
(138) Physical Property Measurement System - Heat Capacity Option User's Manual. Quantum Design: San Diego 2004.
(139) Hall, E. H. *On The Rotational Coefficient of Various Metals*; 1881.
(140) Schäfer, W.; Scheunemann, K.; Nitsche, R. Crystal Structure and Magnetic Properties of $Cu_4NiSi_2S_7$. *Mater. Res. Bull.* **1980**, *15*, 933–937.
(141) Fan, J.; Carrillo-Cabrera, W.; Antonyshyn, I.; Prots, Y.; Veremchuk, I.; Schnelle, W.;

Drathen, C.; Chen, L.; Grin, Y. Crystal Structure and Physical Properties of Ternary Phases around the Composition $Cu_5Sn_2Se_7$ with Tetrahedral Coordination of Atoms. *Chem. Mater.* **2014**, *26*, 5244–5251.

(142) Cheng, X.; Li, Z.; You, Y.; Zhu, T.; Yan, Y.; Su, X.; Tang, X. Role of Cation Vacancies in Cu_2SnSe_3 Thermoelectrics. *ACS Appl. Mater. Interfaces* **2019**, *11*, 24212–24220.

(143) Dong, Y.; Khabibullin, A. R.; Wei, K.; Ge, Z.-H.; Martin, J.; Salvador, J. R.; Woods, L. M.; Nolas, G. S. Synthesis, Transport Properties, and Electronic Structure of $Cu_2CdSnTe_4$. *Appl. Phys. Lett.* **2014**, *104*, 252107/1-4.

(144) Pei, Y.; Wang, H.; Snyder, G. J. Band Engineering of Thermoelectric Materials. *Adv. Mater.* **2012**, *24*, 6125–6135.

(145) Shi, Y.; Mashmoushi, N.; Wegner, W.; Jafarzadeh, P.; Sepahi, Z.; Assoud, A.; Kleinke, H. Ultralow Thermal Conductivity of $Tl_4Ag_{18}Te_{11}$. *J. Mater. Chem. C* **2019**, *7*, 8029–8036.

(146) Heo, J.; Laurita, G.; Muir, S.; Subramanian, M. A.; Keszler, D. A. Enhanced Thermoelectric Performance of Synthetic Tetrahedrites. *Chem. Mater.* **2014**, *26*, 2047–2051.

(147) Jafarzadeh, P.; Menezes, L.; Cui, M.; Assoud, A.; Zhang, W.; Halasyamani, P.; Kleinke, K. $BaCuSiTe_3$: A Noncentrosymmetric Semiconductor with $CuTe_4$ Tetrahedra and Ethane-like Si_2Te_6 Units. *Inorg. Chem.* **2019**, *58*, 11656–11663.

(148) Perdew, J. P.; Burke, K.; Ernzerhof, M. Generalized Gradient Approximation Made Simple. *Phys. Rev. Lett.* **1996**, *77*, 3865–3868.

(149) Koller, D.; Tran, F.; Blaha, P. Merits and Limits of the Modified Becke-Johnson Exchange Potential. *Phys. Rev. B* **2011**, *83*, 195134-1–10.

(150) Skriver, H. L. *The LMTO Method*; Springer: Berlin, Germany, 1984.

(151) Lu, X.; Morelli, D. T.; Xia, Y.; Ozolins, V. Increasing the Thermoelectric Figure of Merit of Tetrahedrites by Co-Doping with Nickel and Zinc. *Chem. Mater.* **2015**, *27*, 408–413.

(152) Jafarzadeh, P.; Rodrigues, M. R.; Shi, Y.; Assoud, A.; Zou, T.; Kycia, J. B.; Kleinke, H. Effect of Mixed Occupancies on the Thermoelectric Properties of $BaCu_{6-x}Se_{1-y}Te_{6+y}$ Polychalcogenides. *Dalt. Trans.* **2019**, *48*, 9357–9364.

(153) Blaha, P.; Schwarz, K.; Madsen, G. K. H.; Kvasnicka, D.; Luitz, J.; Schwarz, K. WIEN2k, An Augmented Plane Wave + Local Orbitals Program for Calculating Crystal Properties. Wien, Austria 2001.

(154) Boon-On, P.; Aragaw, B. A.; Lee, C. Y.; Shi, J. Bin; Lee, M. W. Ag_8SnS_6: A New IR Solar Absorber Material with a near Optimal Bandgap. *RSC Adv.* **2018**, *8*, 39470–39476.

(155) Perdew, J. P. Density Functional Theory and the Band Gap Problem. *Int. J. Quantum Chem.* **1986**, *19*, 497–523.

(156) Qi, X.; Chen, J.; Guo, K.; He, S.; Yang, J.; Li, Z.; Xing, J.; Hu, J.; Luo, H.; Zhang, W.; Luo, J. Thermal Stability of Ag_9GaSe_6 and Its Potential as a Functionally Graded Thermoelectric Material. *Chem. Eng. J.* **2019**, *374*, 494–501.

Appendix

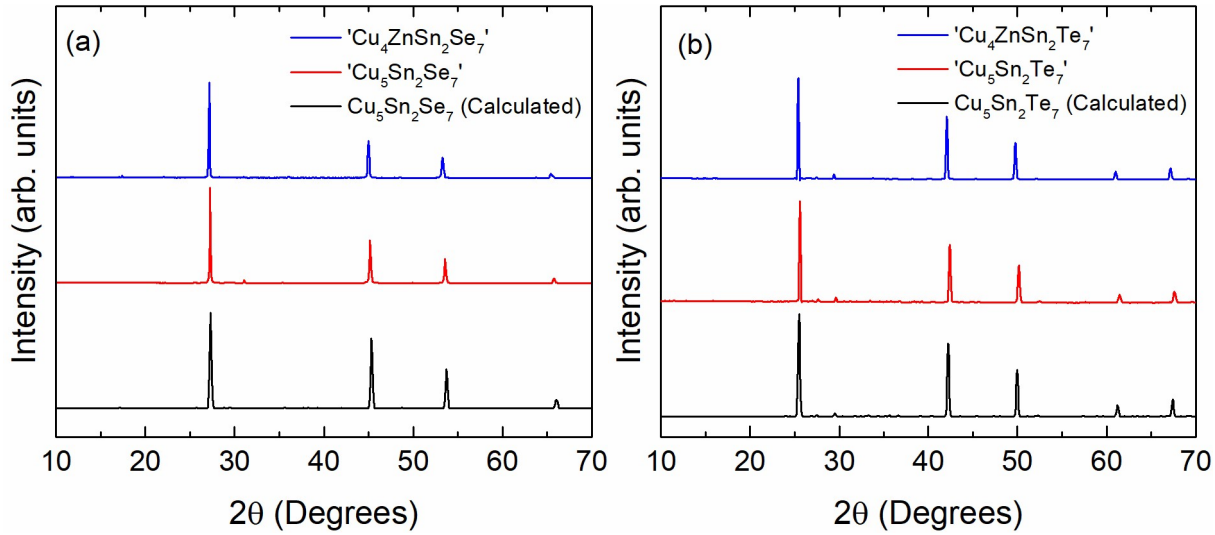

Figure A-1. Powder X-ray diffraction patterns of (a) $Cu_5Sn_2Se_7$, $Cu_4ZnSn_2Se_7$ and (b) $Cu_5Sn_2Te_7$, $Cu_4ZnSn_2Te_7$.

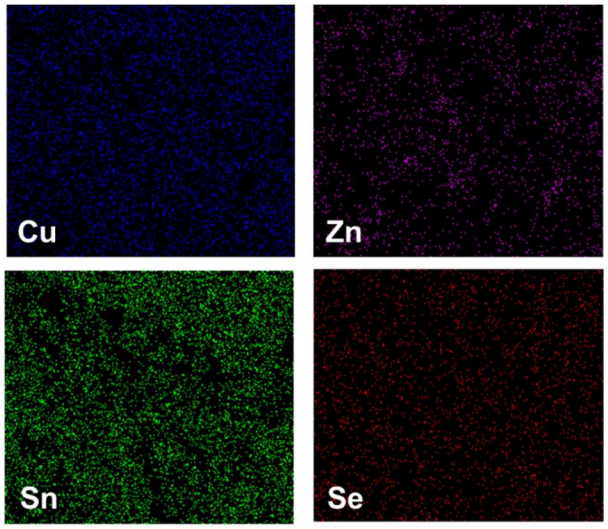

Figure A-2. EDAX mappings of '$Cu_4ZnSn_2Se_7$' which displays homogenous distribution of elements.

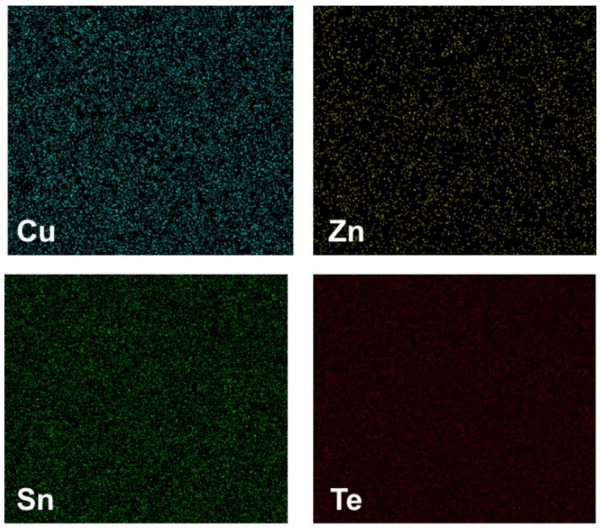

Figure A-3. EDAX mappings of '$Cu_4ZnSn_2Te_7$' which displays homogenous distribution of elements.

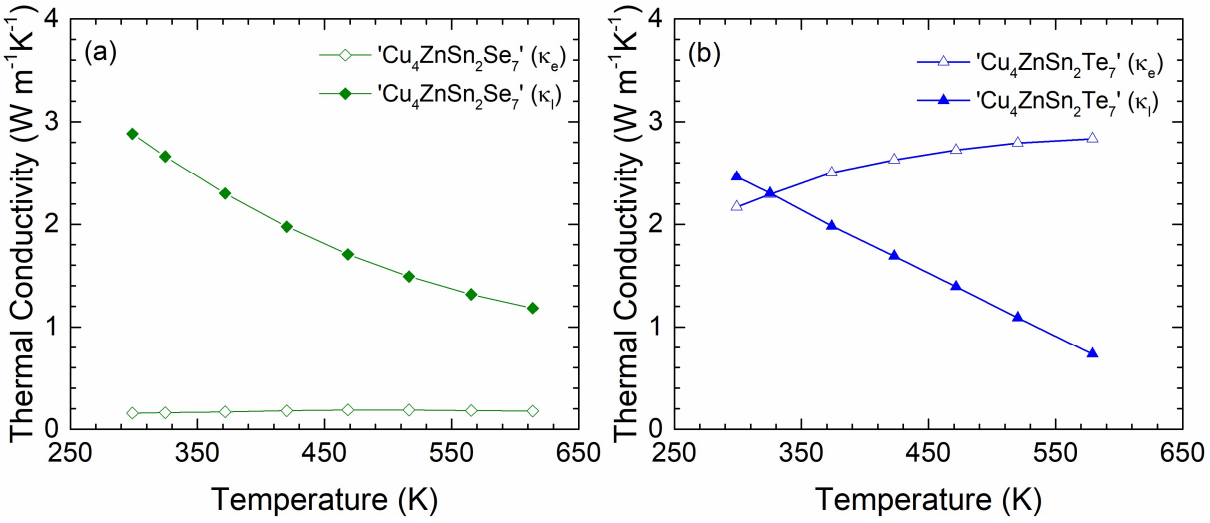

Figure A-4. Temperature dependence of the electrical and lattice components of the thermal conductivity of (a) '$Cu_4ZnSn_2Se_7$' and (b) '$Cu_4ZnSn_2Te_7$'.

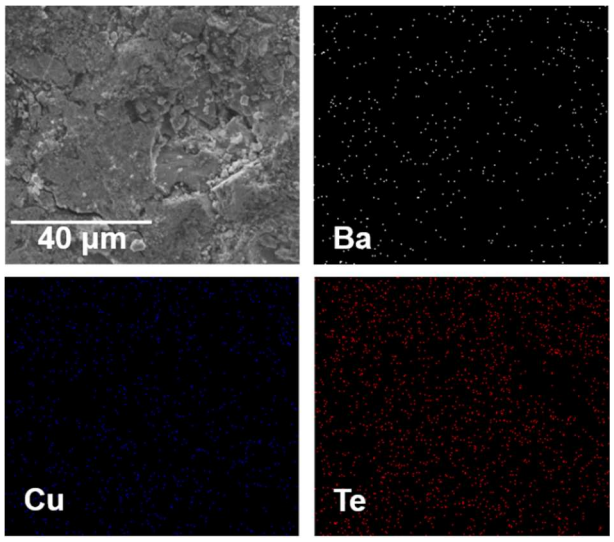

Figure A-5. EDAX maps of $Ba_3Cu_{13.975}Te_{12}$.

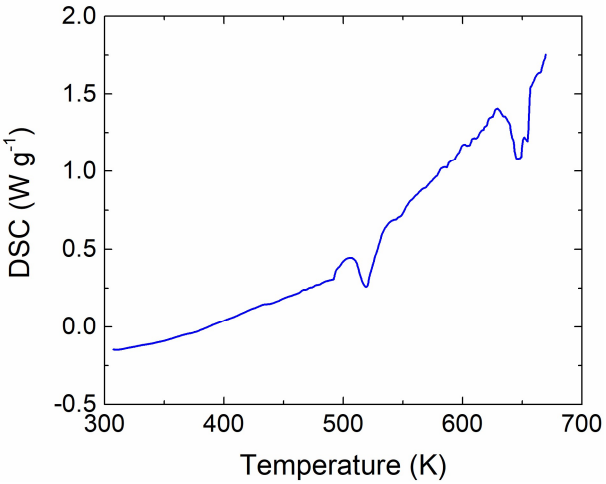

Figure A-6. DSC of $Ba_3Cu_{13.175}Te_{12}$'.

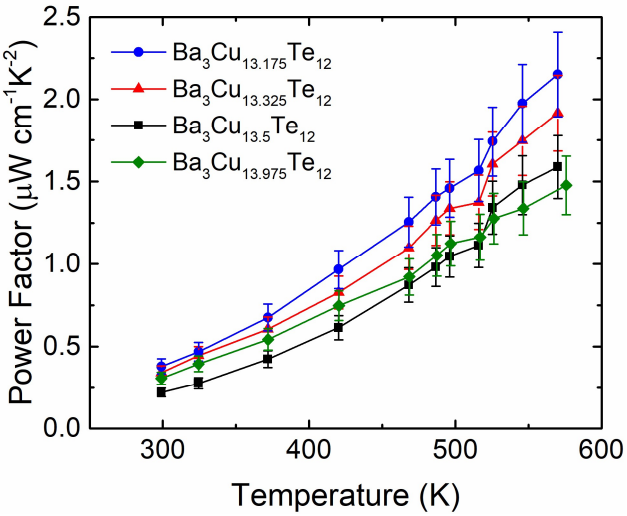

Figure A-7. Temperature dependence of the power factor of $Ba_3Cu_{14-\delta}Te_{12}$ (where $\delta = 0.025$, 0.500, 0.576, and 0.825) with 8% error bars.

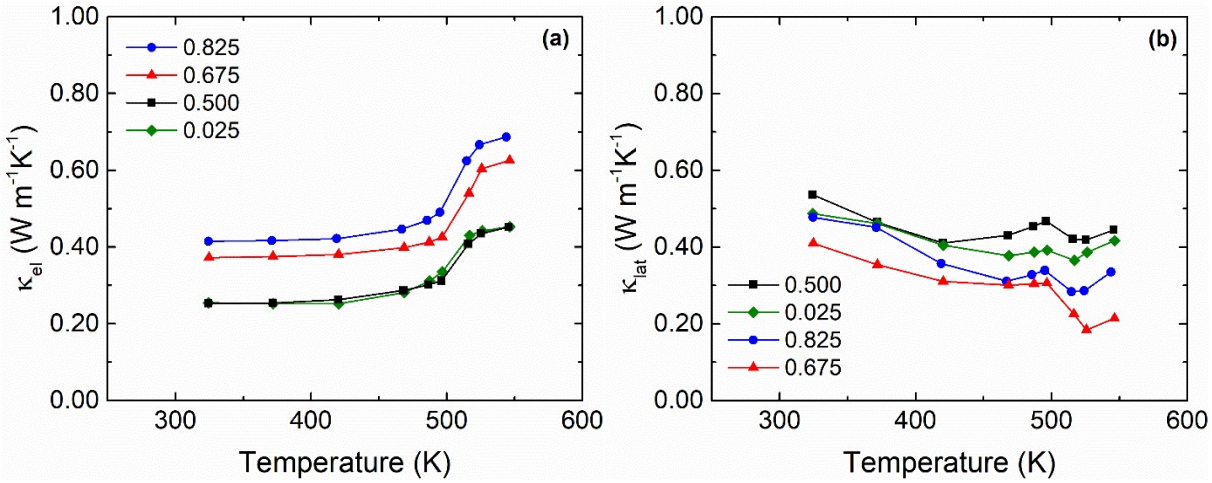

Figure A-8. Temperature dependence of (a) electrical component of the thermal conductivity and (b) lattice component of the thermal conductivity of $Ba_3Cu_{14-\delta}Te_{12}$ (where $\delta = 0.025$, 0.500, 0.576, and 0.825).

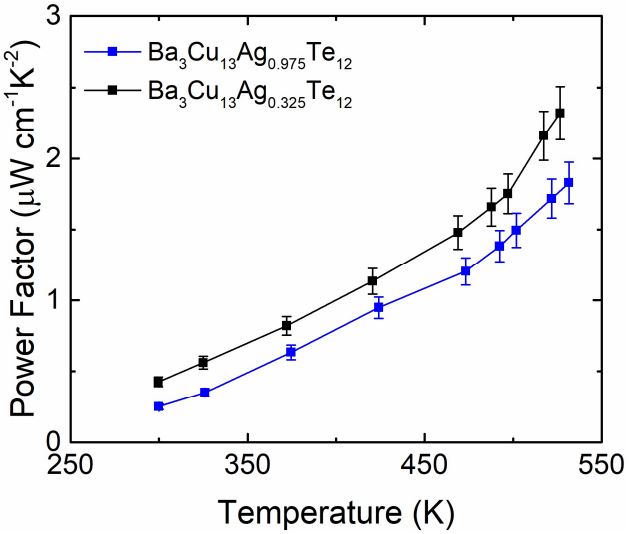

Figure A-9. Temperature dependence of the power factor of $Ba_3Cu_{13}Ag_{0.975}Te_{12}$ and $Ba_3Cu_{13}Ag_{0.325}Te_{12}$ with 8% error bars.

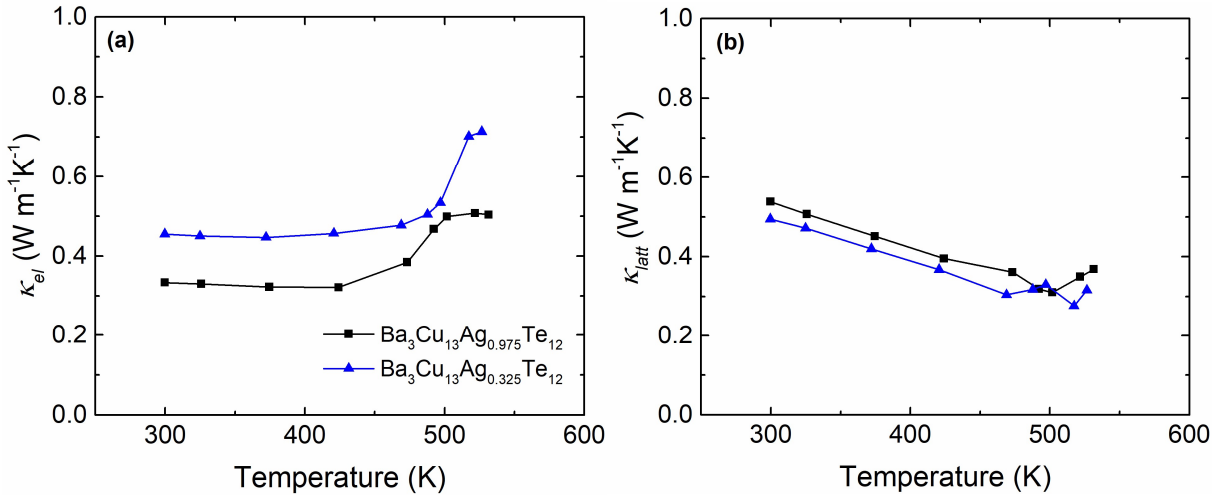

Figure A-10. Temperature dependence of (a) electrical component of the thermal conductivity and (b) lattice component of the thermal conductivity of $Ba_3Cu_{13}Ag_{0.975}Te_{12}$ and $Ba_3Cu_{13}Ag_{0.325}Te_{12}$.

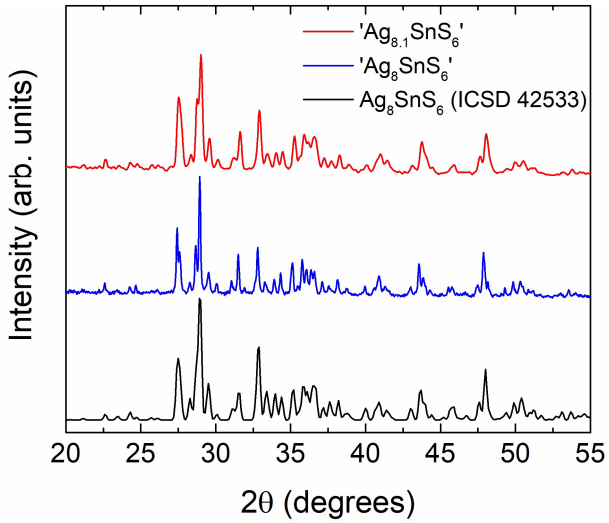

Figure A-11. X-ray powder diffraction data of Ag_8SnS_6 and 'Ag_8SnS_6'

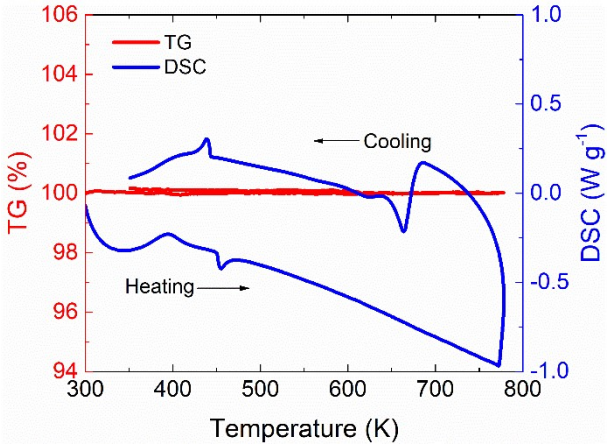

Figure A-12. Combined DSC/TG curves of Ag_8SnS_6. The peak during cooling below 700 K is an artefact of the machine setup.

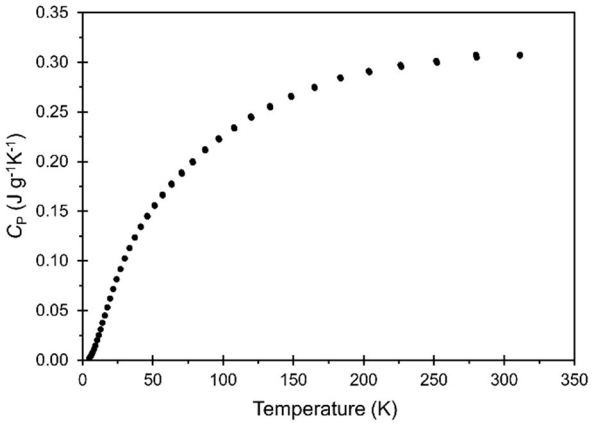

Figure A-13. Specific heat of Ag_8SnS_6.

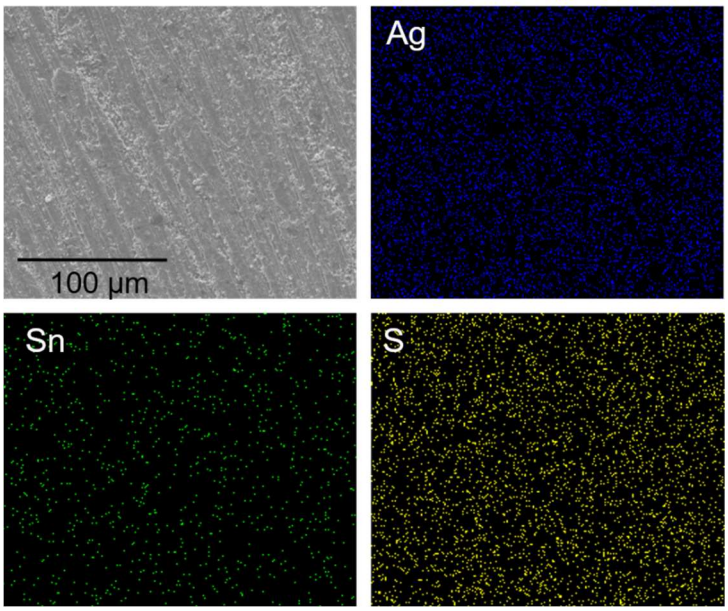

Figure A-14. EDAX mappings of 'Ag_8SnS_6' which displays homogenous distribution of elements.

Table A-1. Refined lattice parameters of of $Cu_{5-x}Zn_xSn_2Q_7$.

	'$Cu_5Sn_2Se_7$'	'$Cu_4ZnSn_2Se_7$'	'$Cu_5Sn_2Te_7$'	'$Cu_4ZnSn_2Te_7$'
a (Å)	12.5580(8)	12.6067(5)	13.544(1)	13.5925(2)
b (Å)	5.6570(2)	5.6771(1)	6.0442(2)	6.0696(2)
c (Å)	8.9991(5)	8.9270(6)	9.5771(3)	9.4935(2)
β (º)	98.170(5)	98.135(3)	98.063(3)	98.302(2)
V (Å^3)	632.81(7)	632.47(5)	776.26(5)	775.02(3)

Table. A-2. Results of EDAX confirming homogeneity of '$Cu_4ZnSn_2Se_7$'

Element	Atomic Percent		
	Theoretical	Average	STDEV
Cu (K)	28.57	29.36	1.18
Zn (K)	7.14	6.81	1.05
Sn (L)	14.29	14.68	0.32
Se (L)	50.00	49.14	1.94

Table. A-3. Results of EDAX confirming homogeneity of '$Cu_4ZnSn_2Te_7$'

Element	Atomic Percent		
	Theoretical	Average	STDEV
Cu (K)	28.57	28.04	1.77
Zn (K)	7.14	7.28	0.77
Sn (L)	14.29	14.67	1.05
Te (L)	50.00	50.01	1.34

Table A-4. Results of EDX confirming homogeneity of $Ba_3Cu_{14-\delta}Te_{12}$

Material	Element	Atomic Percent		
		Theoretical	Average	STDEV
$Ba_3Cu_{13.975}Te_{12}$	Ba (L)	10.4	11.1	0.64
	Cu (K)	48.2	45.9	0.40
	Te (L)	41.4	43	0.99
$Ba_3Cu_{13.50}Te_{12}$	Ba (L)	10.5	11.4	0.49
	Cu (K)	47.4	45.2	0.93
	Te (L)	42.1	43.5	0.78
$Ba_3Cu_{13.325}Te_{12}$	Ba (L)	10.6	10.4	0.30
	Cu (K)	47.0	47.0	0.69
	Te (L)	42.4	42.7	0.84
$Ba_3Cu_{13.175}Te_{12}$	Ba (L)	10.7	10.9	0.58
	Cu (K)	46.8	46.0	0.49
	Te (L)	45.6	43.2	0.45

Table A-5. Results of EDAX confirming homogeneity of $Ba_3Cu_{14-\delta-x}Ag_xTe_{12}$

Material	Element	Atomic Percent		
		Theoretical	Average	STDEV
$Ba_3Cu_{13}Ag_{0.975}Te_{12}$	Ba (L)	10.4	11.1	0.20
	Cu (K)	44.9	44	1.54
	Ag (L)	3.4	2.4	0.71
	Te (L)	41.4	43.1	0.74
$Ba_3Cu_{13}Ag_{0.50}Te12$	Ba (L)	10.5	10.7	0.20
	Cu (K)	45.6	46	0.95
	Ag (L)	1.8	1.2	0.33
	Te (L)	42.1	42.6	0.46

Table A-6. Results of EDAX confirming homogeneity of 'Ag_8SnS_6'

Element	Atomic Percent		
	Theoretical	Average	STDEV
Ag (L)	53.33	52.17	0.99
Sn (L)	6.67	6.59	0.83
S (K)	40	41.1	0.62

Table A-7. Results of EDAX confirming homogeneity of '$Ag_{8.1}SnS_6$'

Element	Atomic Percent		
	Theoretical	Average	STDEV
Ag (L)	53.64	54.30	0.47
Sn (L)	6.62	6.15	0.25
S (K)	39.74	39.56	0.22